R-01-22

System and safety studies of accelerator driven transmutation systems

Annual Report 2000

Waclaw Gudowski, Jan Wallenius, Kamil Tucek, Marcus Eriksson, Johan Carlsson, Per Seltborg and J Cetnar

Department of Nuclear and Reactor Physics
Royal Institute of Technology, Stockholm

May 2001

SKB

System and safety studies of accelerator driven transmutation systems

Annual Report 2000

Waclaw Gudowski, Jan Wallenius, Kamil Tucek,
Marcus Eriksson, Johan Carlsson, Per Seltborg
and J Cetnar

Department of Nuclear and Reactor Physics
Royal Institute of Technology, Stockholm

May 2001

PREFACE

The research on safety of Accelerator-Driven Transmutation Systems (ADS) at the Department of Nuclear and Reactor Physics has been focused on:

a) ADS core design and development of advanced nuclear fuel optimised for high transmutation rates and good safety features;

b) analysis of ADS-dynamics

c) computer code and nuclear data development relevant for simulation and optimization of ADS;

d) participation in ADS experiments including 1 MW spallation target manufacturing, subcrtical experiments MUSE (CEA-Cadarache)

Moreover, during the reporting period the EU-project "IABAT", co-ordinated by the Department of Nuclear and Reactor Physics has been finished and 4 other projects have been initiated in the frame of the 5th European Framework Programme.

Most of the research topics reported in this paper are referred to appendices, which have been published in the open literature. The topics, which are not yet published, are described here in more details.

Blue text color in a PDF version of this report implies links which can take a reader by a mouse click to the referred part of the report or to a referred Appendix.

iv

TABLE OF CONTENTS

APPENDICES:

Articles/Reports

I.   Kamil Tucek, Burnable Poisons in Sub-Critical Cores Dedicated to Radiotoxic Waste Transmutation", Lic. thesis, TRITA – FYS 3069, Royal Institute of Technology, Stockholm, 2000.

II.   J. Wallenius, K. Tucek and W. Gudowski, Safety analysis of nitride fuels in cores dedicated to waste transmutation. Actinide and Fission Product Partitioning and Transmutation, Proceedings of the 6th International Information Exchange Meeting, Madrid 2000. OECD/NEA, 2000.

III.   W. Gudowski, editor, Impact of Accelerator Based Technologies on Nuclear Fission Safety IABAT-project, EUR 19608, 2000

IV.   Johan Carlsson, Decay Heat Removal from the Guard Vessel by Thermal Radiation and Natural Convection, Lic. thesis, Royal Institute of Technology, Stockholm, December 2000.

V.   A. V. Ignatyuk, V. P. Lunev, Yu. N. Shubin, E.V. Gai, N. N. Titarenko A.Ventura, W.Gudowski, Neutron Cross Section Evaluations for ^{238}U up to 150 MeV, Nuclear Science and Technology, November 2000.

VI.   W. Gudowski, Transmutation of Nuclear Waste, Nuclear Physics A663&664, 169c-182c, 2000.

VII.   W. Gudowski, Transmutation of Isotopes – Ecological and Energy Production Aspects, Acta Physica Polonica B No 1, Vol. 31, 2000.

VIII.   W. Gudowski, Why Accelerator-Driven Transmutation of Wastes Enables Future Nuclear Power?. Proc. of Linac2000, XX International Linac Conference, Monterey, August 21-25, 2000. Invited paper.

IX.   K. Tucek, J. Wallenius and W. Gudowski, Optimal distribution of fuel, poisons and diluents in sub-critical cores dedicated to waste transmutation. In Proc. Int. Conf. on Emerging Nuclear Energy Systems, ICENES 00, Petten 2000.

X.   D. Filges, W. Gudowski, Summary and highlights of hadronic sessions, speculations and perspective views, International Conference on Advanced Monte Carlo for Radiation Physics, Particle Transport Simulation and Applications, 23-26 October, 2000, Lisbon, Portugal. Invited contribution.

XI.   M. Eriksson, J. Wallenius, K. Tucek, W. Gudowski, "Preliminary Safety Analysis of a Swedish Accelerator Driven System Employing Nitride Fuel and Burnable Absorbers", IAEA Technical Committee Meeting on "Core Physics and Engineering Aspects of Emerging Nuclear Energy Systems for Energy

Generation and Transmutation", 28 November to 1 December 2000, Argonne National Laboratory.

1   INTRODUCTION

The research program in accelerator-driven nuclear transmutation at the Department of Nuclear and Reactor Physics of the Royal Institute of Technology in Stockholm is focused on safety aspects of transmutation systems. In order to cover this broad and complicated topic and to harmonize our activities with international projects in which we actively participate, our research has been structured into few major workpackages:

- Design of high-performance ADS-core and analysis of its parameters including dynamics of ADS, emergency cooling systems, radiation stability of materials and development of advanced fuel for ADS
- Development of simulation tools and nuclear data libraries necessary for advanced ADS-simulations
- Participation in ADS-related experiments, with a special attention to important components of ADS (e.g. construction of the spallation target)

2   SING-SING CORE (SSC) CONCEPT

2.1   CHARACTERISTCS OF SSC

Neutronic and thermal hydraulic studies of a modular sub-critical TRU burner have been performed addressing issues associated with high reactivity loss during burnup and extensive helium production in MA fuel pins. This design, named audaciously Sing-Sing Core (SSC), is based on introduction of burnable absorbers into the reactor core of an accelerator-driven system incinerating TRU nuclides.

After feasibility studies of different options for burnable absorber, boron carbide was chosen as a reference material due to its good thermal and irradiation stability in fast neutron spectrum. Furthermore, the burnability of boron is superior in comparison to other candidates for burnable absorbers like Hf or Eu. The role of boron carbide (enriched in ^{10}B up to 90% in order to avoid neutron moderation in interactions with ^{11}B) in the system is multifold:

- it mitigates reactivity loss due to the burnout of fissile plutonium nuclides,
- effectively suppresses neutron captures of slow-downed neutrons in minor actinides, limiting thus production of helium source term in fuel pins (^{242}Cm, ^{238}Pu),
- dilutes highly reactive fuel enabling to achieve flat power distribution similar to that attainable in critical systems.

With respect to the choice of fuel, nitrides have been considered as a primary candidate. They offer good combination of thermal stability together with high thermal conductivity and heavy-metal density allowing a factor of two higher linear power ratings than those typical for oxides and metallic cores. In order to mitigate adverse effects of burnable absorbers on coolant void coefficient, lead-bismuth eutectic has been adopted as a coolant material. Pb/Bi has also low chemically activity with outer environments (water) excluding possibility for fire or explosions. On the other hand, thermal physical properties of Pb/Bi are somewhat inferior to those of sodium - 30% lower mass flow, and significantly lower heat transfer coefficients - eventuating in high pitch-to-diameter ratios and temperature gradients in-between outer cladding and coolant bulk. Liquid lead-bismuth eutectic is also highly corrosive in the contact with cladding and structural materials at higher temperatures. This drawback can be to some extent (for temperatures lower than 625 ^oC and velocities less than 3.0 m/s) mitigated by the on-line control of oxygen content in the coolant. Steel specially designed for use in Russian Pb/Bi cooled reactors was chosen as a material for cladding and structural components.

The system design refers to a scenario of ADS start-up and introduction into the nuclear reactor parks (first cycle strategy), assuming therefore the composition of TRU vector being that of unrecycled PWR/BWR spent fuel (burnup 40 GWd/tHM) after 30 years of decay. A sketch of the SSC is displayed in Figure 2-1.
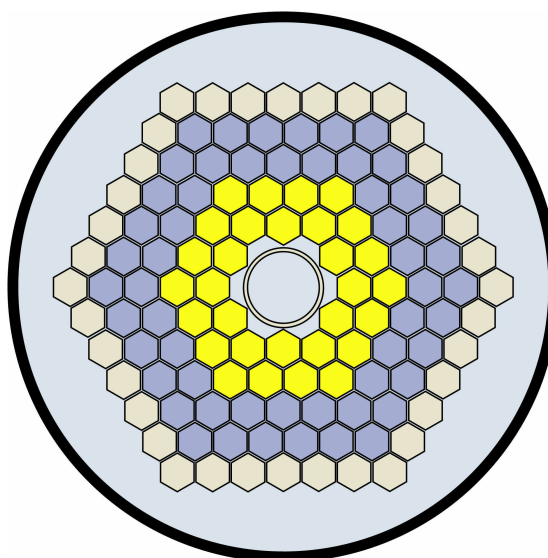
Figure 2-1. Cross-section of the Sing-Sing Core

84 hexagonal fuel assemblies with duct flat-to-flat distances of 22.0 cm have been configured in four fuel zones containing variable concentrations of TRU together with depleted uranium (yellow zones) and boron carbide (blue zones). Technetium pins are present in zone two, sub-assemblies in the outermost zone indicates steel reflector. The first two fuel zones are conceived as a multiplication buffer of spallation neutrons while outer fuel zones containing burnable absorber pins serve to transmutation purposes.

A summary of SSC principal parameters is given in Table 2-1.

The fuel pin and pellet design is similar to that of CAPRA [1] reactor assuming 15% fuel porosity allowing release of all produced helium and fission gases into the plenum. The pitch-to-diameter ratios in core zones were optimized accounting for increasing power peaking during burnup. After 300 days, the maximum linear rating of 80 kW/m is attained in zone 1 when burnup of SSC has to be interrupted due to the limitation in maximum cladding temperatures. A significant improvement of fission-to-absorption probabilities on even neutron nuclides in zones 3-4 is manifested by their 2.5-fold increase for ^{241}Am in comparison to the CAPRA and Energy Amplifier [2] figures, reducing such an equilibrium amount of He-producing nuclides (^{242}Cm) in the fuel.

On the other hand, the introduction of boron carbide into the core yields adverse effects on core safety parameters, particularly fuel temperature and coolant void coefficients. Due to the extremely hard neutron spectrum, the Doppler coefficient virtually disappears because very few neutrons reach the neutron capture resonances. With respect to the core voiding reactivity being +3500 pcm, the initial level of sub-criticality should actually be set below k_{eff}=0.965, while a value of 0.972, corresponding to the target thermal power of 20 MW, has been used for these simulations. The burnup calculations have been accomplished by the MCB (Monte Carlo Burnup – see chapter 6.1) code, irradiating the fuel for 300 days at the constant thermal power of 1200 MWt. The reactivity loss of 5600 pcm has to be compensated by an increase of accelerator power from 20 to 75 MW.

Table 2-1. Conceptual characteristics of Sing Sing Core

Reactor power [MWt]	1200
k-eigenvalue at BOL	0.972
Target outer radius [cm]	24.9
1. Sub-assembly design	
Pitch-to-diameter ratio (zone 1/zone 2-4)	1.950/1.785
Fuel pins in S/A (zone 1/2/3/4)	331/317/251/319
Absorber pins in S/A (zone 1/2/3/4)	0/0/146/78
Technetium pins in S/A (zone 1/2/3/4)	0/80/0/0
2. Neutronic characteristics	
Coolant void worth [pcm]	3500
Doppler constant [pcm]	-13
Delayed neutron fraction [pcm]	270
Effective delayed neutron fraction [pcm]	160
3. Burnup parameters	
Cycle length [days]	300
Reactivity loss [pcm/cycle]	5600
Average net TRU consumption [%h.a.]	8.7
Peak net TRU consumption [%h.a.]	11.5
Target power (BOL/EOL) [MW]	20.5/75.1
Radial power peaking in zone 1 (BOL/EOL)	1.08/1.70
Average linear power [kW/m]	48
Peak linear power [kW/m]	80

A disadvantage of introducing absorbers into accelerator driven systems is larger capture probability of spallation source neutrons, having consequently adverse effect on source efficiency. The source efficiency can be also influenced by target dimensions (diameter) or by a choice of a diluent material and fuel matrix. Thus, series of parametric studies of different system parameters have been performed in order to arrive at a distribution that maximizes both direct fission probabilities of minor actinides and source efficiencies and gains minimum power peaking.

In order to interpret the results, a multiplication of spallation neutrons exiting target can be evaluated either as:

$$M_{ext}^n = 1 + k_0 + k_0 k_1 + k_0 k_1 k_2 + \cdots$$

where k_0 is the external source neutron multiplication factor, and k_i (i > 0) is the generation dependent multiplication factor, or estimated in terms of fission multiplication as:

$$M_{ext}^{f} = 1 + \overline{u} N_{f},$$

where $\overline{u}$ is the average number of neutrons emitted per fission, and N_f is the number of fissions per spallation neutron. The resulting difference in neutron multiplication is then often parametrized in terms of the source neutron efficiency j_{i}^{*} defined as:

$$j_{i}^{*} = \frac{M_{ext}^{i} - 1}{M_{fiss} - 1}, \quad f = i, n$$

where $M_{fiss} = 1/(1 - k_{eff})$ denotes the fundamental mode neutron multiplication and k_{eff} denotes the k-eigenvalue of the neutron transport equation.

The external neutron multiplication factor k_0 was estimated for different Pb/Bi-target radii of the Pb/Bi or Na-cooled ADSs with infinite radial core lattice dimensions, see Figure 2-2.

An increase of target radius implies higher probability for axial leakage of neutrons which diminishes their chances to induce fission in the core. At the same time, a probability of neutron capture in the target and core increases as neutrons subsequently slow down; the median energy of neutrons exiting target drops from 910 keV to 680 keV as target radius is increased from 20 cm to 30 cm. Backscattering of spallation neutron is pronounced mainly in lead-bismuth cooled system which further slow down the neutrons. Increasing the pitch-to-diameter ratio of fuel lattice further degrades the efficiency of spallation neutrons. This is mainly due to the increased probability of their axial leakage, being as high as 12% for the Na cooled system at P/D=2.0. This is to be compared with only 6.0%, observed for the Pb/Bi-system.
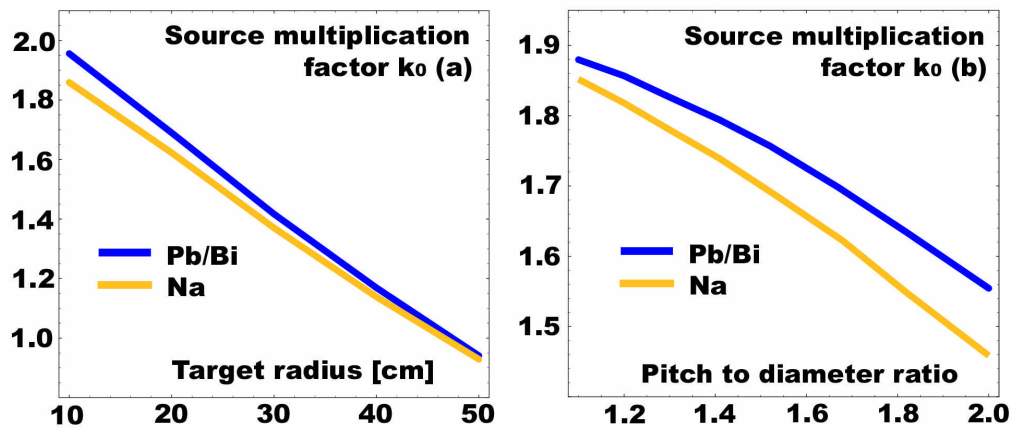
Figure 2-2. The external source multiplication factor as a function of target radius (a) and pitch-to-diameter ratio (b) for diluent and poison free radially infinite lattices cooled by lead/bismuth and sodium.

Maximum fission-to-absorption ratios are desirable if helium production in fuel pins is to be minimized. The potential of the boron carbide as a slow neutron shield was investigated by dispersing equal fractions of boron carbide and transuranium nitride in liquid metal coolants. As displayed in Figure 2-3 (a), the probability of direct fission of ^{241}Am increases with ^{10}B enrichment and reaches 0.5 for 50% ^{10}B enrichment in boron carbide. In realistic core designs with reasonable source neutron efficiencies and flat

power density distribution, the fission probabilities drop to 40% owing to the leakage of somewhat moderated neutrons from nearby fuel zones.

The dependence of the probability of direct fission on the coolant volume fraction is seen on Figure 2-3 (b). The decrease of direct fission probability is quite modest and values above 50% are still feasible for the larger pitches required by the poorer thermal properties of the lead/bismuth coolant (P/D ~ 2.0).

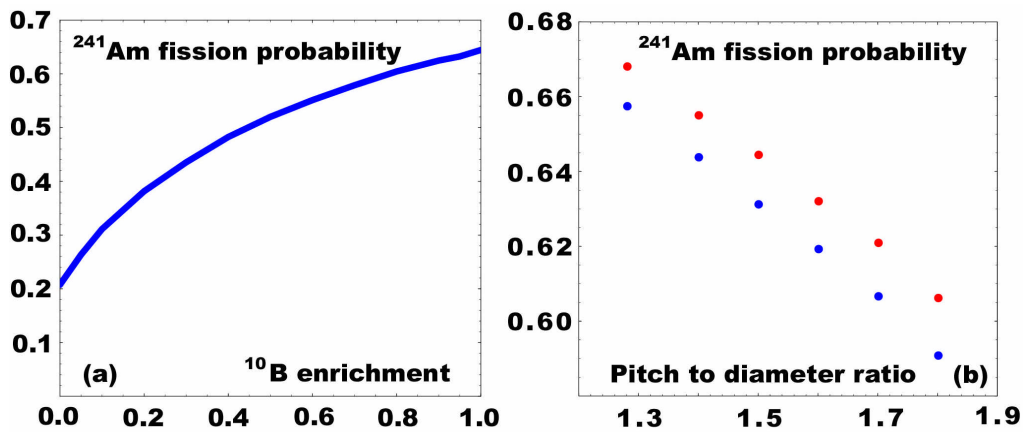Figure 2-3. The probability of direct fission of ^{241}Am as function of (a) ^{10}B enrichment in B_4C pins and (b) pin pitch-to-diameter ratios. Sodium (red point) yields slightly harder spectrum than Pb/Bi.

The design of the Sing Sing Core was thus accordingly improved in further studies. The radius of the target has been decreased to 20 cm while number of fuel zones was raised from four to twelve in order to allow for better differentiation in TRU and BA content. The burnable absorbers were removed from the vicinity of the target and placed only into fuel zones containing minor actinides. Outer fuel zones consist now of fresh plutonium and serves as a system driver, supplying neutrons into heavily poisoned transmutation zones.

A more detailed description of Sing-Sing core and its performance is given in **Appendix I.**

2.2   TEMPERATURE PROFILES OF THE SSC FUEL

Thermal hydraulic calculations were performed on the Pb/Bi cooled fuel pin bundle on the design of the 'Sing-Sing Core' described in [7]. In the region investigated a power of 75kW/m was generated in each fuel pin. The examinations showed that at the hottest spot the surface cladding reaches a temperature somewhat below the acceptable temperature of 893K where the protective oxide layer on the cladding is damaged [24] – as shown of Figure 2-4.These calculations also depicted a significant radial temperature drop of 80K in the Pb/Bi coolant. Better mixing of the coolant would probably increase the heat removal.

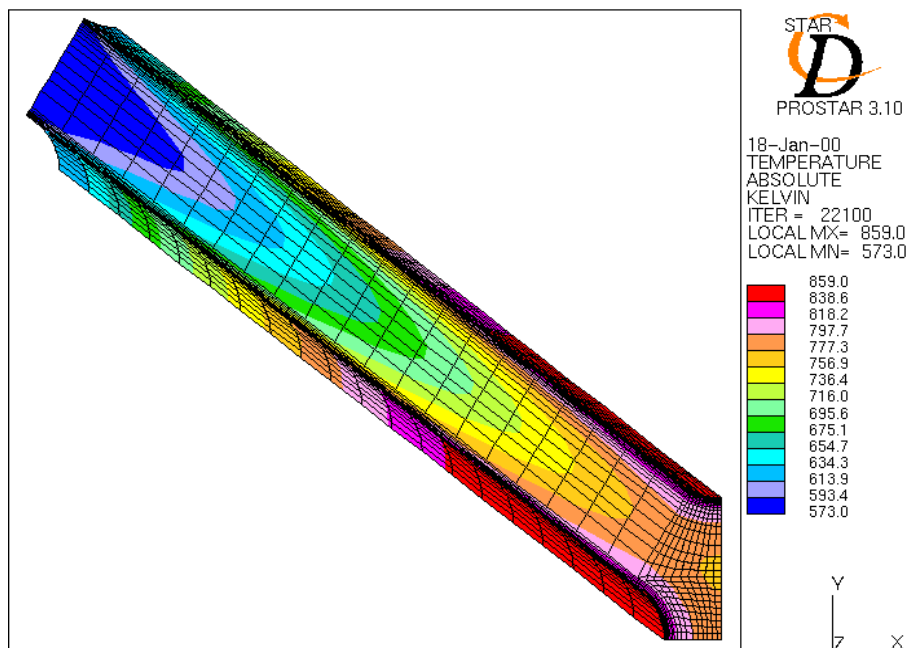**Appendix IV, section 7** describes these investigations in detail.

Figure 2-4. The temperature profile of the Pb/Bi coolant channel of the SSC

3   CORE ANALYSIS

A *beyond design basis* analysis of core behaviour under accidental conditions is presented here in order to assess problem potentially arising due to dissociation of nitride fuels taking place at elevated fuel temperatures. The formation and release of nitrogen gas from the core region would lead to a change in reactivity combined with an increase in cover gas pressure. It has been shown that certain core configurations may have difficulties in retaining safety margins should nitride dissociation occur [3], [4]. Therefore one needs to identify core geometries and/or fuel compositions providing a more benign behaviour in beyond design basis accident scenarios.

For this purpose fully three-dimensional Monte Carlo modelling of a) CAPRA type cores [1], [5] assumed to be operating on nitride fuel, and b) sub-critical minor actinide burners as proposed by JAERI [6] was performed The use of continuous energy Monte Carlo techniques allowed to accurately describe core states voided from nitrogen and/or coolant. The JEF2.2 cross section library was processed with NJOY (see chapter 6.2) for use in the Monte Carlo codes MCNP [28], MCNPX [33] and MCB (see chapter 6.1).

In the CAPRA core simulations, the fuel was assumed to consist of depleted uranium (60%) in conjunction with plutonium of degraded quality (40%). The fraction of $^{11}B_4C$ moderator pins was varied as function of pin pitch in order to obtain criticality at BOL with all shut down rods extracted. The nitrogen was taken to be of natural isotopic composition in a first series of simulations, and consisting of 99% ^{15}N in a second series. The active part of the core was then voided from all nitrogen and the k-eigenvalues were recalculated. The resulting change in reactivity is depicted in Figure 3-1, where it can be seen that the loss of natural nitrogen from the core indeed yields a signficant positive reactivity feedback for the CAPRA pin pitch (P/D = 1.20). However,

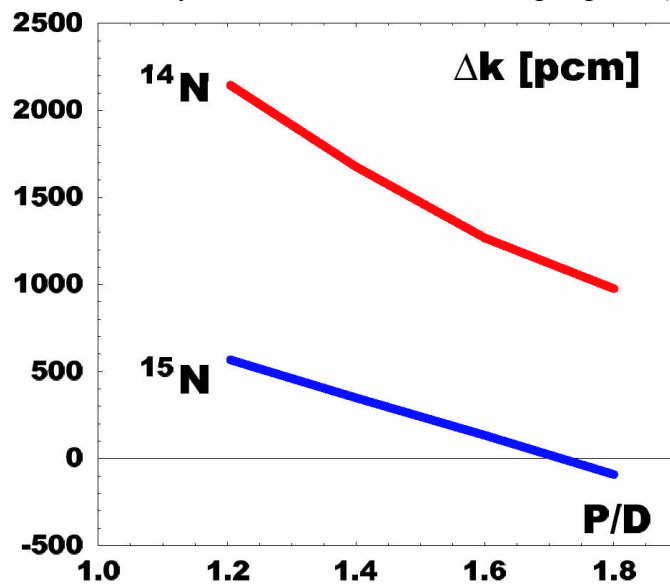*Figure 3-1. Nitrogen void worths in a (U,Pu)N fueled CAPRA core.*

with increasing pin pitch, the magnitude of the feedback decreases. In the case of ^{15}N enriched nitrogen, the change in reactivity is much smaller, since the influence of (n,p)

reactions in ^{14}N now is negligible, and only elastic scattering on ^{15}N contributes to the neutronics of the system. Increasing the pin pitch, the ^{15}N void worth even becomes negative, as the leakage component of the neutron balance starts to dominate.

When modeling the JAERI core, it was found that adopting equal molar fraction of zirconium nitride and transuranium nitride was consistent with the proposed average pin and core power (30 kW/m & 800 MWth, respectively). The minor actinide composition corresponded to that of light water reactor discharges after five years of cooling, and the plutonium fraction was varied in order to obtain a k-eigenvalue equal to 0.95, for each of the core configurations studied. Sodium and lead-bismuth coolants were included in the investigation. Figure 3-2 shows the change in eigenvalue resulting from decomposition of transuranium nitrides (ZrN was assumed to be stable) followed by escape of nitrogen gas from the core. The reactivity feedback decreases with pin pitch in all cases, with ^{15}N enriched nitrogen typically yielding 750 pcm lower values. It is interesting to note that nitrogen in a sodium cooled core has a significantly lower void worth than in a lead-bismuth cooled core. This is due to the poorer neutron economy (higher axial leakage) pertaining to sodium, which requires a higher fraction of plutonium in the fuel to obtain a given reactivity level in the non-voided state. Accordingly, the change in contribution of fast fissions to the neutron balance when voiding the core becomes smaller.
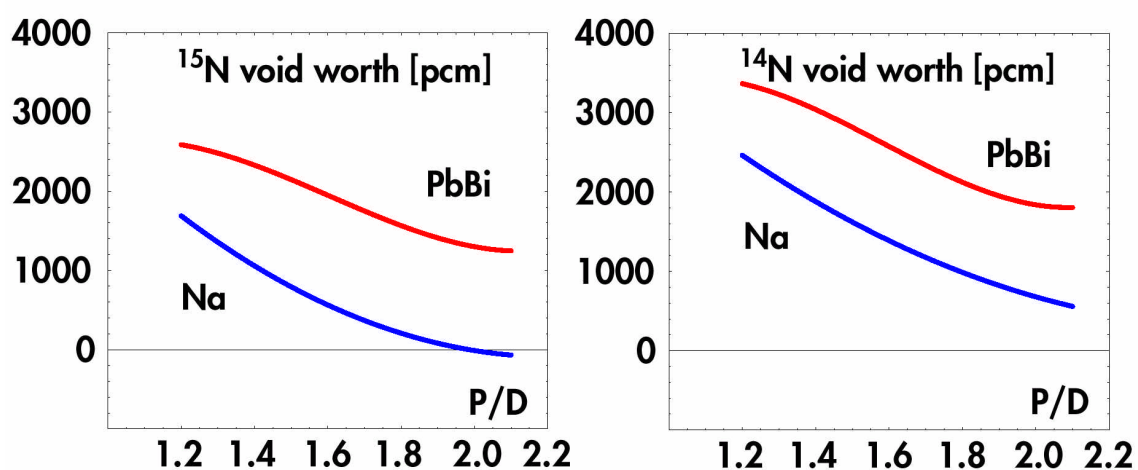
Figure 3-2. Change in k-eigenvalue assuming decomposition of transuranium nitrides and escape of nitrogen gas from cores cooled by sodium and lead-bismuth.

Considering that the loss of nitrogen from the core may be accompanied by loss of coolant, one needs also to evaluate the combined coolant and nitrogen void worths. Figure 3-3 shows the change in reactivity obtained when voiding the JAERI core types from ^{15}N and coolant in the *active core region*. The combined void worth is smaller than the sum of the independent nitrogen and coolant worths, as expected from the increase in axial leakage. The decrease with pin pitch is also stronger, and the combined void worth becomes smaller than the larger of the individual worths for pin pitches larger than 1.7.

The following preliminary conclusions from the calculations performed on nitrogen void worths can thus be made:

The use of ^{15}N enriched nitrogen, which is a prerequisit within the context of partitioning and transmutation, will diminish the maximum change in reactivity possible
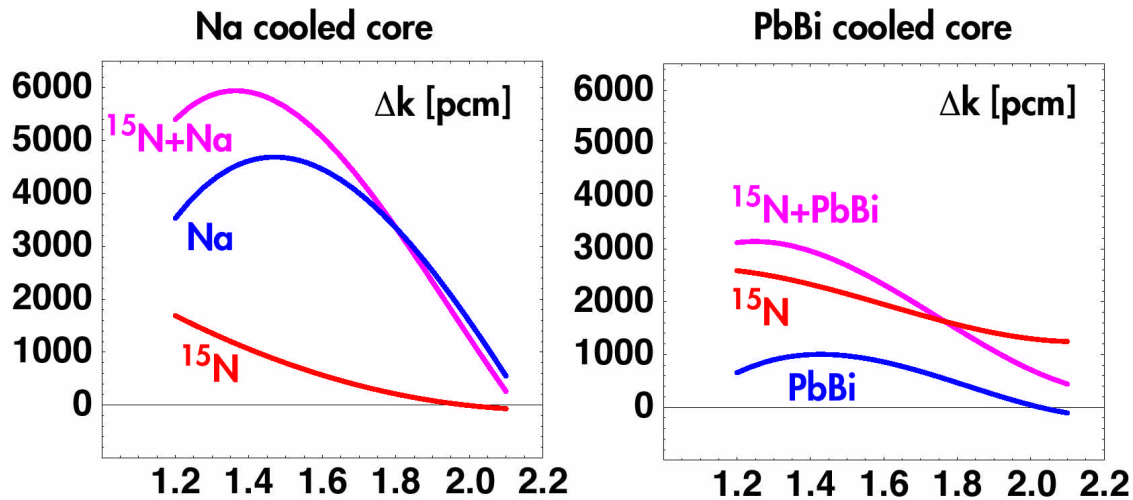
Figure 3-3. Change in k-eigenvalue for simultaneous voiding of coolant and ^{15}N enriched nitrogen from the active part of the core.

if nitrogen gas should escape the core. Simultaneously increasing the pin pitch above 2 times the pin diameter can yield negative nitrogen void worths for coolants providing high axial leakage factors. With lead-bismuth coolant, the ^{15}N void worth remains at a level of 1000 pcm for the JAERI core here investigated

As an increase in pin pitch must be accompanied by an increase in plutonium fraction, lead-bismuth cooling still appears to be preferential even at large pin pitches. A Pu fraction of 40% corresponds for instance to P/D = 1.5 at k = 0.95 in the sodium cooled version of the JAERI core, while using lead-bismuth coolant leads to P/D = 1.8. The sodium void worth at P/D = 1.5 being larger than 5000 pcm, however would demand operation at even lower k-eigenvalues, with severe impact on the power economy of the system. In the next phase of this safety analysis, reactivity losses will be calculated as function of pin pitch, in order to find an optimal compromise between void worths and reactivity losses.

Calculations of cover gas pressures resulting from escape of nitrogen from the core have not yet been done, but it is expected that the relatively low inventory of nitrogen in the JAERI core will make it less vulnerable than the CAPRA core for such events.

More detail description and results of these investigations is given in Appendix II.

4 DYNAMICS OF ACCELERATOR-DRIVEN SYSTEMS

4.1 INTRODUCTION

This chapter deals with dynamic and safety issues of ADS and it serves as an introduction to some safety related questions that are characteristic to source-driven nuclear energy systems. The chapter is basically divided into two parts. In the first part, evidence of some distinguishing kinetic features of the ADS is provided and discussed. Some of the dynamic properties, that characterize the ADS and demand a unique safety approach are pointed out. One attribute that is intrinsic to subcritical systems is the large difference in response time between the power and the thermal reaction time of reactor components. Some simple examples are performed to demonstrate these qualities. A lumped heat capacity method is used to gain physical insight into the transient behavior of fuel pins. In the second part, safety characteristics of our specific ADS-core design have been investigated. The SAS-DIF3DK computer code is applied to the analysis of transients imposed by source insertion and to Loss of Coolant Flow. Discussion is made on the optimization that has been performed in order to increase the amount of natural circulation flow and increase the safety margins in the event of an accident.

During the year of 2000 a collaboration was initiated with the Division of Reactor Analysis and Engineering at Argonne National Laboratory, USA. The object is to jointly address safety and dynamics issues of accelerator-driven systems. The Argonne National Laboratory (ANL) has for long played a major role for advancing the design and operation of nuclear energy systems in the United States. The laboratory has developed computational tools for characterizing the performance and safety features of advanced reactors. More recently it is involved in the development of accelerator-driven systems. ANL has enhanced existing computer codes to facilitate the investigation of safety characteristics in heavy-metal cooled subcritical systems.

4.2 SUBCRITICAL REACTOR DYNAMICS

There are important differences in the dynamic behavior between critical reactors to the class of subcritical reactors (or ADS). While the critical system maintains a self-sustaining chain-reaction on its own, the ADS must be fed with additional neutrons from an external neutron source to assume a steady power level. The fact that the ADS is driven by an independent neutron source, that is unaffected by the conditions in the reactor, have a strong influence on the kinetics behavior, control, and stability characteristics of such systems.

The kinetic performance of a source-driven system is well described by the inhomogeneous point kinetics equations [7]. The solution for one group of delayed neutrons is as follows (see chapter 4.5 for additional details).

$$p(t) = -\frac{s}{r} + \frac{s+r}{r-b}e^{\frac{r-b}{\Lambda}t} + \frac{b}{b-r}\left(\frac{s}{r}+1\right)e^{\frac{\bar{l}r}{b-r}t}$$
<div align="right">4-1</div>

where the reactivity, ρ, is a measure of the amount of off-criticality and is defined as

$$r = \frac{k_{eff}-1}{k_{eff}}$$

In a subcritical state, the effective multiplication factor k_{eff} (eigenvalue) is less than unity and ρ is negative. The notation being used follows the recommendations outlined in ref. [7]. The solution is applicable to an ADS with an external neutron source that is initially in a stationary state and that is subject to a step change in reactivity and/or source power. The solution contains one constant term and two exponential terms. The first term characterizes the constant external source, the second term describes the rapid transition to a quasi-static level, the "prompt jump" or "prompt drop" level, and the last term involves the delayed neutron response.

In an ADS the reactivity is largely offset from criticality, in most ADS sample designs usually by more than 20 times the delayed neutron fraction. The net result is a *substantially reduced sensitivity of the subcritical system to any reactivity disturbance* compared to a critical reactor. To illustrate the impact of subcriticality on the dynamic response of source-driven systems, a reactivity insertion transient is shown in Figure 4-1. One critical system, and three subcritical systems with varying degree of subcriticality (k_{eff}=0.95, 0.995, and 0.9995) are subjected to a reactivity increment of 10 cents. The delayed neutron fraction is assumed to be 0.0020, hence, 10 cents correspond to 0.0002 (20 pcm). Transient response is obtained using eq. 4-1.
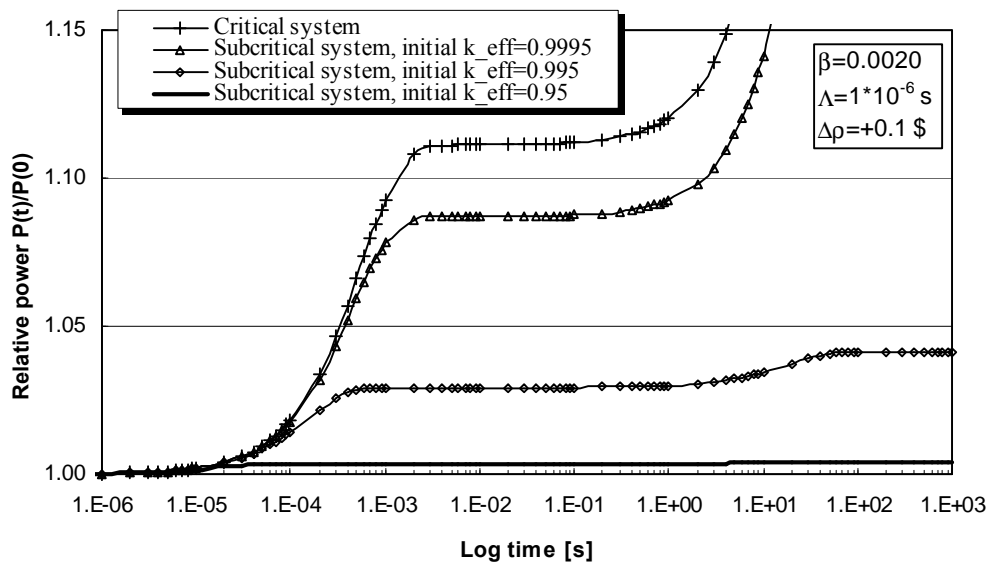
Figure 4-1. Transient response of an ADS subject to a reactivity insertion of 10 cents. Notice the very small response in the deeply subcritical system (keff=0.95).

Clearly, for an equivalent reactivity increment, the deeply subcritical system (k_{eff}=0.95) experiences a minor power increase whereas the critical system suffers a strong power excursion. What is also obvious from Fig. 4-1 is that for a reactivity disturbance (as long as ρ stays in the subcritical regime) to an ADS, the power will eventually approach

a new stationary level (for the subcritical system, k_{eff}=0.9995, the power assumes a steady level that is outside the plotting area); whereas in a critical reactor (absent reactivity feedbacks) a change in reactivity leads to an exponential increase in power. This is also realized by inspecting 4-1. In a subcritical state both exponential factors in eq. 1 approach zero when transient time approaches infinity. Accordingly, both exponential terms vanish and the power asymptotically assumes the value of the constant term given by

$$p(t) = -\frac{s}{r} \quad \text{"new stationary level"} \qquad\qquad 4\text{-}2$$

This behavior includes transients involving variation in source intensity or source importance as well. If the source power is increased by twice the initial power, the reactor power will be amplified by a factor of two. If the source is reduced to half the initial intensity, the power will assume a stationary state at half the initial power, and so on.

In Figure 4-2, the previous transient in the deeply subcritical system (k_{eff}=0.95) is examined in more detail.
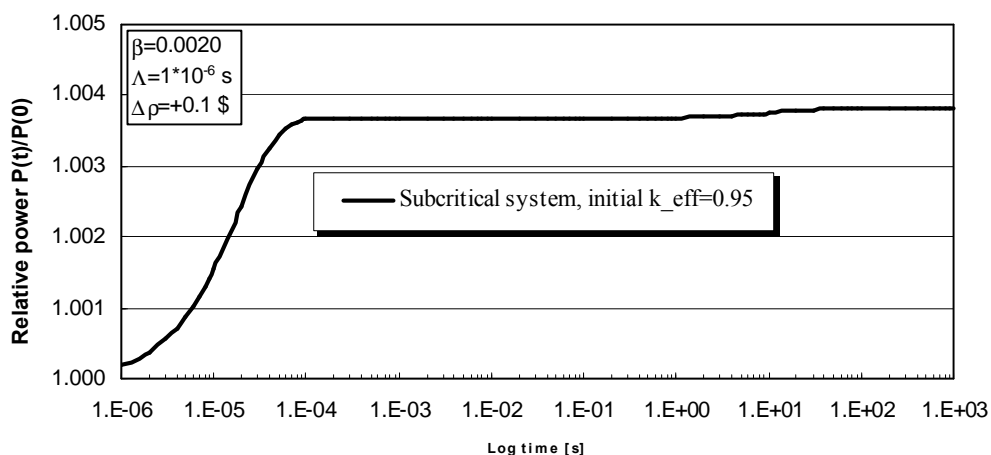
Figure 4-2. 10 cents reactivity insertion in a deeply subcritical system (k_{eff}=0.95). Notice the very rapid response to a reactivity disturbance.

Following a reactivity insertion, the ADS responds with a rapid transition, a prompt jump, to a quasi-static level. How fast this transition proceeds is determined by the prompt period. It is not until the transient reaches the time frame of seconds that a small influence of the delayed neutrons appear. The delayed neutrons only contribute with a small change in power in an ADS.

The prompt jump phenomena is not unique to the ADS, it occurs in any nuclear reactor. The unique behavior, however, of an ADS is that the quasi-static level assumes a value which is very close to the asymptotic level. Examining eq. 4-1 we may get a mathematical expression for the magnitude of the quasi-static level. During the prompt jump the first exponential term in eq. 4-1 quickly approaches zero and drops out. The exponential factor in the last term assumes a value close to unity and is virtually unchanged during the prompt jump. When simplifying eq. 4-1 under those conditions, it is found that the magnitude of the quasi-static level is given by [7]

$$p_{pj} = \frac{s + b}{b - r} \quad \text{``prompt jump level''} \qquad\qquad 4\text{-}3$$

An ADS, with a substantial subcriticality margin, adjusts to an intermediate level that is very close to the final, asymptotic, level. The level of subcriticality has a large influence. This is clearly seen in Figure 4-1 where the system which is close to critical (k_{eff}=0.995) reaches a prompt jump level which is smaller relative to the asymptotic level. Delayed neutrons play an increasing role when the system approaches critical conditions.

The prompt jump is the initial response of the prompt neutrons to adjust to a new state. The time constant for this rapid transition is determined by the prompt period.

$$T_{prompt} = \left| \frac{\Lambda}{r - b} \right| \qquad \text{[s]} \quad \text{``prompt period''} \qquad\qquad 4\text{-}4$$

The prompt period is the time required for the power to change by a factor of e. Since the overall magnitude of ρ is considerable larger than β, the prompt period is mostly determined by the mean neutron generation time, Λ, and the reactivity, ρ, itself. In fact, the influence of delayed neutrons to slow down the transient is negligible in an ADS. On the contrary, the response is dominated by the feedback of prompt neutrons rather than by delayed neutrons. The reason is not because the delayed neutron fraction, in general, is smaller in ADS, rather the delayed neutron source is small in comparison to the source of external neutrons. The net result is that *delayed neutrons have no significant influence on the overall transient response in a deeply sub-critical reactor*, quite different from the response in a critical reactor where delayed neutrons are of great importance for control. The ADS is essentially operating on prompt neutrons and source neutrons alone.

The above mentioned dynamic features of source-driven systems give rise to some unique control and safety related issues that require different design approaches compared to critical reactors. For example, the fact that the ADS is largely insusceptible to reactivity perturbations has a direct consequence on the effect of thermal feedbacks that normally couples back to the reactivity in a nuclear reactor. The impact of such feedbacks will be much smaller in an ADS compared to any critical system. A simple calculation may illustrate this.

IMPACT OF REACTIVITY FEEDBACK ON COOLANT TEMPERATURE

The asymptotic power level in an ADS following a reactivity change is determined from the source multiplication formula.

$$P = P_0 \cdot \left| \frac{s}{r} \right|$$

where P is the asymptotic power, P_0 is the initial power, s is the relative strength of the independent source, and r is the subcritical reactivity in the new asymptotic state.

The axial increase in coolant temperatures in the core channel is determined from

$$(T_{out} - T_{in}) = \frac{P}{w \cdot c_p} = \frac{\text{Total power} [W]}{\text{Coolant flow rate} [kg/s] \cdot \text{Coolant specific heat} [J/kgK]}$$

where w is the coolant flow rate, and c_p is specfic heat of the coolant. Assuming that the inlet temperature and flow rate is the same, the coolant outlet temperature in a new asymptotic state following a reactivity perturbation is given by

$$T_{out} = \left| \frac{s}{r} \right| \cdot \frac{P_0}{w \cdot c_p} + T_{in} = \left| \frac{s}{r} \right| \cdot (\Delta T_{cool})_{initial} + T_{in}$$

Results of the above relation is displayed in Table 4-1. An initial temperature difference of 100 K between core inlet and outlet is assumed. The increase in coolant outlet temperature following a reactivity insertion is calculated for two reactivity increments. Results are tabulated as a function of subcriticality.

Table 4-1. Increase in coolant outlet temperatures [K] following reactivity insertion. It is assumed that initial coolant ΔT=100 K. Inlet temperatures and coolant flow rate is constant. 1\$=0.0020.

Initial k_{eff}	1\$ insertion	2\$ insertion
0.950	4 K	8 K
0.975	8 K	18 K
0.995	66 K	390 K

Temperatures in Table 4-1 are those obtained in the asymptotic state if the power would increase without any constraining feedbacks. Remembering that the time to reach asymptotic power in an ADS is determined by the prompt period, then the time to attain asymptotic coolant temperatures is determined by the coolant transit time (which normally is about half a second in a Pb/Bi cooled ADS). In this simple analytic treatment any thermal feedback effects such as Doppler, void, and dimensional changes that presumably would mitigate transient response have been neglected. The effect that those might have on the deeply subcritical system (k_{eff}=0.95 and k_{eff}=0.975) in this example can be disregarded considering previously mentioned reasons. For the close-to-critical system (k_{eff}=0.995) feedback effects would necessarily have to be taken into account in order to obtain the correct asymptotic temperature. However, the example still gives a qualitative insight into the thermal response of an ADS subject to reactivity changes.

In critical reactors reactivity feedbacks in combination with delayed neutrons are used to balance heat generation and heat losses and to obtain a smooth control of power. For example, in a PWR smooth power variation and cycling is achieved by adjusting the turbine throttle, which in turn alters the temperature and density of the primary coolant. Subsequently, thermal and hydraulic feedbacks act on reactivity to give an even change in power. In a fast reactor, the control rod position is adjusted. Critical systems rely on delayed neutrons and smoothly varying feedbacks to level out reactivity disturbances. Since delayed neutrons as well as reactivity feedbacks only have a weak importance, in terms of influencing the dynamic behavior in an ADS, other means for control must be used. If, for example, the ADS is subject to an increase in coolant inlet temperature due to a failure in the heat sink, then the reactivity feedbacks that follow will have a minimal influence on the power. Unless a much stronger feedback is introduced, temperatures in the reactor will be more or less unaffected by the feedback. One obvious solution would be to change the source strength or source importance. The source is linearly proportional to the power, 10% increase in source strength yields 10% increase in power, and so on. Compared to reactivity changes, it is easy to accomplish a 10% change of source power by adjusting the beam power output from the accelerator. However, source changes will lead to extremely abrupt power changes in the subcritical reactor.

4.2.1   Time constants

Some general properties for the thermal behavior of reactor components under transient conditions may be obtained by studying their characteristic time constants. The time constant is a measure of how fast these components will respond to changes in the power generation. The time constants affect the energy buffering ability as well as the time for various reactivity feedback mechanisms to take effect. For example, it is useful for evaluating such things as the time taken by the fuel to cool down or heat-up following a power transient.

Reactor period

By definition, the reactor period (or e folding time) is the time required for the power to change by a factor of e. Below, the reactor period of a fast critical reactor is compared with the reactor period of an ADS.

CRITICAL REACTOR

The average decay constant of all the delayed neutron precursors is given by

$$\frac{1}{\overline{l}} = \frac{1}{b} \sum_{k=1}^{6} \frac{b_k}{l_k}$$

For fissioning of ^{239}Pu in a fast spectrum $\overline{?} = 0.075 \ s^{-1}$

(an alternative weigthing method could be used, $\overline{l} = (\sum l_i b_i) / b$, which would result in $\overline{l} = 0.410 s^{-1}$)

Following a subprompt reactivity insertion the critical reactor responds with a initial, small, prompt jump followed by a slow, stable period given by

$$T_{period} = \frac{b - r}{\overline{l} \ r}$$

considering a transient in a critical reactor with, $r = +0.0010$ and $b = 0.0020$,

$T_{period} \approx 13$ seconds

(In the case of a power decrease, the period is negative, and its magnitude is the length of time required to for the power to decrease by a factor of e.)

ADS

The sub-critical reactor responds immediately with a time constant given by the prompt period

$$T_{period} = \left| \frac{\Lambda}{r - b} \right|$$

assuming similar values as in previous illustrations, $\Lambda = 1 \cdot 10^{-6}$, $r = -0.05$ and $b = 0.00200$

$T_{period} \approx 20 \ ms$

Following an unbalance in source or reactivity, the reactor period drops from typical 10 seconds in a fast reactor to microseconds in an ADS. It is realized that the ADS responds rapidly to any disturbance. Therefore the ADS requires faster operating control and protective systems to ensure an acceptable response to source, reactivity, and flow disturbances. The rate of power increase is so rapid that only a prompt negative reactivity feedback from the rising fuel temperature would be able to control the power. Prompt reactivity feedback (Doppler) appears immediately with changes in reactor power and it is directly related to changes in fuel temperature. Delayed contribution to reactivity feedback comes from the effects of changes in the temperature of coolant or other core components besides the fuel. For the delayed feedbacks there is a delay between the time of power production and the time of component temperature rise that is determined by the time to transport heat from the fuel to the components.

Lumped time constant of fuel pin

A change in power results in temperature changes in the fuel, coolant, and structure. Evaluation of the characteristic time constant of the component gives a measure of the thermal response time. It depends on the thermal properties of the pin and coolant, and

also on the coolant velocity and lattice parameter. To find an expression for the time constant of a solid exposed to a heat sink we apply the "lumped heat capacity method". For the fuel pin this gives [8]

$$\frac{\overline{T}(t)-T_{\sin k}}{T_0-T_{\sin k}}=e^{-\frac{U}{C_f}t}$$ 4-5

where $\overline{T}(t)$ is the average temperature in the fuel, T_{sink} is the temperature of the heat sink [K] (normally the coolant), C_f is the heat capacity of the fuel pin [J/kgK] per unit length, and U is the overall heat-transfer coefficient [W/K] per unit length. The time constant, τ [s], is the time it takes for the temperature difference between the heat sink and average temperature of the fuel to change by a factor of $1/e$ (36.8 % of the initial difference). The fuel time constant then becomes

$$t_f=\frac{C_f}{U_f} \quad [s]$$ 4-6

Even though the lumped heat capacity method is simple in its treatment it is sufficient in many cases. Often the convective heat-transfer coefficient contain large uncertainties and to apply more detailed methods may be unnecessary. Numerical values for the fuel time constants based on sample design data of the SSC [7] fuel pin design are presented in 0 (see chapter 4.5 for detailed information on calculations). Average temperature is calculated from the temperature distribution of a hollow fuel pin (id=2 mm, od=5.88 mm). Heat capacity and thermal resistance for the fuel, bonding, and cladding are treated separately. The convective heat-transfer coefficient, is calculated using the Lyon-Martinelli correlation [10] for flowing liquid metal along a tube wall. Constant thermophysical properties are assumed. No direct thermal contact between the fuel itself and the cladding is assumed (open gap).

Table 4-2. Characteristic time constants of the SSC fuel pin

Property	t_f [s]
Pb/Bi bonding, v=2.5 m/s, P/D=1.75	0.46
Pb/Bi bonding, v=2.0 m/s, P/D=1.75	0.48
Pb/Bi bonding, v=1.5 m/s, P/D=1.75	0.51
Pb/Bi bonding, v=2.5 m/s, P/D=2.19	0.49
Na bonding, v=2.5 m/s	0.44
He bonding, v=2.5 m/s	1.74
N_2 bonding, v=2.5 m/s	7.13

For a liquid metal bond, the time constant is at the most 0.5 seconds. The presence of a liquid metal bond between the fuel and the cladding significantly reduces the fuel time constant. Therefore, heat is rapidly transferred from the fuel into the coolant. In general,

it is desirable to have a short time constant in order to diminish the temperature increase in the fuel region.

The flow velocity and the pitch-to-diameter ratio have only a weak influence on the time constant of the SSC fuel. In liquid metals the conductive heat transfer dominate over momentum heat transfer and much heat-transfer may occur even at low flow velocities.

In a subcritical reactor the power level changes much faster compared to the time constants involved in typical heat-transfer processes, for example the time required to transport heat out of the fuel pin. In comparison with the prompt period, the entire power change take place over a short enough time span that the fuel may be considered to behave adiabatically, with no heat transport taking place. This puts a requirement on the ability of the fuel to store large amounts energy. In other words the fuel should preferably accommodate high failure temperatures, be structurally resistant to temperature changes, and have high heat capacity in order to store energy without a sharp increase in temperature.

4.3   ACCIDENT ANALYSIS

In this section an initiatory accident analysis [11] is performed on a model of a Swedish design for an 800 MWth accelerator-driven system. The analysis investigates the consequences of the following type of accident events

1) a *source insertion* or a *source jerk* type of accident where the external neutron source is promptly increased by a factor of two. In an ADS this would correspond to inadvertent control of the proton beam. In the envisioned ADS design, reactor transients may be caused by a relatively fast insertion or removal of the accelerator beam [12]. The possibility for adjusting beam power during operation is a design requirement in order to facilitate compensation for reactivity losses during burnup. Therefore, source jerk type of accidents is not unrealistic in the envisioned ADS.

2) a *protected Loss of Flow* (LOF) type of accident. In this case it is assumed that all centrifugal pumps fail to operate at the same time and coolant flow rates is driven by buoyancy forces alone. It is supposed that the beam is shutoff at the same instant when pumps fail. In that case total power rapidly drops to decay heat levels. Simultaneous failure of all the pumps because of power failure is not unlikely, common cause failure could cause failure of the supply of power to all the coolant pumps.

3) an *unprotected Loss of Flow* (ULOF) type of accident. In a normal loss of flow event the plant protection system would automatically switch off the accelerator or at least divert the beam from entering the core, however, in this case it is assumed that the accelerator continues to feed the system with protons. The ADS will remain at full power for the complete transient while the flow drops.

In all events, normal heat sink operation is assumed. If no heat sink is available, natural circulation flow will drop and eventually cease.

Thermal conditions of fuel, cladding, and coolant are analyzed. The SAS-DIF3DK computer code is used to obtain transient results. Possible safety consequences are

considered with respect to a set of postulated failure criteria, see Table 4-3, based on maximum allowable temperatures in reactor components.

Table 4-3. Thermal failure criteria for the SSC

Component	Failure criteria
Fuel, dissociation of PuN	2150 K (2800K in N_2 environment)
Fuel, dissociation of AmN	1570 K
Cladding, steel melting point	1700 K
Cladding, corrosion	900 K (extended operation)

4.3.1 General code description

The SASSYS-DIF3DK [13] code couples reactor thermal hydraulics treatment with a 3D spatial kinetics treatment [14]. Time-dependent neutronics calculations may rely on either a point kinetics or a 3D spatial kinetics treatment [15]. In the spatial kinetics treatment neutron distributions are calculated using either transport theory [16], [17], [18], [19] or diffusion theory. The code solves the multi-group time-dependent neutron balance equations with or without external neutron source.

The thermal/hydraulics treatment [20] in SASSYS-DIF3DK calculates detailed 3-dimensional temperatures and material densities. The code uses multiple channels (the term "channel" is used to denote collectively the fuel pin, cladding, associated coolant, and structure) to model a whole-core representation. Heat transfer in each fuel pin is modeled with a two-dimensional (r/z) heat conduction equation. The core assembly thermal hydraulics treatment in SASSYS-DIF3DK includes the calculation of fuel, cladding, and structure temperatures, as well as coolant flow rates and pressure distributions in each channel. Both steady-state and transient temperatures and coolant pressures are calculated. The code handles forced convection as well as free convection heat and mass transfer. Primary and secondary coolant circuits and their mechanical components may be included into the model. The code is adapted to model either sodium, lead, or lead/bismuth as coolant. Thermophysical properties, heat transfer correlations, and fluid dynamics correlations are embedded in the code. The code has limited ability to analyze core disruptive accidents.

4.3.2 Model and Assumptions

The SSC [7] (Sing-Sing Core) is a model of an ADS developed at the Royal Institute of Technology, Sweden. The model considered in the present accident analysis is rated for a thermal power of 800 MW and it is cooled by an eutectic of liquid lead/bismuth. The fuel consists of plutonium and minor actinides contained in a zirconium-nitride based matrix. No fertile material is present in order to maximize transmutation rates and to avoid production of new heavy waste nuclides. Separate pins of neutron absorbers, B_4C, are located within the core. Boron carbide pins are used to achieve a flat power profile at begin of life and to compensate for reactivity losses during burnup. The boron carbide is highly enriched in [10]B due to its benign neutron capture properties which helps to increase fission to absorption probability in even neutron numbered nuclides [7]. The design uses fixed absorber pins, separate from the fuel, that are radially zoned. Cross-section of the SSC layout, somewhat different than on Fig. 2-1, is illustrated in Fig. 4-3.

The use of fixed absorber pins is advantageous since it does not necessitate to fabricate pins of different composition. Pins are positioned in a triangular pin configuration. The fuel pins are hollow in order to reduce peak temperatures. Nitride fuel is employed to obtain high thermal conductivity and to allow for high linear ratings. The nitride fuel is highly enriched in ^{15}N to avoid the high capture cross section of ^{14}N and to minimize the accumulation of radioactive ^{14}C in the fuel. Major design parameters are displayed in Tables 4-4 and 4-5.
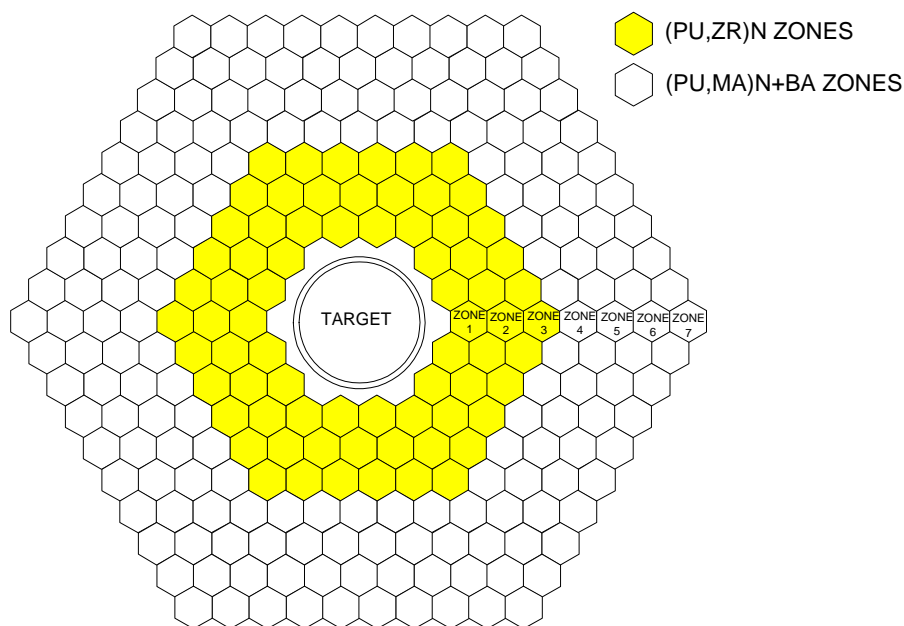
Figure 4-3. Core map of the SSC. Darker regions contain (Pu,Zr)N and light regions contain (Pu,MA)N and burnable absorber pins.

Table 4-4. Major system design data of the SSC used in SAS modeling

Total reactor power	800 MWth
Beta effective	0.0017
Mean neutron generation time	1.0e-6
Initial k_eff (eigenvalue)	0.970
Active core height	1.00 m
Fuel porosity	15%
Pellet inner radius	1.00 mm
Pellet outer radius	2.40 mm
Cladding inner radius	2.49 mm
Cladding outer radius	2.94 mm
Inlet coolant temperature	573 K
Coolant flow velocity	2.5 m/s
Flat-to-flat distance	9.90 cm
Pitch between subassemblies	10.10 cm
Cladding	Ferritic steel
Thermal bond (fuel to cladding)	Pb/Bi
Direct heat deposition in coolant	9%
Direct heat deposition in cladding	1%

Table 4-5. Fuel subassembly data of the SSC

Zone	P/D	Fuel pins/ subassembly	BA pins/ subassembly	[kW/m per fuel pin]
1	2.19	61	0	52
2	2.19	61	0	52
3	2.19	61	0	52
4	1.75	41	50	51
5	1.75	64	27	49
6	1.75	70	21	48
7	1.75	84	7	45

Integral reactor properties such as mean neutron generation time, effective delayed neutron fraction, and neutron flux distributions are obtained from MCNP calculations performed at steady-state condition. The transuranic fuel with a large fraction of minor actinides exhibits a low effective delayed neutron fraction. ^{239}Pu, with a low yield of delayed neutron precursors, dominates the fission rate. Since the delayed neutrons are emitted at energies lower than that of prompt neutrons their importance with respect to leakage and fission is different. The average importance of the delayed neutrons is smaller than that of prompt neutrons in the SSC. The effective β value in the SSC is lower because delayed neutrons have a smaller chance of causing fission in even-numbered nuclei since most delayed neutrons have energies below the threshold energy for fast fission. Moreover, the prompt yield of ^{239}Pu, increases with energy, which also gives prompt neutrons higher importance than delayed neutrons. In addition, the existence of absorbers in the core increases the probability for capture of delayed neutrons in ^{10}B.

A high pitch-to-diameter ratio increases the amount of natural circulation and reduces the potential for flow blockage. A large degree of natural circulation also has the benefit of self-distributing the flow radially to maintain relatively uniform coolant rise across all positions of the core. The SSC is designed to provide considerable natural circulation to ensure that heat removal capability is available in loss of flow events.

The core, heat exchanger, and primary pumps are immersed in a single pool of lead/bismuth. The primary heat exchangers are the steam generators. Four primary pumps are located in the cold pool. An illustration of the SSC vessel and primary system is displayed in Figure 4-4.Temperatures in the coolant range from 573 K at inlet to 761 K at the outlet in steady-state. Because liquid lead/bismuth is nearly incompressible, a vapor volume is provided to accommodate thermal expansion of the fluid; otherwise expansion may rupture the primary system if the temperature increase is sufficiently large. The coolant is kept at a low pressure, slightly above 1 atmosphere. Since the saturation temperature of lead/bismuth is high, even at atmospheric pressure, there is no need to pressurize the primary system. Rather, as shown in Figure 4-4, the reactor vessel is filled with lead/bismuth to a prescribed level, with the remainder of the vessel being occupied by an inert cover gas. The compressibility of this cover gas permits the lead/bismuth to expand with increasing temperatures.

Natural convection is promoted by a large separation distance between the heat exchanger and core mid-plane. Therefore, the steam generators are elevated well above the core. The drawback is that a large separation distance requires an increased vessel size which penalizes the economics of the plant and increases the seismic loading on the vessel.
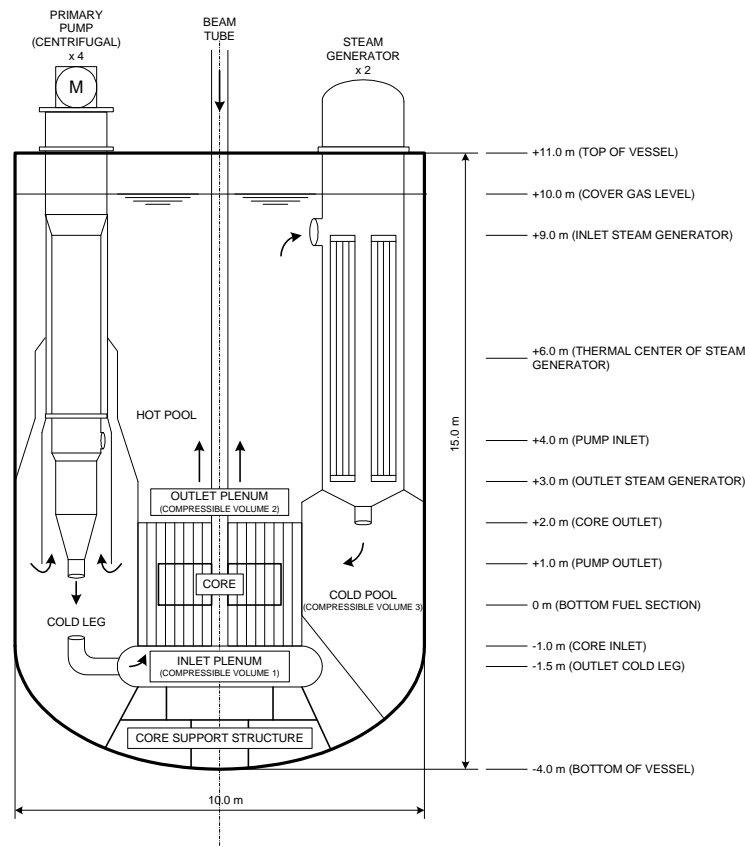
Figure 4-4. SSC 800 MWth primary circuit (pool type system)

Assumptions

The initial safety assessment calculations of SSC may be rather crude because of the uncertainties involved in many of the parameters. Instead, a simple model is used to identify the particular operating and safety characteristics, to define where further studies ought to be performed, and to define failure mechanisms and possible ranges of safe operation. As the design and safety evaluation proceeds the design will solidify as model parameters are updated continuously. Once a conceptual design is defined, it is suitable to carry out more elaborate calculations.

For the present purposes the SAS code is set up to run in point kinetics mode. There are some obvious drawbacks of using point kinetics in large and loosely coupled systems (especially thermal systems), which exhibit strong flux tilting. However, the present ADS is a small, strongly coupled core with a very hard spectrum. Space-time effects in such cores are very small and point kinetics theory is known to predict total power very well. This simplification is justified because of relatively large neutron mean free paths in SSC, which allows for the spatial shape of the flux to be quickly established following a reactivity perturbation.

Secondly, thermal feedback effects are not incorporated into the model. There are two main reasons that justify this simplification. In a typical heavy-metal cooled system coolant density changes gives a negative feedback, if however, neutron absorbers are present, coolant density changes increases the fission probability in even neutron numbered isotopes and less neutrons are captured in ^{10}B. Thus, in the SSC design, the

net result of coolant density changes is a slight positive feedback. Since the core contains no fertile fuel the Doppler feedback is negligible. In a pre-disruptive phase, no strong (negative) reactivity feedbacks exist in the present SSC design. Typically, strong reactivity feedback in a fast reactor originate from Doppler, coolant density changes, and thermal expansion of structure, however, in the SSC design those reactivity effects are much lower. Moreover, as discussed previously, even if strong reactivity feedbacks are present in the ADS, the impact they have on the power is significantly smaller compared to a fast reactor.

Constant steam generator boundary conditions are assumed, any influence from secondary circuit components are neglected. During all circumstances a constant inlet temperature of 573 K is assumed. This is equivalent of assuming that the steam generator removes heat at the same rate as it is produced, which is generally not the case. The impact of introducing this simplification depends on the investigation being made. If, for example, a rapid power variation is the phenomenon under consideration, it will be adequate to assume that the inlet temperature is constant. However, for "long" transients, in this case longer than the primary coolant loop time, an increase in coolant outlet temperatures will eventually influence coolant inlet temperatures. In a loss of flow condition this simplification has a low importance. In a source transient the assumption is not negligible and it must be taken into consideration when evaluating the safety consequences.

The decay constants for the delayed neutron precursor groups, λ's, do not differ markedly among fissionable isotopes, hence, a single set given by the lambda's of ^{239}Pu is used throughout the kinetics calculations. Direct γ heating of the structure is accounted for in the SAS model.

4.3.3   Loss of Flow accident

In the event of failure of all primary coolant pumps, the pressure drop across the core decreases, causing decreased mass flow rate. It is assumed that the pump coast-down occur in all pumps simultaneously. Pump failure due to loss of power does not result in an instantaneous loss of pressure head, since even if the pump motor suddenly fails, the rotational inertia of the pump impeller and fly wheel will cause the pump to coast down gradually over a period of time. Figure 4-5 shows the flow rundown due to loss of all electrical power to all four primary pumps in SSC. This figure contains the flow reduction in SSC following a LOF accident in case a) the beam is shut-off, b) the beam still on.

Following failure of the power supply to the pumps the pump torque immediately drops to zero. It is assumed that the SSC is designed with a fly wheel attached to the pump, the pump then coasts down at a rate determined by the inertia of the fly wheel, the inertia within the pump, and the inertia of the coolant. It is possible to lengthen the coast down time of the flow by designing with a large fly wheel. This increases the flow rate during the early stage. It can be determined from Figure 4-5 that the pump will continue to circulate the coolant for a substantial length of time. In an unprotected loss of flow event (beam on), the mass flow rate is promoted by a larger fraction of natural convection. Since natural convection is driven by density differences in the liquid it is linked to the power generation and to the temperature of the coolant. The flow in SSC undergoes a minimum just as the pump impeller comes to rest. As we shall see, this generates peak temperatures in the core. This phenomena is physical, it typically occur
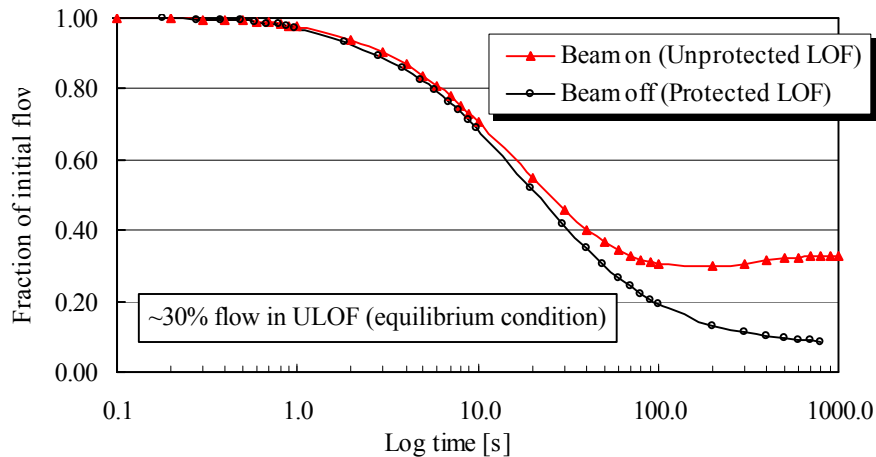
Figure 4-5. Primary coolant flow reduction following pump failure. Loss of electrical power to all pumps. Flow is reduced to natural circulation only.

in any loss of flow event. The flow rate have a tendency to dip before establishing a natural circulation flow that is in equilibrium with the heat generation. Equilibrium flow rate is reached within 100 seconds in the SSC. An equilibrium mass flow rate corresponding to 30% of the initial flow is achieved in the SSC. This flow is sustained by natural convection alone.

In the safety evaluation of the system, it must be ascertained whether natural convection on its own is adequate for heat removal. Otherwise, means must be incorporated to automatically shut down the beam before excessive core heat-up takes place.

Protected Loss of Flow event (beam off)

Following a beam shut-off the power will be generated by decay heat alone. Figure 4-6 displays the normalized total reactor power of the SSC subjected to a *protected loss of flow* event.
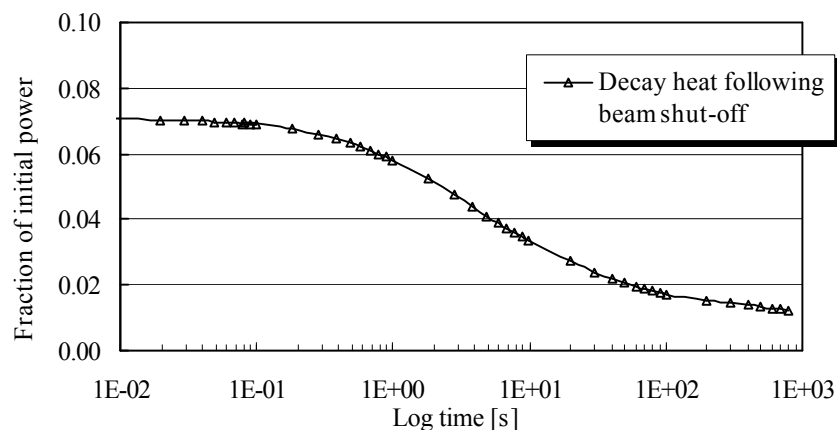

Figure 4-6. Total reactor power of SSC following beam shut-off.

The decay heat amounts to approximately 7% of full power immediately following the shutdown of the beam. After one hour the decay heat is produced at a rate of about 1% of full power. During the time period being analyzed (1000 seconds) the normalized

flow substantially exceeds the normalized power. The resulting, maximum, core temperatures are shown in Figure 4-7.
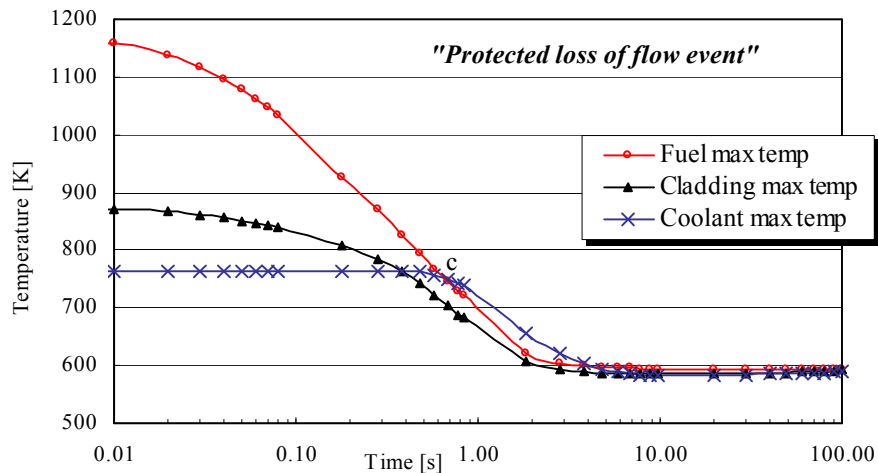

Figure 4-7. Maximum temperatures in fuel, cladding and coolant following Loss of Flow and simultaneous beam shut-off.

The favorable imbalance of normalized flow and power causes the overall temperature in the core to decrease. Redistribution of stored heat between fuel, cladding, and coolant causes the temperature of the fuel and cladding to drop immediately following beam shut-off. The redistribution of heat from the fuel to cladding and coolant tends to dominate the early stages of any protected flow failure accidents. The fuel temperature falls off at a rate determined by the characteristic time constant (calculated in earlier section to be 0.5 seconds) while the coolant requires the channel transit time (0.4 seconds) to elapse before any temperature changes occur. Power responds rapidly while the pump inertia retains a considerable flow during the early phase. During the initial second, the flow coast down has a negligible influence on the transient. The rapid temperature drop continues until an equilibrium is established between natural convection flow and decay heat generation. Subsequently, core temperatures are kept in balance as heat removal equalizes heat generation.

At a certain point in time the maximum temperature of the coolant is higher than the maximum temperature of the cladding and the fuel. The reason is because maximum temperatures occur at different axial locations. While maximum temperatures for the fuel and cladding are recorded close to core center, maximum temperatures for the coolant arise at core outlet. The coolant absorbs extra heat as it flows from core center to the outlet and it may temporarily obtain higher local temperatures than the cladding and fuel. In the equilibrium state, the production of decay heat results in the fuel temperature remaining slightly above that of the cladding and coolant.

From the above calculations it may be determined that the SSC responds in a benign way to a *protected loss of flow* event. Natural circulation flow effectively removes decay heat from the core.

Unprotected Loss of Flow event (beam on)

Typically the plant protection system is designed to automatically shut-off the beam in a pump failure event. Hence, it is only when the plant protection system (PPS) malfunctions that an *unprotected loss of flow* (ULOF) event may occur. The term "unprotected" refers to the situation when the accident event is not protected by the PPS. Given the hypothesis of complete failure of the pumps and complete failure of the plant protection system the dynamic response of SSC is investigated. Figure 4-8 contains the calculated thermal response of SSC in the case of an ULOF event.
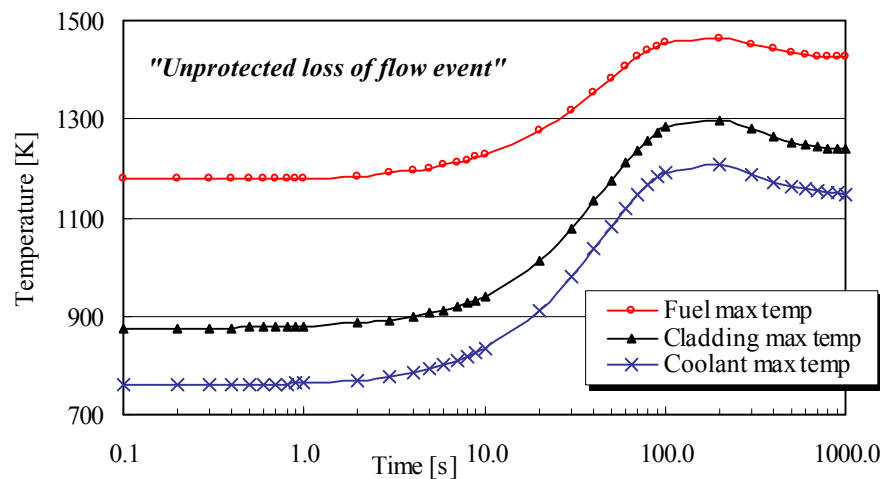
Figure 4-8. Maximum temperatures in fuel, cladding and coolant following Loss of Flow with beam on.

Since no reactivity feedbacks are present, power will remain at constant level throughout the transient. The reduction of flow reduces the heat removal and coolant temperatures increases. The temperature of the coolant increases first and is a primary indication of flow reduction. As the coolant heats up, less heat is transferred from the fuel. Temperatures in the fuel and cladding will gradually increase. The temperature increases at a rate determined by the flow coast down. When the pumps have come to a complete rest, mass flow rate is at a minimum. This enables core temperature to reach a critical point. As temperature peak, it will give the buoyancy driven flow an extra boost.

From Figure 4-8 it can be determined whether the reactor can remain at full power without causing immediate excessive temperatures or whether a rapid shutdown is required to prevent core damage. In this case, peak fuel temperatures are approximately 100 K below the fuel failure margin (set to 1570 K for the dissociation temperature of americium nitride).

4.4   SOURCE INSERTION ACCIDENT

In a *source insertion* accident the outcome of the transient is strongly dependent on the rate and magnitude of the source insertion. In this case, a worst case scenario is assumed in which a step increase of source intensity is simulated. Source power is promptly increased by a factor of two and the reactor power will double at almost the same

instant. Figure 4-9 displays the maximum fuel, cladding, coolant temperatures obtained for the SSC.
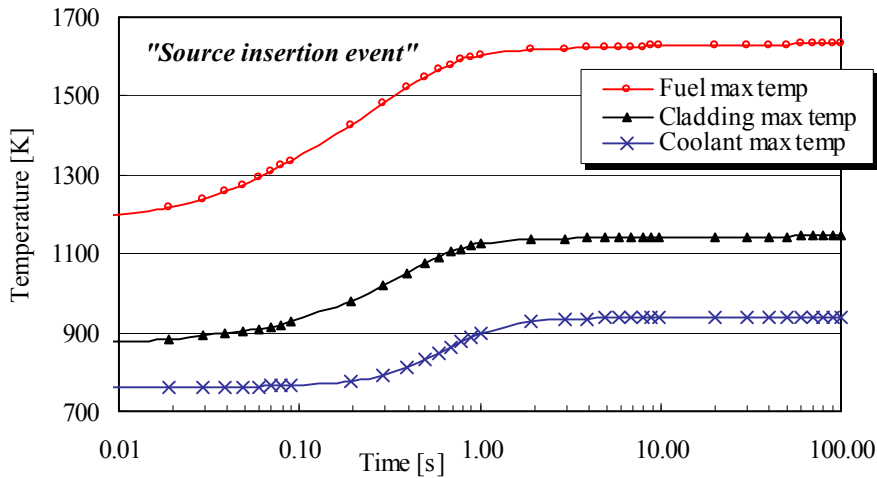

Figure 4-9. Maximum temperatures in fuel, cladding, and coolant following a source insertion transient.

The source disturbance is first noted as a rise in fuel temperatures and later by a rise in coolant temperatures. In any source disturbance the speed of the transient is characteristic. In a prompt increase of the source intensity, the reactor power reaches the asymptotic level before any temperature changes occur. It is seen that asymptotic thermal conditions are obtained within a few seconds. In fact, major parts of the transient are completed in the first second. Thus, early termination of source transients is desirable to diminish the negative consequences.

The calculation indicates that temperatures following a prompt doubling of the source power in the SSC may exceed the dissociation temperature of americium nitride fuel. It should also be taken into consideration that a constant coolant inlet temperature is assumed. Main concern in a source transient is that the power may increase to levels beyond the removal capabilities of the heat transport system. A more conservative approach would be to assume a constant coolant temperature drop in the steam generator. This would necessarily generate continuously increasing inlet temperatures for transients longer than the primary coolant loop time.

4.5   EXPLANATORY NOTE: SOME THEORETICAL GROUNDS FOR ADS DYNAMICS

4.5.1   Analytic solution of the point kinetics equations for a source-driven system

The point kinetics equations are arrived at when condensing the diffusion equation into a purely time-dependent one. The term "point kinetics" is used to indicate the space-and energy independence. To obtain a useful analytic expression the complexity of the point kinetics equations is reduced to one group of delayed neutrons. A weighted decay constant is used to represent all six delayed neutron groups. Moreover, since we seek

the solution to a step change in reactivity or source, any time-dependence of $\rho(t)$ and $s(t)$ is neglected. The following form of the point kinetics equations are considered.

$$\frac{dp}{dt} = \frac{r - b}{\Lambda} p(t) + \frac{1}{\Lambda} \overline{I} z(t) + \frac{1}{\Lambda} s \quad \textit{"one-delay-group point kinetics equations"} \qquad 4\text{-}7$$

$$\frac{dz}{dt} = -\overline{I} z(t) + bp(t) \qquad 4\text{-}8$$

$\overline{I}$ = weighted average decay constant for one group of delayed neutrons

s = relative independent source

$I_k z_k(t)$ = relative neutron source of delay group k

The notation used is the same as indicated by Karl O. Ott and Robert J. Neuhold, in the textbook "Introductory Reactor Dynamics". The total sources of delayed and independent neutrons in eqs 4-7 and 4-8 appear relative to the initial total source of fission neutrons according to

$$I_k z_k(t) = I_k \frac{\hat{C}_k(t)}{\hat{S}_{f0}} \quad \textit{"relative neutron source of delay group k"} \qquad 4\text{-}9$$

$\hat{C}_k = \hat{C}_k(t)$ = total precursor concentration in group k (integrated over space)

$\hat{S}_{f0}$ = total source of fission neutrons (integrated over spave)

where $z(t)$ is called the "reduced precursors" of delay group k.

$$s(t) = \frac{\hat{S}(t)}{\hat{S}_{f0}} \quad \textit{"relative independent source"} \qquad 4\text{-}10$$

$\hat{S} = \hat{S}(t)$ = total neutrons from independent source (integrated over space)

The system of equations 4-7 and 4-8, may be written as:

$$\dot{p}(t) - \frac{r - b}{\Lambda} p(t) - \frac{\overline{I}}{\Lambda} z(t) - \frac{1}{\Lambda} s = 0 \qquad 4\text{-}11$$

$$\dot{z}(t) + \overline{I} z(t) - bp(t) = 0 \qquad 4\text{-}12$$

The equations are solvable by the method of Laplace transform. Application of the Laplace transform method to the system of differential equations yields:

$$L\{\dot{p}(t)\} - \frac{r - b}{\Lambda} L\{p(t)\} - \frac{\overline{I}}{\Lambda} L\{z(t)\} - \frac{s}{\Lambda} L\{1\} = 0 \qquad 4\text{-}13$$

$$L\{\dot{z}(t)\} + \overline{I} L\{z(t)\} - bL\{p(t)\} = 0 \qquad 4\text{-}14$$

The initial values for $p(t)$ and $\zeta(t)$ are given by: $p(0)=p_0$ and $\zeta(0)=\beta p_0/\lambda$. Using the initial conditions and the Laplace translation theorems gives:

$$L\{p(t)\}= P(u)$$

$$L\{\dot{p}(t)\}= uP(u)- p(0)= uP(u)- p_0$$

$$L\{z(t)\}= Z(u)$$

$$L\{\dot{z}(t)\}= uZ(u)- z(o)= uZ(u)- \frac{bp_0}{\overline{I}}$$

$$L\{1\}= \frac{1}{u}$$

Where u is called the transform variable, which in this case is taken with respect to time. The Laplace expressions are substituted into eqs 4-13 and 4-14. The transformed equation becomes:

$$uP(u)- p_0 - \frac{r-b}{\Lambda}P(u)- \frac{\overline{I}}{\Lambda}Z(u)- \frac{s}{\Lambda u}=0 \quad \text{``transformed equation''} \qquad \text{4-15}$$

$$uZ(u)- \frac{bp_0}{l}+ \overline{I}Z(u)- bP(u)= 0 \qquad \text{4-16}$$

From transformation and simplification of eqs 4-15 and 4-16 we get:

$$P(u)\left(u^2 + u(\overline{I}-a_p)- \frac{r\overline{I}}{\Lambda}\right)= p_0 u + p_0 \frac{b}{\Lambda}+ p_0 \overline{I}+ \frac{s}{\Lambda}+ \frac{s\overline{I}}{\Lambda u} \qquad \text{4-17}$$

again we introduce the expression for the prompt inverse period:

$$a_p = \frac{r-b}{L} \quad \text{``prompt inverse period''} \qquad \text{4-18}$$

in order to factorize the second factor in the left hand side of eq. 4-17 we solve the second-degree equation:

$$u^2 + (\overline{I}-a_p)u - \frac{\overline{I}r}{\Lambda}= 0 \qquad \text{4-19}$$

and it has the following solution:

$$u_{1,2}= -\frac{\overline{I}-a_p}{2}\pm \sqrt{\left(\frac{\overline{I}-a_p}{2}\right)^2 + \frac{\overline{I}}{\Lambda}r} \quad \text{``solution to second degree equation''} \qquad \text{4-20}$$

If ρ is not close to β then the solution to eq. 4-19 can be approximated to

$$u_1 = -\frac{\overline{I}-a_p}{2}+ \sqrt{\left(\frac{\overline{I}-a_p}{2}\right)^2 + \frac{\overline{I}}{\Lambda}r}\approx \frac{lr}{\Lambda(\overline{I}-a_p)}\approx -\frac{\overline{I}r}{\Lambda a_p}= \frac{\overline{I}r}{b-r} \quad \text{``}1^{st}\text{ root''} \qquad \text{4-21}$$

$$u_2 = -\frac{\overline{I} - a_p}{2} - \sqrt{\left(\frac{\overline{I} - a_p}{2}\right)^2 + \frac{\overline{I}}{\Lambda}} \, r \approx a_p - \overline{I} \, \frac{b}{b - r} \approx a_p = \frac{r - b}{\Lambda} \quad \text{``2}^{nd} \text{ root''} \qquad 4\text{-}22$$

Use these roots to factorize eq. 4-17

$$P(u)(u - m_1)(u - m_2) = p_0 u + p_0 \frac{b}{\Lambda} + p_0 \overline{I} + \frac{s}{\Lambda} + \frac{s\overline{I}}{\Lambda u} \qquad 4\text{-}23$$

divide both sides of eq. 4-23 with $(u\text{-}m_1)(u\text{-}m_2)$ and apply the inverse Laplace transform:

$$L^{-1}\{P(u)\} = L^{-1}\left\{\frac{u}{(u - m_1)(u - m_2)}\right\} p_0 + L^{-1}\left\{\frac{1}{(u - m_1)(u - m_2)}\right\}\left(p_0 \frac{b}{\Lambda} + p_0 \overline{I} + \frac{s}{\Lambda}\right) +$$
$$+ L^{-1}\left\{\frac{1}{u(u - m_1)(u - m_2)}\right\} \frac{s\overline{I}}{\Lambda} \qquad 4\text{-}24$$

The inverse Laplace transform for each term can be evaluated with the help of the method of partial fractions:

$$L^{-1}\{P(u)\} = p(t) \quad \text{``inverse Laplace of 1}^{st} \text{ term''} \qquad 4\text{-}25$$

$$L^{-1}\left\{\frac{u}{(u - m_1)(u - m_2)}\right\} = \frac{m_1}{m_1 - m_2} e^{m_1 t} + \frac{m_2}{m_2 - m_1} e^{m_2 t} \quad \text{``inverse Laplace of 2}^{nd} \text{ term''} \quad 4\text{-}26$$

$$L^{-1}\left\{\frac{1}{(u - m_1)(u - m_2)}\right\} = \frac{1}{m_1 - m_2} e^{m_1 t} + \frac{1}{m_2 - m_1} e^{m_1 t} \quad \text{``inverse Laplace of 3}^{rd} \text{ term''} \quad 4\text{-}27$$

$$L^{-1}\left\{\frac{1}{u(u - m_1)(u - m_2)}\right\} = \frac{1}{m_1 m_2} + \frac{1}{m_1(m_1 - m_2)} e^{m_1 t} + \frac{1}{m_2(m_2 - m_1)} e^{m_2 t} \quad \text{``inverse Laplace}$$
$$\text{of 4}^{th} \text{ term''} \qquad 4\text{-}28$$

Substituting the inverse Laplace expressions into 4-24 and we obtain the *exact* solution

$$p(t) = -\frac{s}{r} + p_0\left[e^{m_1 t}\left(\frac{m_1}{m_1 - m_2} + \frac{b}{\Lambda(m_1 - m_2)} + \frac{\overline{I}}{m_1 - m_2} + \frac{s}{p_0 \Lambda(m_1 - m_2)} + \right.\right.$$
$$\left. \frac{s\overline{I}}{p_0 \Lambda m_1(m_1 - m_2)}\right) + \qquad 4\text{-}29$$
$$\left. e^{m_2 t}\left(\frac{m_2}{m_2 - m_1} + \frac{b}{\Lambda(m_2 - m_1)} + \frac{\overline{I}}{m_2 - m_1} + \frac{s}{p_0 \Lambda(m_2 - m_1)} + \frac{s\overline{I}}{p_0 \Lambda m_2(m_2 - m_1)}\right)\right]$$

where m_1 and m_2 are roots of a second-order equation given by eqs 4-21 and 4-22. The exact solution cannot be evaluated for $\rho=0$. Unfortunately, the exact expression is cumbersome and not very transparent. With the inclusion of the approximate expressions of the roots u_1 and u_2 and omission of small terms, 4-29 can be reduced to

$$p(t) = -\frac{s}{r} + \frac{s+r}{r-b}e^{\frac{r-b}{\Lambda}t} + \frac{b}{b-r}\left(\frac{s}{r}+1\right)e^{\frac{\bar{I}r}{b-r}t} \quad \text{``approximate solution''} \qquad 4\text{-}30$$

The above solution is approximate in that sense that small terms have been neglected. It is valid if ρ is not close to β (but ρ may be larger and smaller than β), for $\rho\neq0$ and $\lambda\Lambda<<\beta$. These requirements are well satisfied in an ADS. For example, the first requirement (ρ not close to β) would only be violated in a super-prompt critical excursion when the step reactivity insertion come close to $\Delta\rho=|\rho_0|+\beta$. The second requirement ($\lambda\Lambda<<\beta$) is satisfied under all conditions since the mean neutron generation time, Λ, in a fast spectrum is extremely short.

4.5.2 Derivation of fuel time constant

General solution of the temperature distribution in a cylindrical solid

The general solution for the temperature distribution in a cylindrical shell as well as in a solid cylinder is given by

$$T(r) = \frac{-q_V}{4\cdot\lambda_{fuel}}r^2 + C_1\cdot\ln(r) + C_2 \quad q_V\text{=volumetric heat generation }[W/m^3] \qquad 4\text{-}31$$

The above general solution may be used to obtain the temperature distribution for a variety of boundary conditions, for example,

Temperature distribution in a hollow fuel pin with uniform internal heat generation

Two boundary conditions are needed to evaluate C_1 and C_2. The first boundary condtion would be

$$T(r_2) = T_2 \quad \text{"1st boundary condition"}$$

If we assume that the inner surface of the cylinder is *perfectly insulated*, or adiabatic, then the second boundary condition would be

$$\frac{dT}{dr}=0 \quad \text{for } r=r_1 \quad \text{"2nd boundary condition"}$$

Applying the 1st boundary condition to the general solution, eq. 4-31, gives

$$T_2 = \frac{-q_V}{4\cdot\lambda_{fuel}}r_2^2 + C_1\cdot\ln(r_2) + C_2 \qquad 4\text{-}32$$

The derivative of the general solution with respect to r is

$$\frac{dT}{dr} = \frac{-q_V}{\lambda_{fuel}} \cdot r + \frac{C_1}{r}$$

<div align="right">4-33</div>

Similarly, applying the 2nd boundary condition to eq. 4-32 gives

$$0 = \frac{-q_V}{2 \cdot \lambda_{fuel}} \cdot r_1 + \frac{C_1}{r_1} \qquad \text{and} \qquad C_1 = q_V \cdot \frac{r_1^2}{2 \cdot \lambda_{fuel}}$$

<div align="center">inserting into, eq. 4-32 gives</div>

$$C_2 = T_2 + \frac{q_V}{4 \cdot \lambda_{fuel}} r_2^2 - \frac{q_V}{2 \cdot \lambda_{fuel}} \cdot r_1^2 \cdot \ln(r_2)$$

Substituting into the general solution, eq. 4-31, it follows that

$$T(r) = T_2 + \frac{q_V}{4 \cdot \lambda_{fuel}} \cdot \left(r_2^2 - r^2\right) - \frac{q_V}{2 \cdot \lambda_{fuel}} \cdot r_1^2 \cdot \ln\left(\frac{r_2}{r}\right)$$

<div align="right">4-34</div>

Derivation of average temperature

In the lumped heat capacity method the average temperature is used to characterize the temperature of the body. The average temperature, T_{av}, in a cylindrical shell is obtained from

$$T_{av} = \frac{\int_{r_1}^{r_2} T(r) \cdot 2\pi r \, dr}{\int_{r_1}^{r_2} 2\pi \cdot r \, dr}$$

<div align="right">4-35</div>

Inserting the previously derived expression of T(r), eq. 4-34, into eq. 4-35 we get

$$T_{av} = T_2 + \frac{\int_{r_1}^{r_2} \frac{q_V}{4\lambda_{fuel}}\left(r_2^2 - r^2\right)r - \frac{q_V}{2\lambda_{fuel}}r_1^2 \cdot \ln\left(\frac{r_2}{r}\right) \cdot r \, dr}{\int_{r_1}^{r_2} r \, dr}$$

which simplifies into

$$T_{av} = T_2 + \frac{\left[\dfrac{-1}{8} \cdot q_V \cdot r_2^2 \cdot \dfrac{\left(-r_2^2 + 2 \cdot r_1^2\right)}{\lambda_{fuel}} - \dfrac{1}{8} \cdot q_V \cdot r_1^2 \cdot \dfrac{\left(-3 \cdot r_1^2 + 2 \cdot r_2^2 - 4 \cdot r_1^2 \cdot \ln(r_2) + 4 \cdot r_1^2 \cdot \ln(r_1)\right)}{\lambda_{fuel}}\right]}{\left(r_2^2 - r_1^2\right)}$$

or rather,

$$T_{av} = T_2 + \frac{\left[\dfrac{-1}{8} \cdot q_V \cdot r_2^2 \cdot \dfrac{\left(-r_2^2 + 2 \cdot r_1^2\right)}{\lambda_{fuel}} - \dfrac{1}{8} \cdot q_V \cdot r_1^2 \cdot \dfrac{\left(-3 \cdot r_1^2 + 2 \cdot r_2^2 + 4 \cdot r_1^2 \cdot \ln\left(\dfrac{r_1}{r_2}\right)\right)}{\lambda_{fuel}}\right]}{\left(r_2^2 - r_1^2\right)}$$

as a parentheses, if the hollow cylinder would assume the shape of a solid cylinder, $r_1 = 0$, the above expression for T_{av} becomes

$$T_{av} = T_2 + \frac{q_V \cdot r_2^2}{8\lambda_{fuel}}$$

Derivation of thermal resistance
The basic equation for linear thermal resistance is

$$R_{th} = \frac{\left(T_{av} - T_2\right)}{q_l}$$

q_l = linear heat generation rate [W/m]

R_{th} = linear thermal resistance [K/W/m]

replacing linear heat rate with volumetric heat generation rate in a hollow fuel pin gives

$$R_{fuel} = \frac{\left(T_{av} - T_2\right)}{q_V \cdot \pi \cdot \left(r_2^2 - r_1^2\right)}$$

q_V = uniform volumetric heat generation within the fuel pin [W/m^3]

inserting the derived expression for T(r) for T_{av}, gives

$$R_{fuel} = \frac{r_1^2 \cdot \left(3 \cdot r_1^2 - 2 \cdot r_2^2 - 4 \cdot r_1^2 \cdot \ln\left(\dfrac{r_1}{r_2}\right)\right) + r_2^2 \cdot \left(r_2^2 - 2 \cdot r_1^2\right)}{8 \cdot \pi \cdot \lambda_{fuel} \cdot \left(r_2^2 - r_1^2\right)^2}$$

further simplification results in

$$R_{fuel} = \frac{3 \cdot r_1^4 - 4 \cdot r_1^2 \cdot r_2^2 + r_2^4 - 4 \cdot r_1^4 \cdot \ln\left(\dfrac{r_1}{r_2}\right)}{8\pi\lambda_{fuel} \cdot \left(r_2^2 - r_1^2\right)^2} \qquad 4\text{-}36$$

Linear thermal resistance of the bonding [K/W/m]

$$R_{bond} = \frac{\ln\left(\dfrac{r_3}{r_2}\right)}{2 \cdot \pi \cdot \lambda_{bond}} \qquad 4\text{-}37$$

Linear thermal resistance of the cladding [K/W/m]

$$R_{clad} = \frac{\ln\left(\dfrac{r_4}{r_3}\right)}{2 \cdot \pi \cdot \lambda_{clad}} \qquad 4\text{-}38$$

Linear convective resistence [K/W/m]

$$R_{conv} = \frac{1}{h \cdot 2 \cdot \pi \cdot r_4} \qquad 4\text{-}39$$

Convective heat-transfer coefficient is calculated from the Lyon-Martinelli correlation

$$Nu = 4.8 + 0.0025 \cdot (RePr)^{0.8}$$

Combining eqs. 4-36 to 4-39 we may calculate the overall heat-transfer coefficient [W/K per unit length]

$$U = \frac{1}{R_{fuel} + R_{bond} + R_{clad} + R_{conv}} \qquad 4\text{-}40$$

Derivation of heat capacities

$$C_{fuel} = \left(r_2^2 - r_1^2\right)(1 - porosity)\,\pi \cdot \rho_{fuel} \cdot c_{pfuel}$$

$$C_{bond} = \left(r_3^2 - r_2^2\right)\pi \cdot \rho_{bond} \cdot c_{pbond}$$

$$C_{clad} = \left(r_4^2 - r_3^2\right)\pi \cdot \rho_{clad} \cdot c_{pclad}$$

$$C_{tot} = C_{fuel} + C_{bond} + C_{clad} \qquad\qquad 4\text{-}41$$

Characteristic time constant of the fuel pin [s]

Eqs 4-40 and 4-41 give the time constant of the fuel pin

$$\tau = \frac{C_{tot}}{U}$$

Table 4-6. Design data used

Fuel pin design	ID fuel	OD fuel	ID cladding	OD cladding	v [m/s]	P/D	n_{pins}	D_h [mm]	p
			[mm]						
All pins	2.00	4.80	4.98	5.88	2.0 or 2.5	1.75	91	10.63	0.15

Table 4-7. Physical constants used

Fuel pin design, bonding	Fuel density [kg/m³]	Fuel specific heat [J/kgK]	Fuel thermal conductivity [W/mK]	Bonding density [kg/m³]	Bonding specific heat [J/kgK]	Bonding thermal conductivity [W/mK]
Pb/Bi v=2.5 m/s	13778	212	11.313	9965	147	16.038
Pb/Bi v=2.0 m/s	13778	212	11.313	9965	147	16.038
Na v=2.5 m/s	13778	212	11.313	804.785	1252.178	58.341
He v=2.5 m/s	13778	212	11.313	1.5960	5200.000	0.3150
N₂ v=2.5 m/s	13778	212	11.313	11.2560	1143	0.062

Table 4-8. Physical constants used

Fuel pin design, bonding	Cladding density [kg/m³]	Cladding specific heat [J/kgK]	Cladding thermal conductivity [W/mK]	Coolant density [kg/m³]	Coolant specific heat [J/kgK]	Coolant thermal conductivity [W/mK]
Pb/Bi v=2.5 m/s	7722	569.2	21.816	10209	147	13.992
Pb/Bi v=2.0 m/s	7722	569.2	21.816	10209	147	13.992
Na v=2.5 m/s	7722	569.2	21.816	10209	147	13.992
He v=2.5 m/s	7722	569.2	21.816	10209	147	13.992
N_2 v=2.5 m/s	7722	569.2	21.816	10209	147	13.992

5 THERMAL HYDRAULICS STUDIES OF SOME ADS CHARACTERISTICS

5.1 EMERGENCY DECAY HEAT REMOVAL BY REACTOR VESSEL AUXILIARY COOLING SYSTEM

In accident situations where the normal cooling systems are lost, the decay heat generated must be removed to avoid damages on structural materials. Reactor Vessel Auxiliary Cooling Systems (RVACS) are totally passive and rely, in its most simple form, only on natural air circulation around the reactor vessel [21]. Emergency decay heat removal by RVACS is required in a Loss-of-Heat Sink (LOHS) accident in which the normal heat removal means are not operational e.g. due to a station blackout. The latter would mean that also the accelerator and the primary pumps are switched off (i.e. additionally a Loss-of-Flow – LOF - condition). It is also conceivable that the primary and secondary pumps loose their power supply and that the accelerator is not switched off. The RVACS is a totally passive system i.e. neither human operations nor mechanical devices are necessary to initiate them. Only physical laws (like heat convection and gravitations) govern an RVACS, which makes it extremely unlikely that it fails to operate. The physical foundation for the RVACS is the temperature difference, and consequently the density difference between the air in the downcomer relative to the riser of the RVACS. Due to the heat-up during the LOHS accident a static pressure difference develops, which sets the air in motion and leads to heat removal

The licentiate thesis investigations were performed – see Appendix IV - on the decay heat removal during a combined Loss-of-Flow (LOF) and Loss-of-Heat-Sink (LOHS) accident for two different reactor sizes, 80MWth and 480MWth. The reactor design was based on the proposal of an ADS demonstration plant from the Italian engineering firm Ansaldo [22].

It was shown that for an 80MWth reactor, in which the proton beam is shut off immediately after LOHS accident initiation, the decay heat is easily removed by air-cooling alone. In the unlikely case that the proton beam is left on for 30min, severe structural damage can also be prevented. For the 480MWth reactor with an RVACS with air-cooling, the temperature of the core outlet exceeds 1041K where structural problems commence. However, if the gap between the reactor and the guard vessel is filled with Pb/Bi and water is sprayed on the guard vessel outside concurrently, the vessel temperature easily stays below acceptable limits. With these extra cooling measures a 5min delay of the beam-stop can be afforded before severe structural problems commence.

5.2 TEMPERATURE AND VELOCITY PROFILES IN A STEAM GENERATOR ON THE PRIMARY SIDE

Temperature and velocity profiles of steam flowing on the primary side in a steam generator were investigated. These profiles will later be used for modelling particle deposition on the wall surfaces. The deposition velocity in the boundary layers is dependent on the temperature gradient according to eq. 5-1. The motion of particles due to temperature gradients is known as thermophoresis.

$$U_T = -\frac{2C_s \mathbf{n}\left(\frac{k_g}{k_p} + C_t \frac{\mathbf{l}}{R}\right)\left(\frac{(\nabla T)_x}{T_0}\right)}{\left(1 + 2C_m \frac{\mathbf{l}}{R}\right)\left(1 + 2\frac{k_g}{k_p} + 2C_t \frac{\mathbf{l}}{R}\right)} \qquad 5\text{-}1$$

where k_g and k_p the thermal conductivities of the gas and the particle, C_s, C_t, C_m, are numerical factors, $\mathbf{n}$ the kinematic viscosity, $\mathbf{l}$ the mean free path, R the particle radius, $\tilde{N}T$ the temperature gradient, T_0 the mean gas temperature in the vicinity of the particle.

Figures 5-1 and 5-2 depict the temperature and velocity profiles on the primary side at the inlet bend of a steam generator. After the bend the pipe diameter narrows from 3 to 2 centimetres. The temperature at inlet is about 700°C, after the point where the pipe become narrower the coolant medium on the secondary side is 150°C.
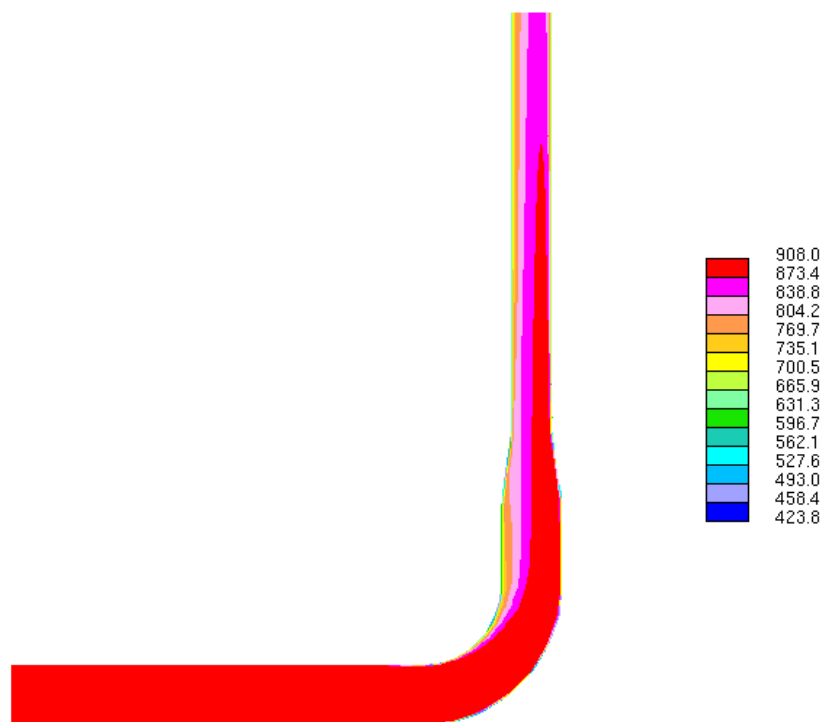

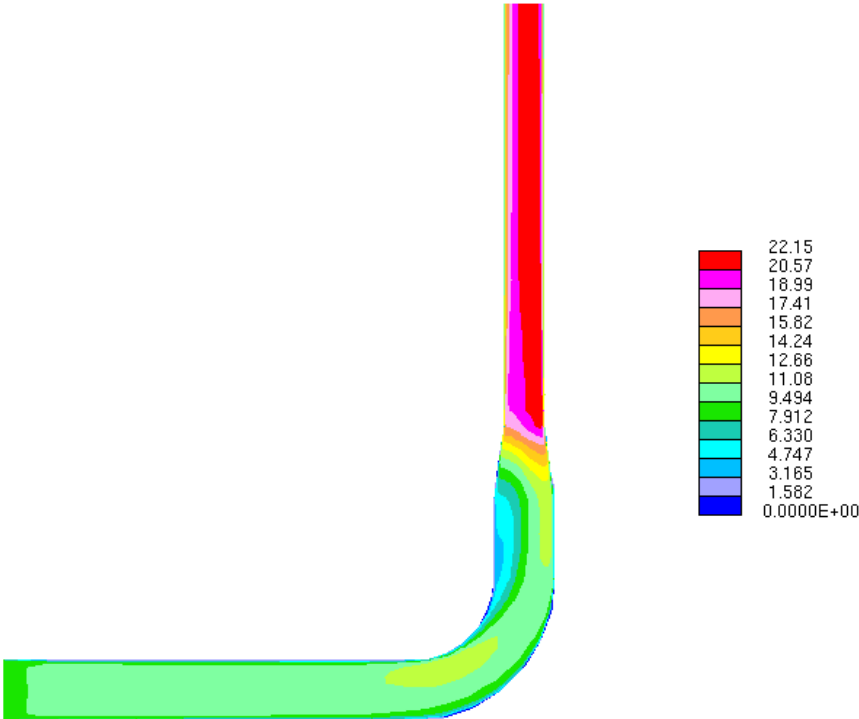*Figure 5-2. Temperature profile at the inlet bend in the primary side of a steam generator.*

Figure 5-3. Velocity profile at the inlet bend on the primary side of a steam generator. The scale is in metres per second.

6   CODE DEVELOPMENT

6.1   MONTE-CARLO BURNUP CODE - MCB

Applications of Monte Carlo methods in radiation transport calculations using continuous-energy data have been growing along with a progress of computational power of computers. However, Monte-Carlo based burnup calculations with reasonable statistics are very lengthy and an average computational time required for these calculations is much larger (even by three order of magnitudes) than for stationary radiation transport calculations. So, effective Monte-Carlo burnup methods require dedicated numerical tools to perform a fast analysis of nuclide transitions in a transmutation phase space.

MCB-code developed at KTH is a Monte Carlo Continuous Energy Burnup Code for a general-purpose use in calculations of nuclide density evolution with time during burnup or decay processes. The code integrates well-known code MCNP [26] widely used for neutron transport calculation, and a novel Transmutation Trajectory Analysis code (TTA) [27]. The code performs density evolution calculations, including formation and analysis of the transmutation chain. The component codes were integrated on the level of the source code of MCNP by preparation of the patch file to the source file of MCNP for preprocessor code that produces a new source file of MCB. Thus MCB keeps all the structure of MCNP and is compatible with it. Initially the version 4B of MCNP code was used and beta version - MCB-0.95 was released for extensive test and applications what included benchmark calculations and reactor core designing. The verification of the code in practice is the best way of its validation. The general conclusion from practical application was that MCB produces valuable results that are physically inherent proving correctness of physical model applied. The outcome of tests showed us also week points of the calculation system concerning two issues. The first one was occurrence of errors in some cross sections, and second was the data allocations system in computer memory of MCNP in cases of system modeling characterized by large number of nuclides and respective cross sections. The second problem was present in the MCNP code since very beginning but showed up only in massive cases that are present in transmutation systems. For dealing with those problems, ad hoc measures were applied. In the meantime, it happened that the same problem troubled the MCNP team what resulted in improvement of the code of version 4C [28]. This was another task for us to upgrade the MCB to the MCNP-4B. The problem was not trivial since the data structure of MCNP was changed significantly and some subroutines were actually rewritten. Since existing problems were alleviated in new version of MCNP, they also disappeared in new version of MCB: MCB1C.

The MCB1C was also equipped with new features among them the main is simulation of material processing. Development of the code was addressed towards improving calculation effectiveness and system diagnostic and towards improving physical model for rigid treatment but also providing simplified model option for quick design studies or benchmarks.

6.1.1   Features of MCB1C

MCB is fully compatible with MCNP-4C and it can work in the pure MCNP mode while keeping newly introduced options of material definitions that can simplify the preparation of input file. MCB can be interrupted and restarted the same way as MCNP and the backup RUNTPE file also can be used for a new restart in case of system malfunction during the run. An enhancement of the case name option was recently introduced. It allows the user to use the same case name for continue run, while the code varies the last letter of the file specific name. MCB creates larger amount of files than MCNP does therefore the structure of file name produced by the code is modified. It consists from the case name, if used, combined with the specific file name. This option gives the user better recognition of created files especially in cases of restarting of calculations.

The MCB code can run on standard UNIX platforms as well as on LINUX computers. In both cases, the PVM – Parallel Virtual Machine [29] - option of parallel execution is available. However, PVM option was heavily modified in MCNP4C thus this feature need to be tested in MCB1C. The pointer option (dynamic allocation of memory) is available also. The dynamic allocation of memory and PVM options can be applied at one time on UNIX systems when standard FORTRAN77 compiler is used. The FORTRAN compilers available on Intel LINUX like GNU does not support dynamic allocation of memory while the ABSOFT compiler creates problems with the PVM option. Introduction of both options simultaneously requires new compiler or problem to be solved a way around.

The decay schemes of all possible nuclides and their isomeric states are formed and analyzed basing on decay data taken from two sources. The first one – TOI.LIB has been prepared based on "Table of Isotopes" and describes decay schemes for over 2400 nuclides [30]. The second one - XS.LIB is a decay data file used for ORIGEN code system [31] and it supports energy-integrated ratios of nuclide formation in excited states. For the purpose of the output file clarity the nuclides are divided into for groups depending on their decay half-life and the discrimination value set by the user. The fast decaying nuclides are treated in a simplified manner, nevertheless the calculated system activity or decay heat depositions accounts for their appearance in the system. The vast number of nuclides can be handled easier way due to introduced possible material specification with the chemical symbols.

The code can be used for simulation of subcritical systems with fixed external source of neutrons and for critical systems for which the eigen-flux is used for normalization. Pure decay mode is also available. The neutron flux distribution can be normalized by specified external neutron source strength or the system thermal power. It can be set in user defined periods independently where periods of irradiation can be mixed with cooling periods. The recent version allows the user for simulation of material processing that includes removal or admixture of the nuclides as well as the shifting of materials from cell to cell and continuous supply of material to the system. This option can be used for consideration of complex refueling scenarios that includes liquid fuel flow to the burnable regions. The user can define time batch points or batch periods for desired processing what simplifies the calculation system definition. The simulation of material processing can be done by one of few options like addmixing or removing certain amount of material, leveling the density of material to required level, or by replacing material (i.e. burnt fuel) with the fresh one. Since the processing can be done also in

continuous way it allows the user for taking into account the nuclides generated in high energy particles interactions, which can be simulated by the LAHET [32] or MCNPX [33] code, in the transmutation process simulation of MCB.

Numerous cross-section libraries and data sets can be loaded into computer memory for to adequately calculate reaction rates and nuclide formation probabilities. Simulation of transmutation system requires material handling of a large number, what, from the user point of view, raises necessity of improving (simplifying) material and associated nuclear data specification. Yet, consideration of different physical conditions as a variable of geometry position requires introduction of material differentiation and possibility to assign different nuclear data libraries to different cells for the same nuclide. All those features are introduced in MCB. The code allows the user much simpler material definition, comparing to MCNP, using material mixing option and definition of materials with chemical symbols. It includes possibility of separate treatment of cross section for different burnable zones, to account for thermal effects, employment of energy dependent distribution of fission product formation, and energy dependent formation of isomer nuclides.

Reaction rates are calculated exclusively by continuous energy method with the usage of the point-wise transport cross-section libraries and, in case of lack of proper library, by using dosimetry cross section library. The contributions to reaction rates are being scored at every instant of neutron collision occurring in cells filled with burnable material by using the track length estimator of neutron flux. The user specifies the libraries explicitly or by using the default library option scheme similar to the one used in MCNP (NLIB entry on M card). It allows the user to assign different library to different cells for the same nuclide in order to account for thermal effects on cross sections. The reaction rates calculations consumes the most of computer time thus optimization of this process can shortened calculations. We have solved this problem in latter versions of MCB by introduction of so-called emerging nuclide run. In this run, which is performed at beginning of calculations the reaction rates are not calculated during neutron transport simulation but after obtained neutron flux. Next, the evolution of material density over burnup period creates the list of emerging nuclides. In actual runs the reaction rate calculations by continues energy method is provided only for meaningful nuclides. The emerging nuclide list is updated with every step of density evolution calculations. Diagnostic of nuclide status and required transport and reaction cross sections is being printout then.

Formation of excited state nuclides due to process of neutron capture or (n,2n) reaction is calculated from energy dependent isomer formation ratios supported by file ISB.LIB or, in case of their lack, by using the integral isomer formation ratios taken from the ORIGEN library - XS.LIB file. The current version of ISB.LIB file is limited to two nuclides and was prepared on rater old experimental data in limited range of energy. In the future, this file needs to be updated with data based on recent evaluations and experiments.

Fission product yield is calculated from incident energy dependent distributions of fission products prepared separately for every fissionable nuclide, which are loaded from the FY.LIB file. The progress due to extensive research in this field will impose an update replacement of this file also. The density of fission product emerging in burnup evolves with time of burnup the same way, as materials from initial composition. They take part in the neutron transport process as well as in transmutation process. Since

large number of possible nuclides creating fission products, the rigid treatment requires extensive number of material considerations what must be calculation time consuming. However, in some cases of interest i.e. for benchmarks or for design studies a simplified form of treatment by using of lump fission product can be required. To meet this we have equipped MCB1C with options of total negligence of fission product considerations or simplified treatment with usage of lump fission product.

Heating is calculated automatically, similar way as the reaction rates, during neutron transport simulation by using heating cross sections that are KERMA factors contained in standard cross section tables. In the initial version of MCB the heating calculations was limited to values deposited by neutrons or released in fission. This limitation diminished after code development. In current version of calculation system, all important effects affecting heating rate are considered. That includes gamma heating, decay heat of short-lived nuclides, particularly fission products, and decay heat of long-lived isotopes, which are responsible for decay-heat. In order to account for gamma heating the heating data in cross section libraries should be processed with included option for local deposition of gamma heating being added to neutron heating. In that way, the gamma heating from gamma radiation induced by neutron capture or scattering is already included at the level of neutron cross section library. The cross section libraries processed for MCB have this option switched on. In case of using cross sections without heating data, or if needed, the user can use an option to calculate heating from recoverable energy of fission which data is by default loaded with transport cross sections. The code calculates the heating from natural decay of nuclides using the energy of decay taken from the ORIGEN library.

Time evolution of nuclide densities is calculated with the complete set of linear transmutation chains that is prepared for every zone and time step so it is being automatically adjusted to time evolving transmutation conditions. The code uses extended linear chain method, based on the Bateman approach, to solve, prepared-on-line, set of linear chains. By using emerging nuclide list the set is constructed only from meaningful linear chains, noticeably contributing to density of formed nuclides. The program calculates transmutation transitions from nuclide to nuclide and prints them out to one of the output file. Transmutation chains that are formed by the code can be also printed for nuclides of interest.

Toxicity of material is calculated as the dose potentially taken by human population in case of ingestion on the basis of committed dose per intake tables, according to regulation by EURATOM Directive [34]. According to obtained results, the program lists the most dangerous nuclides along with their toxicity.

The code development in area of providing system characteristics led to implementing several functions that describe the subcritical system. The program calculates neutron multiplication and neutron multiplication factors both in the external fixed source mode of calculations as well as in criticality calculations with the fission source. Obtained values are then used to calculate the neutron source importance defined in two ways. The first one is the importance for generating the fission reactions that means for fission heating generation. The second is the importance for neutron multiplication that includes non-fission multiplicative reactions. Time evolutions of those parameters are printed out together with neutron source strength, energy deposition per source neutron, potential dose and material activity.

Self-adjusting step routine becomes active when the user defines allowed variation of k_{eff} or the heating rate. The code controls the calculation mode, by setting the external source mode or the fission source mode (k-code), upon the current value of k_{eff} reaches the value specified with VKSW parameter. The calculation mode can be fixed by the user. The options of using the neutron source, defined by SDEF, SSR, SRCTP or the SOURCE subroutine, are possible.

We are planning to implement additional processing of results in calculations producing large number of data. For this purpose a binary file - BHIST - can be created containing all information produced during neutron transport and burnup simulation. BHSIT file will be used by auxiliary program, yet to develop, to produce concise particular graphs or tables.

6.1.2   Options of Transmutation System Definition.

The MCB code can work as a standard MCNP unless burnup option is switched on. The card BURN that contains the list of burnable material does the switch. Without this card, all transmutation options are ignored. Required specifications of transmutation system are briefly described as follows.

- burnable material,
- libraries required for reaction rates calculations,
- control parameters and source specifications for required modes of calculations
- duration of transmutation time periods,
- system normalization with external neutron source strength or thermal power,
- material processing,

In addition to above the user can specify values of control parameters which otherwise would take the default values.

Material and Library Definition.

Following three categories of material are defined:
- *Transport material* - Specified by M card, used in all processes.
- *Burnup material* - Specified by MB card, not used in neutron collision simulation.
- *Residual material* - Specified by MR card, used only for transmutation transition calculations for specific purposes.

Control Parameters.

The Table 6-1 shows available control parameters with their default values and the control card to specify in.

Table 6-1. Control parameters of MCB-code and their default values.

Parameter	Default value	Card	Short description
THFM	10^6 [s]	BATCT	Decay half life threshold for fast decay treatment
CMIN	10^{-10}	BATCT	Discrimination level of nuclide-to-nuclide transmutation transition
VKSW	1.0	BATCT	Value of k-eff above which k-code is used to calculate reaction rates
VKLIM	2.0	BATCT	Value of k-eff that terminates the calculations
FHEAT	OFF	BATCT	Switch to calculate heating only from fission
BURHT	OFF	BATCT	Switch to calculate heating only in burnable zones
TRNDCR	10^{-6}	DISCR	Discrimination level of total cross section contribution used for nuclide selection to the transport calculations
CPRCUT	10^{-6}	DISCR	Discrimination level for nuclide density printout
DPRCUT	10^{-3}	DISCR	Discrimination level for dose printout
VART	1.0 [year]	STPCT	Longest allowed time step
VARK	0.0 (OFF)	STPCT	If greater than zero - allowed variation of k-eff during one time step
VARH	0.0 (OFF)	STPCT	If greater than zero - allowed variation of energy deposition per source neutron during one time step

Mode of Calculations

Burnup calculations can be done either in k-code mode or in transport mode. The system switches between two modes depending on current value of k-eff. In both cases if user whishes to control level of k-eff the k-code mode must be used for this purpose. To invoke k-code calculation the user must use the KCODE card. System normalization is done by POWER card with the limits of system thermal power or by SRCST card with the limits of external source strength.

Possible options:

- Pure decay calculations. No normalization required.
- Only external fixed source mode defined by SDEF, RSSA or SOURCE subroutine. It can be accomplished if system remains subcritical with burnup. Both power or source strength normalization possible.
- Pure k-code mode (with fission source defined by SDEF or SRCTP. Normalization to the thermal power is necessary.
- Mixed cases where both k-code mode and fixed source mode are applied according to specified control parameters and calculated system characteristic.

Period Specification

The user specifies periods of constant physical conditions by using PRIOD card. Duration of periods are limits of time steps so in cases when physical condition. The user can fix time steps or use time step self-adjusting procedure.

Material processing

The material processing is invoked by time specification cards and processing specification cards. Two kinds of processing are allowed: the time point processing, for which the sequence of time points should be specified, and continuous processing, for which the time periods need to be specified. They can be grouped together to form processing batches to be performed in specified time points or time periods. The batches can be formed from the same kind of cards concerning continuous or point type of processing.

The time specification cards are:

    i)   AT – time point specification card for material processing

    ii)   AFTER – the time period numbers for time point material processing

    iii)   FROM – TO - time sub-period specification card for continuous processing

    iv)   DURING – the time period numbers for continuous material processing.

Processing specification can be done by cards:

    i)   RMOVE - remove nuclides from material

    ii)   LIMIT – adjust nuclide density in material according to given limits

    iii)   ADMIX – admix new portion of nuclides to the material

    iv)   SHUFL – shuffle materials.

Figure 6-1 shows a flow-diagram of the MCB code.

Extensive benchmarking of the MCB code have been presented in NEA/OECD [35] and IAEA [36] reports which are to be published in the final forms in 2001.
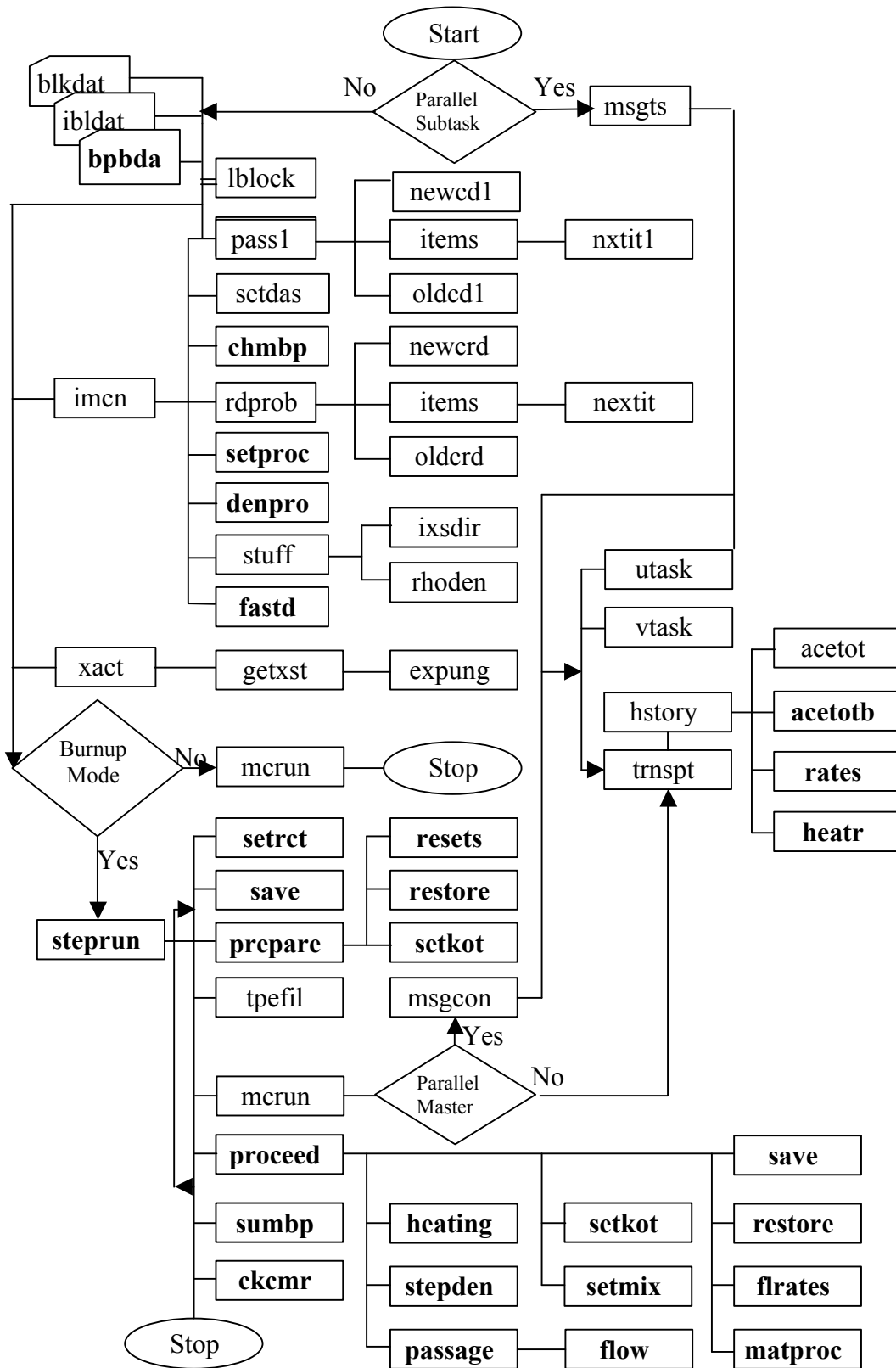
Figure 6-1. Flow diagram of the MCB-code

6.2 BENCHMARKING AND DEVELOPING A NUCLEAR DATA PROCESSING CODE - NJOY

The NJOY [37] Nuclear Data Processing System is a modular computer code used for converting evaluated nuclear data in the ENDF format into libraries useful for applications calculations. Because the Evaluated Nuclear Data File (ENDF) format is used all around the world (e.g., ENDF/B-6 in the US, JEF-2.2 in Europe, JENDL-3.2 in Japan, BROND-2.2 in Russia), NJOY gives its users access to a wide variety of the most up-to-date nuclear data. NJOY provides comprehensive capabilities for processing evaluated data, and it can serve applications ranging from continuous-energy Monte Carlo (MCNP), through deterministic transport codes (DANT, ANISN, DORT), to reactor lattice codes (WIMS, EPRI). The modular nature of NJOY makes it easier to add output for other kinds of application libraries or to add new computational features. NJOY handles a wide variety of nuclear effects, including resonances, Doppler broadening, heating (KERMA), radiation damage, thermal scattering, gas production, neutrons and charged particles, photoatomic interactions, photonuclear reactions, self shielding, probability tables, photon production, and high-energy interactions (to 150 MeV). Output can include printed listings, special library files for applications, and graphics.

NJOY has been under continuous development in many years. KTH has established few years ago a close collaboration with T2 Division at Los Alamos National Laboratory aimed at benchmarking and debugging of the NJOY code in order to establish a reliable computer code for nuclear data processing. Los Alamos National Laboratory, in particular Dr. R. MacFarlane, carries main responsibility for NJOY development and coordinates international tasks on debugging and developing this code [38].

KTH has contributed to the code development through extensive tests on data processing from the following nuclear data libraries:

- Evaluated Nuclear Data File - ENDF/B-6 versions 4, 5 and 6
- Joint European File – JEF-2.2
- Japanese Evaluated Nuclear Data Library –JENDL-3.3
- Evaluated Activation File – EAF-3.1

A number of errors has been discovered both in NJOY source code and in the nuclear libraries themselves. The most important improvements are:

- *For NJOY-code:*
  - removing many compiler-dependent errors and incompatibilities
  - correcting errors destroying the calculation of s(alpha,beta) for some isotopes
  - correcting errors affecting delayed neutron spectra
  - improving acer (acer routine prepares data for Monte Carlo data libraries) consistency checks
  - introducing options enabling processing of some isotopes: natural Pb, natural Si, ^{9}Be, ^{52}Cr, ^{56}Fe, ^{90}Zr from JEF-library , Cd, ^{235}U from JENDL, Si from ENDFB

- removing bugs in H, ^{4}He ^{9}Be, ^{209}Pb processing
- removing errors in modeling of charged-particle emission, which occurs in a number of important materials from release 6 of ENDF/B6
- improving gamma heating and material damage calculations for the JEF data library
- removing errors in processing angular distributions for processing data above 20 MeV, so called 150-MeV evalutions (of special importance for ADS simulations!)
- Correcting size of matrices in order to enable processing of U and Pu data up to 150 MeV.

- *For JEF-2.2 library*:
  - resolving negative energy problems for natural Pb evaluation (non standard evaluation for this element)
  - removing errors for ^{233}U evaluation. The errors have been fixed temporarily for "beta-users", a NEA/OECD Nuclear Data Committee has to make some decisions concerning standarization of some data formats

- *For JENDL-3.2:*
  - Correcting evaluation errors for ^{14}N, ^{12}C

- *For ENDF/B-6*
  - Correcting evaluation errors for ^{208}Pb (n,alpha reaction error) and for ^{14}N

The last version of NJOY99.50 [38] is a very stable and reliable code enabling error-free processing of all major evaluated nuclear data libraries.

7 NUCLEAR DATA LIBRARIES FOR ADS CALCULATIONS

7.1 CREATION OF TEMPERATURE DEPENDENT NUCLEAR DATA LIBRARIES FOR MONTE CARLO CALCULATIONS.

Advanced simulations of Accelerator Driven Systems require very reliable nuclear data with a proper treatment of neutron cross-section resonances, particularly their Doppler broadening. Therefore temperature dependent neutron cross-sections are necessary to obtain precise simulation results required for nuclear safety calculations and for precise estimation of multiplication of subcrtical systems.

Moreover, it is essential for Monte Carlo burnup calculations to normalise properly generation of heat (power) in ADS including contribution coming from gamma/beta decay. In order to meet these requirements a unique nuclear data-base has been created for the neutron cross-section in energy range up to 20 MeV. Applying NJOY-processing (see chapter 6.2) for different evaluated nuclear data libraries, temperature dependent neutron-cross section data base has been created for temperatures of 300K, 600K, 900K, 1200K, 1500K and 1800K and for the following data libraries:

- ENDF/B6 version 4, 5 and 6
- JENDL version 3.2
- JEF version 2.2
- EAF version 3.1

This vast amount of data gives us a unique opportunity to perform state-of-the art simulations both for k-eff calculations and burnup evolution. Moreover, handling of different evaluated nuclear data libraries allows us to isolate and assess uncertainties related to nuclear data evaluations. For more detail information we refer to IAEA and NEA benchmark projects [35], [36].

Processing of the evaluated nuclear data enables us also to extend our Monte Carlo calculations to neutron energy ranges much beyond classical reactor-like calculations, i.e. beyond 20 MeV.

In previous data libraries, used by MCNP, neutrons, protons and electrons could be transported, and only up to energies of 20 MeV. To ameliorate this, new high-energy nuclear data files are being produced, for example LA150. The first extension of LA150 is the upper energy limit of evaluated nuclear data to 150 MeV, and the second is the inclusion of evaluated data for all particles of interest. The reason for choosing 150 MeV as an upper energy limit is that the physics models tend to be very good above this limit, while less accurate below it. The LA150 evaluations are a combination of the existing ENDF/B-VI.5 data and of newly evaluated data from 20 to 150 MeV.

7.2   NEUTRON AND PROTON CROSS-SECTION EVALUATIONS FOR ^{232}TH, ^{238}U AND ^{239}PU FOR ENERGY RANGE UP TO 150 MEV

In collaboration with a Russian group from the Institute of Physics and Power Engineering (IPPE) in Obninsk and partially in the frame of the European Project "IABAT" (see Appendices III and V) neutron and proton cross section evaluations have been performed for ^{232}Th, ^{238}U and ^{239}Pu as a part of broader international activities of building up intermediate energy nuclear data libraries [39]. Here we report only a short of review of the improvements to our data files. More details can be find in Appendices III and V and in [40].

^{232}Th file has been corrected and improved compared to the previously reported results. The set of new optical model parameters has been estimated from the analysis of experimental data of neutron total cross sections, angular distributions for proton elastic scattering and proton absorption cross sections. These parameters are shown in Table 7-1.

Table 7-1. Optical potential parameters for neutrons and protons on ^{232}Th.

Well depth (MeV)	Energy Range (MeV)	Geometry (fm)
$V_r = = 51.5 \pm 16\eta - 0.242E + \Delta_c$	$0 < E < 40$	$r_R = 1.21; a_R = 0.7$
$V_r = 50.58 \pm 16\eta - 0.219E + \Delta_c$	$40 < E < 100$	$r_v = 1.21, \quad a_v = 0.7$
$V_r = 49.34 \pm 16\eta - 0.2066E + \Delta_c$	$100 < E < 150$	$r_v = 1.21, \quad a_v = 0.7$
$\Delta_c = 0.4Z/A^{1/3}$		$r_{coul} = 1.26$
$W_d = 2.079 \pm 5\eta + 0.686E - 2.12 10^{-2}E^2$	$0 < E < 20$	$r_d = 1.455 - 2.81 10^{-2}E + 7.625 10^{-4}E^2,$
		$a_d = 0.621 + 8.61 10^{-3}E,$
		$E < 15$ MeV
		$a_d = 0.75, E > 15$ MeV
$W_d = 9.619 \pm 5\eta - 0.123E + 4.0 10^{-4}E^2$	$20 < E < 150$	$r_d = 1.2, a_d = 0.75, E > 15$ MeV
$W_V = 0.0$	$0 < E < 14.2$	
$W_v = -1.708 + 0.122E - 2.2 10^{-4}E^2$	$14.2 < E < 100$	$r_v = 1.26, a_v = 0.35 + 1.8 10^{-3}E$
$W_v = 0.692 + 0.098E - 2.2 10^{-4}E^2$	$100 < E < 150$	$r_v = 1.26, a_v = 0.35 + 1.8 10^{-3}E$
$V_{SO} = 6.18$	$0 < E < 200$	$r_{SO} = 1.16; a_{SO} = 0.667$

Here $\eta = (A-2Z)/A$; $\beta_2 = 0.196$, $\beta_4 = 0.07$ and the scheme of $0^+ - 2^+ - 4^+ - 6^+$ coupled levels is adopted.

8   SUB-CRITICAL EXPERIMENTS – MUSE EXPERIMENT

8.1   INTRODUCTION

The basic idea with ADS is to supply a sub-critical reactor core with neutrons generated by an intense external neutron source. Such an idea is being investigated in the MASURCA experimental facility at CEA/Cadarache in the framework of the MUSE experiments (<u>MU</u>ltiplication avec <u>S</u>ource <u>Ex</u>terne). A large range of different configurations and several different sub-critical levels are being investigated. In the first two MUSE experiments (MUSE-1 [42] and MUSE-2 [43]) a Californium source (neutron yield of $8 \cdot 10^7 \, n/s$) was placed at the centre of the core in order to sustain the neutron multiplication, while a neutron generator using *(d,t)*-fusion reactions was utilised in MUSE-3 [44].

In MUSE-4 [45] the high intensity pulsed neutron generator GENEPI [46], constructed by CNRS/ISN/Grenoble, will be used to accelerate a 250 keV deuteron beam towards either a deuterium target or a tritium target, creating two different neutron spectra. The created *(d,d)*-neutrons have an energy between 2 and 3 MeV, and the *(d,t)*-neutrons of 14 MeV. A future goal in the research would be to couple a high energetic proton accelerator (~GeV) to a sub-critical reactor core. Such a proton beam impinging on a heavy target releases a large number of neutrons via spallation reactions.

The Monte Carlo calculations described in this report aim at investigating the neutron source effects in a sub-critical media and at determining the source *representativity*, i.e. - how well the system with a *(d,d)*- or a *(d,t)*-source, surrounded by a lead buffer zone, is representative of the same system with a spallation source.

To investigate this representativity, Monte Carlo models have been set up, in which a *(d,d)*-, a *(d,t)*- and a spallation source are coupled to a simplified model of the MUSE-4 configuration. The source representativity has been quantified by calculating and comparing the neutron energy spectra at various positions for the three different sources, and by determining the source efficiency in each case.

The calculations have been performed with MCNP [26] for modelling the systems with the *(d,d)*- and the *(d,t)*-sources and with MCNPX [33] for modelling the 1000 MeV protons creating the spallation source. However, the nuclear data files used this far (ENDF/B-6.4) do *not* include the high-energy range from 20 MeV up to 150 MeV. For the energy range above 20 MeV, neutron transport relies on the MCNPX theoretical models.

8.2 DESCRIPTION OF THE MUSE-4 CONFIGURATION AND THE NEUTRON SOURCES

The configuration that has been studied is a simplified model in two dimensions of the MUSE-4 configuration, shown below in Figure 8-1. The value of *k-eff* (k_{eff}) obtained with MCNP-4C is 0.95848 (± 53 pcm) for this configuration and the data library used is ENDF/B-6.4. The materials used in the configuration are shown in Table 8-1.

It should be mentioned that the part of the lead region above the GENEPI neutron generator target (Figure 8-1A) is artificial, compared to the actual MUSE-4 configuration in which the lead buffer ends at the position of the neutron generator (z = 85 cm). This was done in order to simplify this investigation: the geometry was made the same as in a typical spallation system (Figure 8-1 B).
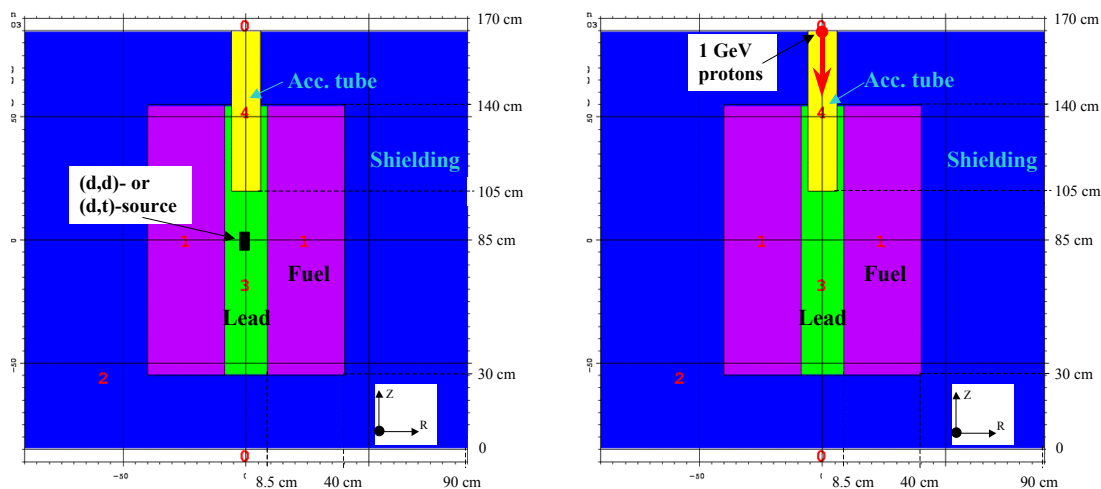

Figure 8-1. Simplified model of the MUSE-4 configuration with 4 regions – k_{eff} » 0.96. A) (d,d)- or (d,t)-source emitted from the GENEPI neutron generator at the centre of the core. B) 1 GeV protons accelerated towards the lead buffer creating a large number of neutrons via spallation interactions.

Three different neutron sources have been considered:

1. **The (d,d)-source** has been simulated with MCNP with the source neutrons emitted from a point at the centre of the core (*r = 0, z = 85 cm,* 0A). The angular and energy dependence of the emitted source neutrons resulting from the GENEPI 250 keV deuterons impinging on a deuterium target are shown in Table 8-2.

2. **The (d,t)-source** has been simulated in the same way, but the angular and energy dependence of the source neutrons were approximated with an isotropic and mono-energetic source of 14 MeV. However, there are pre-defined neutron sources in MCNP for both (d,d)- and (d,t)-reactions, and these will be used in future calculations to avoid unnecessary approximations.

3. **The spallation source:** In order to assess the representativity of the (d,d)- and the (d,t)-sources, a spallation source has been simulated. In this case the extended version of MCNP, MCNPX was used to model the transport and the interactions of 1000 MeV protons with the lead buffer. The protons were

accelerated towards the lead, according to Figure 8-1 B. A large number (~ 20) of neutrons per proton were created in the lead buffer via spallation interactions. The dimensions of the lead target/buffer were *r = 8.5 cm* and *z = 75 cm*.

Table 8-1. Material composition of the simplified model of the MUSE-4 configuration

Material	Isotope	Density [10^{24} atoms/cm^3]	Material	Isotope	Density [10^{24} atoms/cm^3]
Mat 1 – Fuel:	^{239}Pu	1.47e-3	Mat 2 – Shielding:	^{52}Cr	1.5e-2
	^{238}U	5.03e-3		^{23}Na	5.0e-3
	^{56}Fe	7.0e-3		^{56}Fe	5.0e-2
	^{52}Cr	1.5e-3	Mat 3 – Pb	Pb-nat	3.3e-2
	^{23}Na	1.0e-2	Mat 4 – Acc. Tube:	Void	
	^{16}O	1.5e-2			

Table 8-2. Angular and energy dependence of the (d,d)-source neutrons, resulting from the GENEPI 250 keV deuterons impinging on a deuterium target

Angle	Energy	Probability
0	3.050	1.1024
9	3.042	1.1010
18	3.020	1.0969
27	2.984	1.0904
36	2.935	1.0815
45	2.876	1.0706
54	2.808	1.0579
63	2.734	1.0438
72	2.656	1.0287
81	2.576	1.0132
90	2.496	0.9974
99	2.419	0.9819
108	2.346	0.9670
117	2.279	0.9530
126	2.219	0.9403
135	2.167	0.9292
144	2.123	0.9198
153	2.089	0.9123
162	2.064	0.9068
171	2.049	0.9035
180	2.044	0.9024

8.3 BRIEF DESCRIPTION OF THE CALCULATION CODES USED IN THIS STUDY

The two Monte Carlo codes MCNP-4C [28] and MCNPX [33] have been used for of the calculations, with the data library ENDF/B-6.4. Some calculations have also been made with the deterministic code ERANOS [47] using the JEF-2.2 data library.

8.3.1 The Monte Carlo method, MCNP and MCNPX

The Monte Carlo method is, in contrast to deterministic codes, a stochastic method which simulates particle transport in an arbitrary geometry. While deterministic codes solve the Boltzmann transport equation for an *average* particle, Monte Carlo obtains a solution by simulating *individual* particles and then inferring their *average* behaviour. It is particularly useful for complex problems that cannot be modelled by deterministic codes. The problem description is often relatively short an easily constructed. The method consists of following each particle created in a source, throughout its life, from birth to death (absorption, escape etc.), and its interactions with other particles (fission, capture, scattering). The process is run for a large number of source particles to obtain a statistically reliable result and the program records the average behaviour of the simulated particles.

To simulate the particle interaction with matter, nuclear data libraries (i.e. JEF2.2, JENDL-3.2, ENDF/B-6.4) containing cross section information for all relevant isotopes and processes are used. This data is then processed into a format appropriate for MCNP (so called ACER format) by the code NJOY [37], which produces new data files and a "directory" file XSDIR directly used by MCNP.

The basic advantage of Monte Carlo codes over deterministic codes is that they require fewer modelling approximations. In Monte Carlo there are no averaging approximations required in space, energy, and time. A disadvantage of Monte Carlo is that the solution contains statistical errors. All results in Monte Carlo represent estimates with associated uncertainties and the calculations can be rather time consuming as the required precision of the results increases.

The Monte Carlo code that has been used in this investigation is MCNP version 4C and the data library used is ENDF/B-6.4. The energy representation is continuous and the neutron energy range is from 10^{-5} eV to 20 MeV.

MCNPX [33] is an extended version of MCNP where the major capabilities of LAHET [32] and MCNP-4B have been merged together. In MCNP, particle transport relies on nuclear data contained in cross-section tables, which are derived from nuclear data evaluations. In LAHET, on the other hand, particle transport is accomplished by using various theoretical physics models. In MCNPX, the table-based data may be used whenever they exist, as such data are known to yield the best results. When they do not exist, the physics models will be used.

However, the nuclear data file used in all calculations presented in this chapter, is ENDF/B-6.4, which does *not* include the high-energy range up to 150 MeV. Hence, for the energy region from 20 to 1000 MeV, the modelling of the system relies on theoretical models.

8.3.2 ERANOS-code

ERANOS [47] is a deterministic fast reactor code system developed by CEA in collaboration with other R&D labs. It uses cross-section libraries based on JEF2.2 evaluated file. The codes NJOY and CALENDF are used to prepare the data. The ERANOS code is well validated for classical sodium-cooled fast reactors and has been extended to plutonium burning cores with steel-sodium reflectors and high Pu-content. However, it is not yet sufficiently validated for other systems such as systems with uranium free fuel or nitride fuel, with lead and lead-bismuth as coolant, with large sub-criticalities and the presence of high-energy neutrons from spallation.

The ERANOS fast reactor code package is divided into mainly two different parts.

1) **ECCO**

   The first part consists of the cell code ECCO, which produces homogenised macroscopic cross-sections for all specified subassembly-size regions.

2) **Reactor calculations**

   The reactor calculations can be performed either by solving the diffusion equation or the transport equation. There are codes for handling two-dimensional problems and three-dimensional problems:

   a) **BISTRO – 2D** (diffusion or transport S_n code)

   b) **TGV/VARIANT** – 2D or 3D (diffusion or transport variational nodal code)

   c) **H3D – 3D** (diffusion code)

8.4 NEUTRON SPECTRA

8.4.1 Equal-lethargy

The energy limits used for the calculations of the neutron energy distributions have been defined on the basis of the 1968 groups of the ECCO cell code in ERANOS . The lethargy width **D**u of each energy bin is

$$\Delta u = \frac{1}{120} \approx 0.00833 \qquad \qquad 8\text{-}1$$

for the neutron leakage calculations in section 8.4.2 and

$$\Delta u = \frac{1}{20} \approx 0.05 \qquad \qquad 8\text{-}2$$

for all other calculations. The energy limits are defined as

$$E_n = 10 \cdot e^{n/120} \quad n = i, i+1, \dots j \qquad \qquad 8\text{-}3$$

E_n is in MeV and an energy boundary is imposed at 10.000 MeV exactly.

8.4.2   Neutron distribution in the lead buffer, without fuel or shielding

To investigate the properties of the sources and the neutron propagation in the lead alone, the surrounding fuel and shielding were temporarily removed (Figure 8-2). The neutrons are recorded when they cross the outer surface of the lead buffer (marked with the thick red line).

It should be mentioned again, that the part of the lead region above the *(d,d)-* and the *(d,t)*-sources (Figure 8-2A) has been added in order to obtain the same geometry as in a typical spallation system.
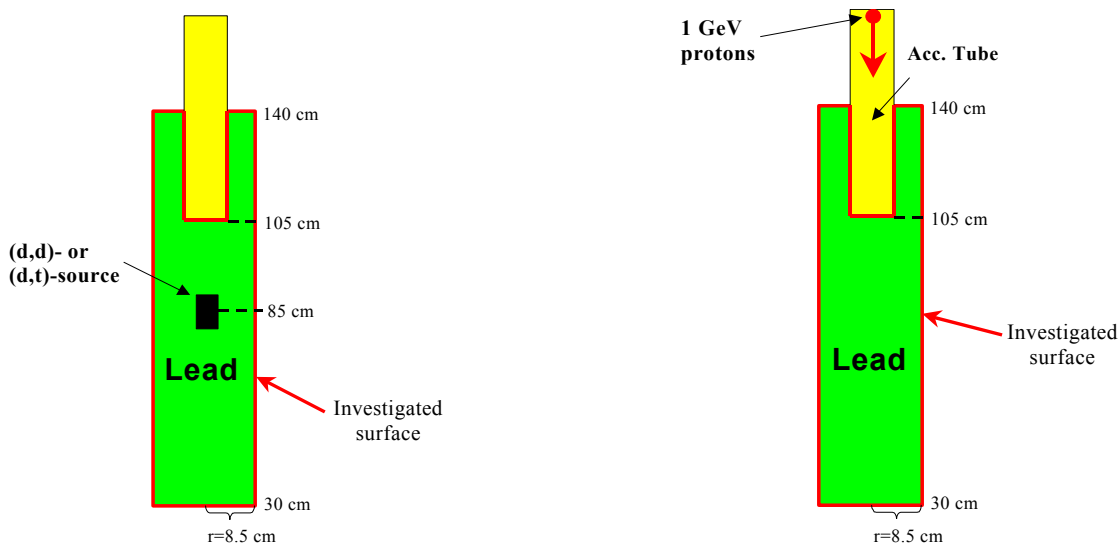
Figure 8-2. Configuration with only the accelerator tube surrounded by the lead buffer region. The read thick line marks the buffer surface being studied. A) (d,d)- or (d,t)-source emitted in the centre of the core. B) 1 GeV protons accelerated towards the lead buffer creating a large number of neutrons via spallation.

Neutron leakage spectrum from the lead buffer

The energy spectra of the neutrons exiting the lead region are plotted in Figure 8-3A (logarithmic x-scale) and in Figure 8-3B (linear x-scale). The following remarks can be made about the neutron fluxes:

- The *(d,d)-spectrum* has a large peak between 2 and 3 MeV, which is the energy range where the neutrons are born in the *(d,d)*-fusion reaction. Hence, only a small fraction of the source neutrons has been slowed down by the lead. The *(d,d)*-leakage spectrum is also shown in Figure 8-4.

- For the *(d,t)-source*, a large part of the source neutrons has been slowed down by scattering and *(n,2n)*-reactions in the lead and the spectrum has a maximum at a little less than 2 MeV. However, 32 % of the neutrons exiting the lead buffer have not interacted with the lead and are still in the 14-MeV peak.

  The peaks in the region between 9 and 12 MeV from the *(d,t)*-source are due to inelastic scattering with the three main stable isotopes of lead, A = 206, 207 and

208. The 14 MeV neutrons excite the nuclei to a certain excited energy state and loose a certain amount of energy in each reaction. Each peak has been identified with an excited state for one of the lead isotopes and the cross-sections of these inelastic reactions *(n,n´)* have been found to be large, while much smaller for all other *(n,n´)*-reactions.

- For the **spallation source**, most of the source neutrons have been slowed down and the spectrum has a shape similar to the *(d,t)*-leakage spectrum, but with even more neutrons slowed down. 7.5 % of the neutrons still have an energy higher than 20 MeV and 2.1 % higher than 100 MeV.

  However, there is a discontinuity in the spectrum at 20 MeV, due to the change from using cross-section table data to using theoretical physics models. The actual values of the high-energy fractions are therefore probably a little lower than 7.5% and 2.1%.
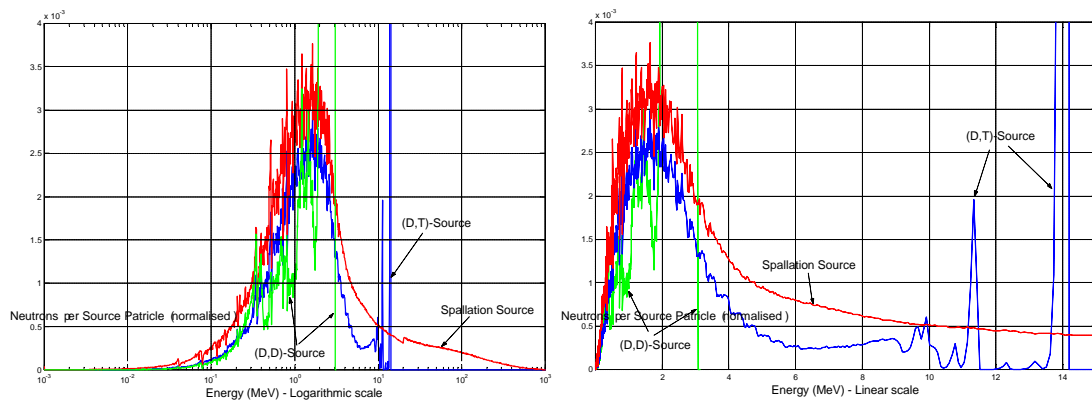

Figure 8-3. Neutron leakage spectrum at the outer surface of the lead buffer zone for a (d,d)-source, a (d,t)-source and a spallation source – the surrounding fuel and shielding are removed! A) Logarithmic x-scale. B) Linear x-scale.
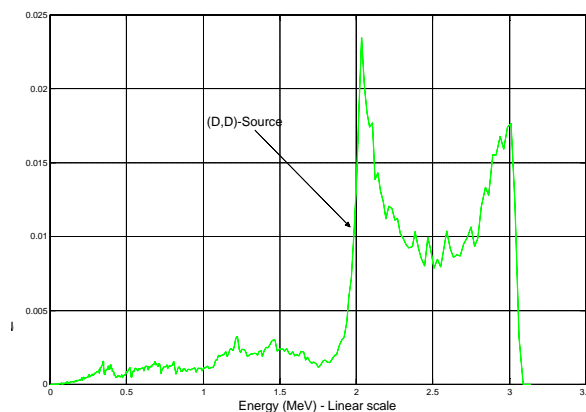

Figure 8-4. Neutron leakage spectrum at the outer surface of the lead buffer zone for a (d,d)-source –Lin-lin scale.

8.4.3   Simplified model of the MUSE-4 configuration, fuel and shielding present

In this section the simplified model of the MUSE-4 configuration shown in Figure 8-1 has been simulated with all four regions present. The neutron energy spectrum has been calculated at four different positions (r = 0, 10, 20 and 30 cm, see Figure 8-5).
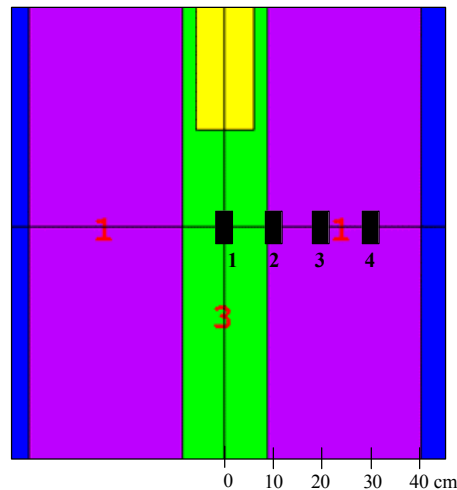

Figure 8-5. The four positions (r = 0, 10, 20 and 30 cm) in the simplified configuration (4 regions) of MUSE-4, where the neutron energy spectra have been calculated.

The results are plotted in Figures 8-6 and 8-7. The following observations can be made about the neutron spectra:

- **Position 1 (*r = 0,* Figure 8-6 A):** At the centre of the core, at the position where the *(d,d)*- and the *(d,t)*-source neutrons are emitted, the source peaks are evidently very large. 45 % of the *(d,t)*-neutrons are in the 14 MeV peak and even more of the *(d,d)*-neutrons are in the peak at 2 to 3 MeV. However, many neutrons created in the fuel enter into the lead buffer and most spectral characteristics of the fuel are visible.

  For the spallation source, a non-negligible fraction of the neutrons are still in the high-energy range above 20 MeV, but most of them have been slowed down or are coming from the fuel.

- **Position 2 (*r = 10 cm,* Figure 8-6 B):** Already 10 cm from the centre of the core, 1.5 cm into the fuel, the spectra from the three different sources are very similar and are largely dominated by the multiplication and the characteristics of the fuel. The two dips in the neutron fluxes, caused by the resonances in sodium (~ 3 keV) and oxygen (~ 0.4 MeV) are very clear. The fractions of source neutrons from the *(d,d)*- and the *(d,t)*-sources are small, but should not automatically be disregarded. 1.6 % of the *(d,t)*-neutrons are still in the 14 MeV peak.
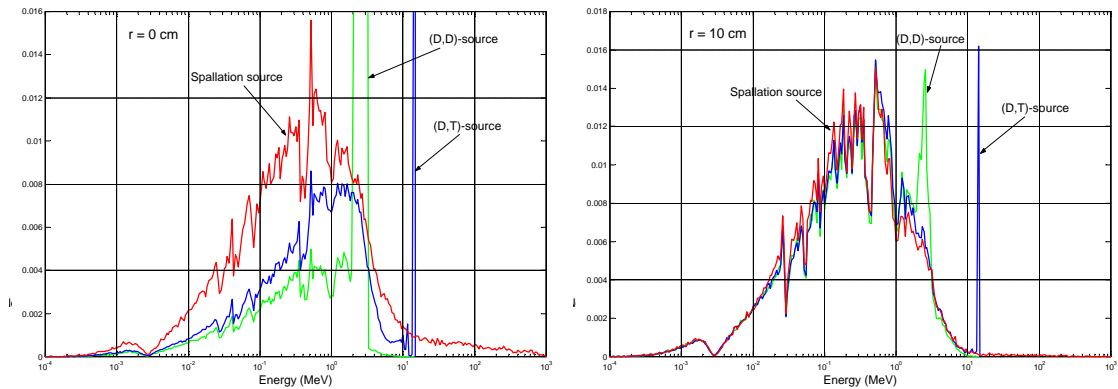
Figure 8-6. Neutron energy distribution in the simplified model (4 regions) of the MUSE-4 configuration for the three sources. A) Position 1 (r = 0). B) Position 2 (r = 10 cm)

- **Position 3 and 4 (*r = 20, 30 cm*,** Figure 8-7 A and B**):** The spectra look about the same as at 10 cm from the centre, but they are even more dominated by neutron multiplication and the other characteristics of the fuel. The *(d,d)*- and the *(d,t)*-source neutrons have almost vanished (though still visible, 0.3 % and 0.1 % respectively of the neutrons still being in the 14 MeV peak.). Hence, the origins of the sources can for most applications be considered as "forgotten" in these regions of the fuel.
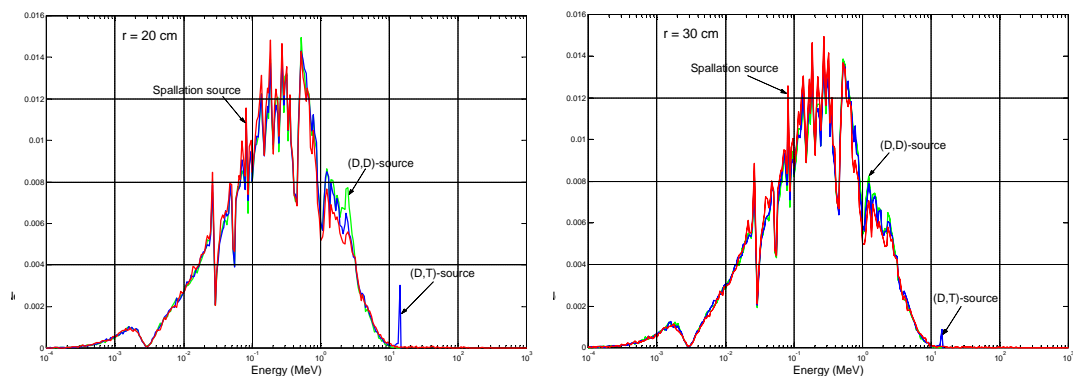

Figure 8-7. Neutron energy distribution in the simplified model (4 regions) of the MUSE-4 configuration for the three sources. A) Position 3 (r = 20 cm). B) Position 4 (r = 30 cm)

8.4.4   Energy spectrum of spallation source neutrons

The neutron yield per proton and the neutron spectrum in a spallation system are very sensitive to the shape of the target. In this section the energy spectrum of spallation neutrons as a function of the target radius and target height has been investigated.

Energy spectrum versus target radius

In these simulations the target consisted of a cylinder with a fixed height of 50 cm and a radius varying from 5 to 20 cm (Figure 8-8). As is seen in Figure 8-8, and as expected, the peak of the spectrum moves towards lower energies with increasing radius of the

lead target. With the radii of 5 cm and 10 cm, the peaks are at a little more than 2 MeV and a little less than 2 MeV respectively, while the neutron spectrum in the case of the 20 cm radius peaks at about 1 MeV. The fractions of neutrons above 20 MeV and 100 MeV for the different cases are shown in Table 8-3.
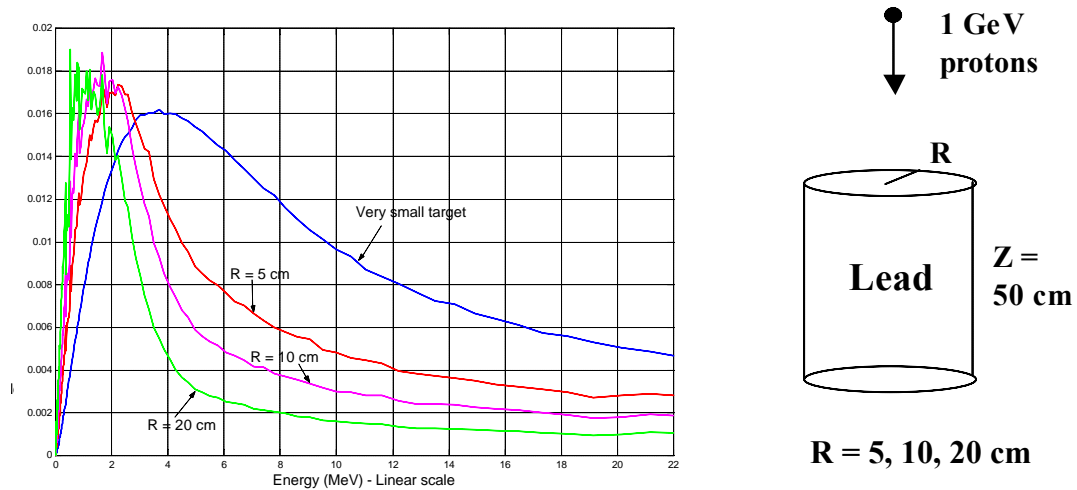

Figure 8-8. Neutron energy spectrum of spallation source neutrons versus lead target radius (z = 50 cm), computed with MCNPX.

Table 8-3. Fractions of neutrons above 20 MeV and 100 MeV from spallation source with varying target radius

Target radius	E > 20 MeV	E > 100 MeV
20 cm	3.7 %	1.1 %
10 cm	6.9 %	2.2 %
5 cm	10.9 %	3.7 %
Very small target	15.6 %	3.9 %

Very small target

With a very small target (1 mm thick) practically no scattering occurs and the neutrons released have significantly higher energies than in the thick-target cases. The spectrum peaks at a little less than 4 MeV and a rather large part (15.6 %) of the neutrons are still in the energy range above 20 MeV. This spectrum is plotted in 0 and in lin-log and log-log scale in Figure 8-9 A and B.
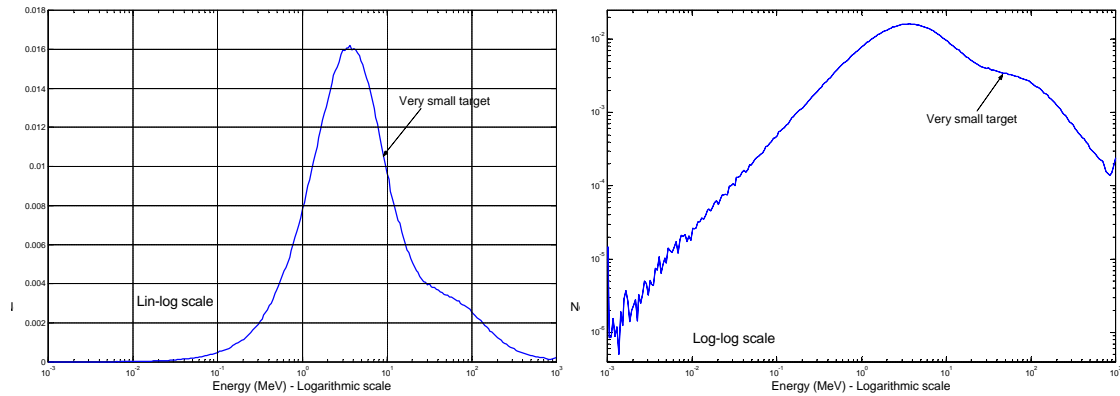
Figure8-9. Neutron energy spectrum originating from 1000 MeV protons impinging on a very small lead target. A) Lin-log scale. B) Log-log scale.

Energy distribution versus target height

In this case the target consisted of a cylinder with a fixed radius of 20 cm and a height varying from 25 to 100 cm (Figure 8-10). It is seen in the figure that the distribution of the neutron yield is relatively insensitive to the height of the target when it is increased beyond 50 cm, i.e. saturation is reached.
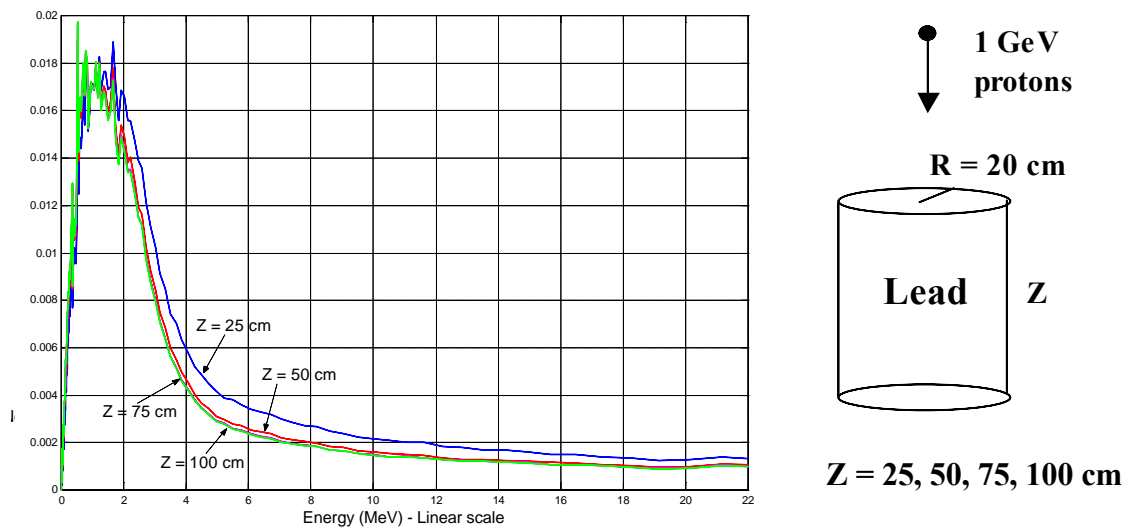

Figure 8-10. Neutron energy spectrum of spallation source neutrons versus lead target height (r = 20 cm), computed with MCNPX.

8.4.5 Conclusion on spectrum studies

The investigation of the neutron leakage spectra at the outer surface of the lead buffer shows that, a large part of the neutrons from the *(d,t)-* and the spallation sources have been slowed down when they exit the buffer, while most of the *(d,d)*-source neutrons are unperturbed.

The origins of the neutron sources, coupled to the simplified model of the MUSE-4 configuration, have been found to be almost "forgotten" at distances of ~20 cm or more into the fuel.

It has also been found that the neutron spectrum moves towards lower energies with increasing target radius and that saturation in the spallation neutron moderation is reached at a depth of about 50 cm.

8.5   SOURCE EFFICIENCY

The source efficiency has been determined for the simplified model of the MUSE-4 configuration, shown in 0. MCNP has been used to simulate the *(d,d)*- and the *(d,t)*- source and MCNPX to simulate the spallation source. In addition to this, the source efficiency for the *(d,t)*-source has also been determined with ERANOS.

8.5.1   Deriving j*

To determine the source efficiency with MCNP and MCNPX, we started from the following two neutron balance equations:

$$< Af >=< Pf > + < S >$$ 8-4

$$< Af >= \frac{1}{k_s} \cdot < Pf >$$ 8-5

where

$<Af>$ = Total absorption + leakage rate of neutrons

$<Pf>$ = Total production rate of neutrons *(Fission + (n,xn)-reactions + other nuclear interactions)*

$<S>$ = Production of neutrons by external source

and from the expression for *k-source* (k_s):

$$k_s = \frac{< Pf >}{< Pf > + < S >} = \frac{F + X + NI}{F + X + NI + S}$$ 8-6

where

F = Neutrons produced by fission

X = Neutrons produced by *(n,xn)*-reactions induced by neutrons with energy below 20 MeV

NI^l = Neutrons produced by "nuclear interactions" induced by neutrons with energy above 20 MeV

From the values obtained for k_{eff} and k_s, the source efficiency j* can then be determined, according to:

---

[1] Neutrons produced by *"nuclear interactions"*, weighted per source neutron. The neutrons produced by neutrons with an energy higher than 20 MeV (spallation and other secondary reactions) are labelled "Nuclear Interactions" in MCNPX

$$j^* = \frac{\frac{1}{k_{eff}} - 1}{\frac{1}{k_s} - 1}$$

8-7

Alternatively, with k_s replaced by its expression (eq. 8-6), the above expression for j^* can be rewritten as:

$$j^* = \left(\frac{1}{k_{eff}} - 1 \right) \cdot \left(\frac{F + X + NI}{S} \right)$$

8-8

The above quantities can all be computed with MCNP and MCNPX.

8.5.2   Error estimation of j^* for the *(d,t)*-source

To get an estimate of the statistical uncertainty in the source efficiency, assume first that the relative errors of *F*, *X* and *S* are **DF**, **DX** and **DS** and apply the formula for "propagation of error" 0. The error has been determined for the system with the *(d,t)*-source only. Note that in the case of 14 MeV source neutrons, there is no contribution from any "nuclear interactions" (*NI* in 0).

$$\Delta f(x_1, x_2, ...) = \sqrt{\left(\frac{\partial f}{\partial x_1} \Delta x_1 \right)^2 + \left(\frac{\partial f}{\partial x_2} \Delta x_2 \right)^2 + ... + r_{12} \cdot \frac{\partial f}{\partial x_1} \Delta x_1 \cdot \frac{\partial f}{\partial x_2} \Delta x_2 + ...}$$

8-9

From this formula, the relative errors in k_s can first be calculated. The correlation constant **r** could either be positive or negative – negative if k_{eff} and k_s are correlated and positive if they are anti-correlated. However, to determine **r** is a rather difficult task, and as a first approximation **r** will be assumed to be zero. The derivatives, from which **D**k_s can be calculated, are in this case

$$\frac{\partial k_s}{\partial F} = \frac{\partial k_s}{\partial X} = \frac{S}{(F + X + S)^2}$$

8-10

and the expression for **D**k_s becomes

$$\Delta k_s \approx \sqrt{\left(\frac{\partial k_s}{\partial F} \Delta F \right)^2 + \left(\frac{\partial k_s}{\partial X} \Delta X \right)^2}$$

8-11

To determine the error in j^*, we have for the derivatives of j^*

$$\frac{\partial j^*}{\partial k_{eff}} = -\frac{1}{k_{eff}^2 \cdot \left(\frac{1}{k_s} - 1 \right)} = \frac{-j^*}{k_{eff}} \cdot \frac{1}{1 - k_{eff}}$$

8-12

$$\frac{\partial j^*}{\partial k_s} = \left(\frac{1}{k_{eff}} - 1 \right) \cdot \frac{1}{(1 - k_s)^2} = \frac{j^*}{k_s} \cdot \frac{1}{1 - k_s}$$

8-13

From these two derivatives and eq. 8-9 the final expression for the relative error in j^* can be obtained.

$$\left(\frac{\Delta \boldsymbol{j}*}{\boldsymbol{j}*}\right)^2 \approx \left(\frac{\partial \boldsymbol{j}*}{\partial k_{eff}} \cdot \frac{k_{eff}}{\boldsymbol{j}*} \cdot \frac{\Delta k_{eff}}{k_{eff}}\right)^2 + \left(\frac{\partial \boldsymbol{j}*}{\partial k_s} \cdot \frac{k_s}{\boldsymbol{j}*} \cdot \frac{\Delta k_s}{k_s}\right)^2 = \left(\frac{1}{1-k_{eff}} \cdot \frac{\Delta k_{eff}}{k_{eff}}\right)^2 + \left(\frac{1}{1-k_s} \cdot \frac{\Delta k_s}{k_s}\right)^2 \qquad 8\text{-}14$$

The result obtained from the MCNP simulation with the *(d,t)*-source was

$$\boldsymbol{j}* = 2.15 \ and \quad \frac{\Delta \boldsymbol{j}*}{\boldsymbol{j}*} = 0.030 \ Þ \ \Delta \boldsymbol{j}* = 0.065 \qquad\qquad 8\text{-}15$$

It should be noted that, in the rigorous error estimation of $\boldsymbol{j}*$, k_{eff} *and* k_s are correlated and $\boldsymbol{r}$ is negative. Hence, the actual statistical errors in $\boldsymbol{j}*$ are in fact smaller than those given by eq 8-14. All values used in the calculations are presented in Table 8-4 in the next section.

8.5.3   Source efficiency for neutrons emitted at the centre of the core

Source efficiency calculated with MCNP and MCNPX

The efficiency of the neutrons emitted from the *(d,d)*- and the *(d,t)*-source at the centre of the core ($r = 0$, $z = 85$, as shown in Figure 8-1) and of the neutrons created in the lead buffer via spallation, has been determined. As was mentioned earlier, the part of the lead region above the *(d,d)*- and the *(d,t)*-sources (Figure 8-2A) has been added in order to obtain the same geometry as in a typical spallation system, and this has an effect on the results of the source efficiency.

The results are shown in Table 8-4 and it is seen that, for each 14-MeV neutron from the *(d,t)*-source emitted isotropically at the centre of the core, about 50 neutrons are produced in the entire core. At this reactivity level of $\boldsymbol{r} \sim$ -4300 pcm, $\frac{1}{k_{eff}} - 1$ (see eq. 8-8) is equal to 0.0433 and the source efficiency is 2.15.

The reason for the high value of $\boldsymbol{j}*$ for the *(d,t)*-source is the larger fission rate, part of which coming from fissions induced by the neutrons multiplied by *(n,2n)*-reactions in the lead buffer (compare cross-section plot in Figure 8-11). It is seen in Table 8-8 that the number of fission neutrons per source neutron is large (48.2), which arises from the emitted *(n,2n)*-neutrons in the lead having the right energy to induce fission, particularly above the [238]U threshold.

In the case of the spallation source, the MCNPX results have been renormalized to 1 source neutron. The raw MCNPX results in parentheses are normalised "per source particle", which in this case are protons. With our target dimensions of $r = 8.5$ cm and $z = 75$ cm, about 21 neutrons, per emitted source *proton*, are created in the lead buffer, by "Nuclear Interactions[4]" and other secondary reactions. The way to define the source neutrons created from the spallation interactions is explained in section 8.7 and the results used to calculate the number of source neutrons produced per source proton, are shown in Tables 8-7 and 8-8. When these neutrons, created in the lead target, are considered as fixed source neutrons, there are about 29 neutrons per source particle created in the rest of the core, mainly by fission. The value obtained for the source efficiency is 1.28, which is considerably lower than for the *(d,t)*-neutrons.

Table 8-4. Source efficiency for the (d,d)-source and the (d,t)-source calculated with MCNP (ENDF/B-6.4), and the spallation source calculated with MCNPX (ENDF/B-6.4). The configuration studied is the simplified model of the MUSE-4 configuration.

Source	k_{eff}	F^2	X^3 (n,xn)	NI^4	S^5	k_s	$j*$
(D,D)	0.95848 (± 53 pcm)	28.8	0.09	-	1.0	0.96643	**1.25**
(D,T)	0.95848 (± 53 pcm)	48.2 (± 1.3)	1.36 (±<0.1)	-	1.0	0.9802 (± 59 pcm)	**2.15 (± 0.065)**
Spall. source	0.95848 (± 53 pcm)	29.0 $(610)^6$	0.14 $(2.8)^6$	0.42 $(8.4)^6$	1.0 $(21.04)^6$	0.96700	**1.28**

On the other hand, the source efficiency for the *(d,d)*-source neutrons is 1.25, which is close to the value for the spallation source. Hence, considering the source efficiency, a *(d,d)*-source coupled to the simplified model of the MUSE-4 configuration is potentially a better substitute for a spallation source than a *(d,t)*-source is. The value of *j* * alone is not sufficient to conclude about "representativity", but the results show that a *(d,d)*-source and a spallation source lead to about the same number of *(n,xn)*- and fission neutrons.
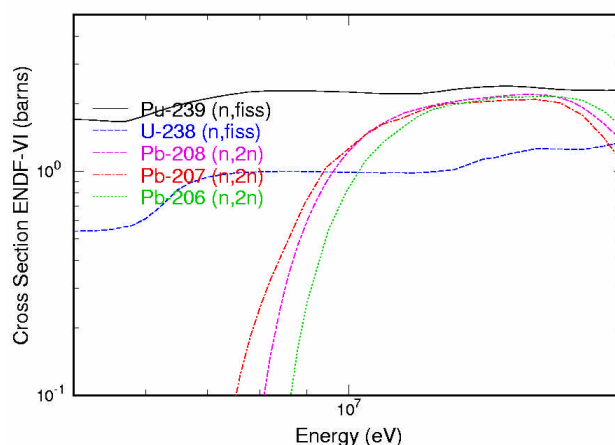

Figure 8-11. Neutron microscopic (n,2n) cross-sections for ^{239}Pu fission, ^{238}U fission and $^{206, 207, 208}Pb$.

---

[2] Neutrons produced by ***fission***, weighted per source neutron.

[3] Neutrons produced by ***(n,xn)-reactions***, by neutrons having an energy lower than 20 MeV, weighted per source neutron.

[4] Neutrons produced by ***"nuclear interactions"***, weighted per source neutron. The neutrons produced by neutrons with an energy higher than 20 MeV are labelled "Nuclear Interactions" in MCNPX.

[5] Neutrons emitted by ***external source***, weighted per source neutron.

[6] Values in parentheses are per source ***proton***.

Source efficiency for the (D,T)-source calculated with ERANOS

To corroborate the results obtained with MCNP, two ERANOS calculations have been performed for the same configuration (Figure 8-1)-one determining k_{eff} and one determining k_s. The calculations have been performed with JEF-2.2 data and the BISTRO S_n module [48], which solves the neutron transport equation. Due to convergence problems, the *(d,t)*-source at the centre of the core has been distributed over a somewhat larger volume, a cylinder with a radius of 6 cm and a height of 21 cm. This has been justified by rerunning the MCNP-calculations with the same source geometry, which did not change the source efficiency significantly. The simulations have only been performed for the system with the *(d,t)*-source. The results are shown in Table 8-5.

Table 8-5. Source efficiency for the (d,t)-source calculated with MCNP (ENDF/B-6.4) and ERANOS (JEF-2.2)

	Code	k_{eff}	k_s	$j*$
(D,T)-Source	**MCNP**	0.95848	0.98022	**2.15 (±0.065)**
	ERANOS	0.94299	0.97470	**2.33**

The 1500 pcm difference in k_{eff} is very large, but it has been found in other benchmarks and is partly due to differences in nuclear data libraries. It is being investigated more deeply in the MUSE-4 simplified benchmark, for which the same difference between ERANOS with JEF-2.2 and MCNP with ENDF/B-6.4 appears. The difference between the computed $j*$ is about 8 %, which is fairly good, in view of the large difference in k_{eff}.

Source efficiency as a function of neutron energy for point sources at the centre of the core

Another way to show the effect of the *(n,2n)*-multiplication in the lead buffer is to calculate $j*$ for mono-energetic point sources of different energies. In Figure 8-12, the MCNP-computed value of $j*$ is plotted versus source neutron energy for the energy range from 0.25 MeV to 15 MeV.

It is seen that the curve starts to increase at about 7 MeV, in accordance with the energy threshold of the *(n,2n)*-reaction in lead, plotted in Figure 8-11. The value for the lead *(n,2n)*-cross section at 14 MeV is about 2.0 barn, which is comparable to the fission cross-section in ^{239}Pu and in ^{238}U. The value of $j* = 2.15$ for the 14 MeV *(d,t)*-neutrons is recognised from Table 8-4 and the values of about 1.25 to 1.30 at 2 to 3 MeV correspond to the *(d,d)*-source neutrons.

8.5.4 Decomposition of $j*$ for the spallation source

Most reactor code simulations only take into account neutrons with energies lower than 20 MeV. However, a significant fraction of the neutrons produced by spallation have an energy greater than 20 MeV and the contribution of these high-energy neutrons to the

source efficiency has been investigated. For this, the spallation source was artificially split into two parts: neutrons with energies below 20 MeV (subscript L) and neutrons with energies above 20 MeV (subscript H).
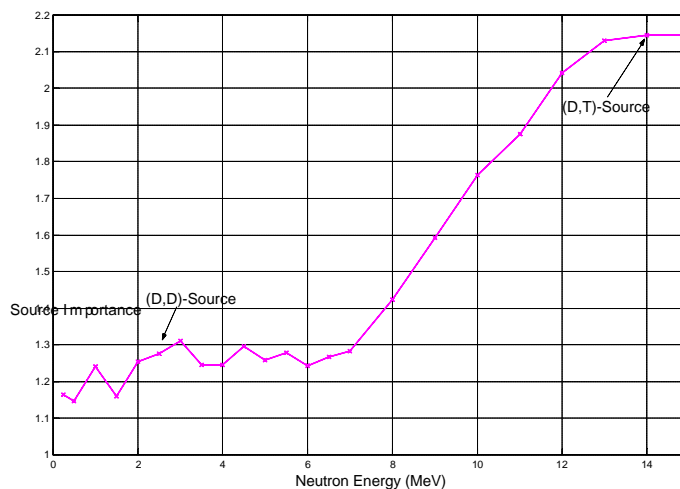

Figure 8-12. $j*$ *versus neutron energy for various point sources of mono-energetic neutrons placed at the centre of the core of the simplified model of the MUSE-4 configuration (Figure 8-1).*

A formula for low- and high-energy contributions to $j*$

We start from the following basic relationship for the source efficiency (equivalent to eq. 8-8)

$$j_I^* = \frac{\dfrac{< f_0^* S_I >}{< S_I >}}{\dfrac{< f_0^* P f_I >}{< P f_I >}} = \frac{\dfrac{< P f_I >}{< S_I >}}{\dfrac{< f_0^* P f_I >}{< P f_I >}} = \left(\frac{1}{k_{eff}} - 1 \right) \cdot \frac{< P f_I >}{< S_I >}$$

8-16

where

Subscript I stands either for the total source (S_T), the source including only neutrons below 20 MeV (S_L) or the source including only neutrons above 20 MeV (S_H)

f_I = Flux created by each source (S_T ® f_T, S_L ® f_L, S_H ® f_H)

f_0^* = Adjoint flux of critical reactor

$<Pf>$ = Total production rate of neutrons *(Fission + (n,xn)-reactions + other nuclear interactions)*

$<S>$ = Production of neutrons by external source, normalised to 1

Since k_{eff} is the same in all cases and since

70

$$< Pf_T >=< Pf_L > + < Pf_H >$$ 8-17

the following relationship for the decomposition of $j*$ can easily be derived:

$$j_T^* < S_T >= j_L^* < S_L > + j_H^* < S_H >$$ 8-18

where

j_T^* = Source efficiency for the total source (S_T)

j_L^* = Source efficiency for source neutrons below 20 MeV (S_L)

j_H^* = Source efficiency for source neutrons above 20 MeV (S_H)

     or

$$\boxed{j_T^* = j_{<20}^* + j_{>20}^*} \quad where \begin{cases} j_{<20}^* = j_L^* \cdot \dfrac{< S_L >}{< S_T >} \\[2ex] j_{>20}^* = j_H^* \cdot \dfrac{< S_H >}{< S_T >} \end{cases}$$ 8-19

     and

$j_{<20}^*$ = Contribution to j_T^* by source neutrons below 20 MeV

$j_{>20}^*$ = Contribution to j_T^* by source neutrons above 20 MeV

The production terms may be written as

$$< Pf_I >= F_I + X_I + NI_I$$ 8-20

where

F = Neutrons produced by fission

X = Neutrons produced by *(n,xn)*-reactions by neutrons with energy below 20 MeV

NI^7 = Neutrons produced by "nuclear interactions" by neutrons with energy above 20 MeV

These quantities can all be explicitly calculated by MCNPX, as is explained in the next section.

---

[7] Neutrons produced by **"nuclear interactions"**, weighted per source neutron. The neutrons produced by neutrons with an energy higher than 20 MeV are labelled "Nuclear Interactions" in MCNPX.

Calculating low-energy and high-energy contributions to $j*$

To calculate the low-energy and high-energy contributions to $j*$, the spallation process with 1000 MeV protons impinging on a lead target (cylinder with $z = 40\ cm,\ r = 5\ cm$) was simulated and the neutron energy distribution in the lead was recorded. A neutron source, with the same dimensions and the same energy spectrum (approximately the same as in Figure 8-8), was then placed at the centre of the lead buffer in the simplified model of the MUSE-4 configuration (Figure 8-13). The neutrons were here distributed homogeneously in the cylinder and emitted isotropically.
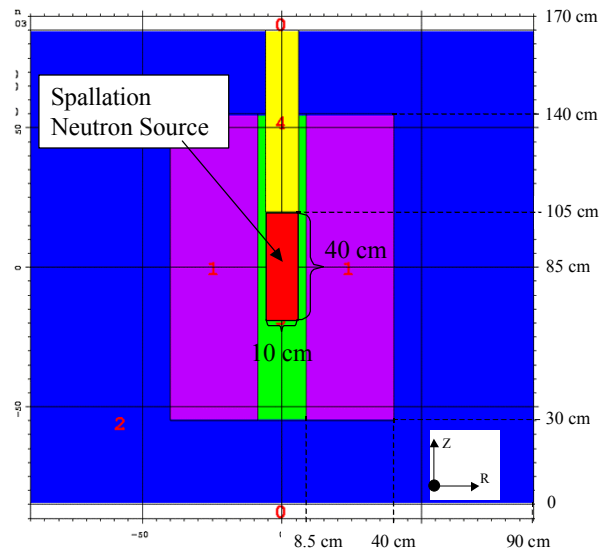

Figure 8-13. The homogenous and isotropic spallation neutron source placed in the simplified model of the MUSE-4 configuration.

The source efficiency was calculated with MCNPX for the two different parts of the source. The results obtained are shown in Table 8-6. As is seen in the table, with the entire source simulated, $j*_T = 1.84$. The source efficiency for the neutrons with an energy between 20 MeV and 1000 MeV (10.8 % of total amount of source neutrons) is very high ($j*_H = 6.13$), which is due to the spallation neutrons (compare with Figure 8-14). For the low-energy part (E<20 MeV), the value is rather low, $j*_L = 1.26$.

It is also shown that the low-energy part of the neutrons contributes with 1.12 (63 %) to $j*$, while the high-energy part with 0.66 (37 %). The sum of these contributions, according to eq. 8-19, is 1.78. This value should theoretically be identical to the value from the calculation performed with the entire spallation source present ($j*_T = 1.84$). It is not, but the results are in fairly good agreement (3 % discrepancy). The result is summarised in eq. 8-21.

$$j*_T = j*_{<20} + j*_{>20} = 1.12 + 0.66 \approx 1.8 \qquad\qquad 8\text{-}21$$

The reason for the high value of $j*_T$ (1.84), compared to 1.28 in Table 8-4, is that the spallation source neutrons have here been emitted isotropically. In the actual case, most of the high-energy neutrons are strongly peaked in the forward direction and exit the

core without interfering with the fuel. Hence, there is no contribution of further spallation reactions or other secondary reactions in the fuel from these neutrons. In future calculations, the decomposition of the spallation source will be performed with the source neutrons emitted with a correct angular distribution. Nevertheless, these results indicate that the method of decomposing the source is valid and provides valuable insight into the system physics.

Table 8-6. Decomposition of φ^*, calculated with MCNPX (subscripts I stands for Low, High and Total)

	F_I	$X (n,xn)$	NI	$<S_I>/<S_T>$ Fraction of neutrons	j_I^* (eq. 8-19)	$j^*_{Contribution}$ [8] (eq. 8-19)
Low E<20 MeV	28.81	0.158	0	0.892	1.26	1.12
High E>20 MeV	134.0	0.79	6.65	0.108	6.13	0.66
Total	41.5	0.23	0.74	1.0	**1.84**	**1.78**[9]

Source efficiency for high-energy leakage neutrons

As was shown in the previous section, neutrons with high energy contribute considerably more to the source efficiency than neutrons with low energy. To get a better view of the contributions to the source efficiency from high-energy neutrons, j^* was plotted versus neutron energy for the energy range up to 1000 MeV (Figure 8-14).
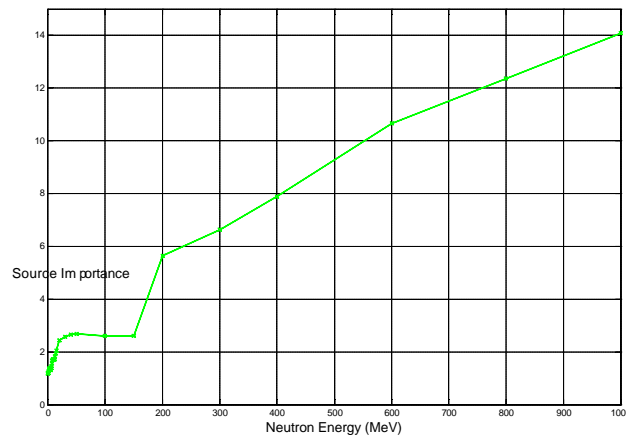

Figure 8-14. j^* versus neutron energy for various point sources of mono-energetic neutrons, for the energy range up to 1000 MeV.

---

[8] $j^*_{Contribution} = j^*_I \cdot$ *fraction of neutrons*

[9] Sum of contributions from S_L and S_H. Should theoretically be identical to the value from the calculation performed with the entire spallation source present ($j^*_T = 1.84$)

As is seen in the figure, the neutrons with an energy of several hundreds of MeV, have very high efficiencies (~ 10), which might contribute significantly to $j\,*$, even though the fraction of these neutrons is very small. To further investigate this, the decomposition of $j\,*$ will be extended to include a larger number of energy bins.

8.6   CONCLUSIONS

Simple calculations have been performed with MCNP and MCNPX to investigate the neutronic properties of various neutron sources placed in a sub-critical core, similar to the MUSE-4 configuration. *(d,d)-*, *(d,t)-* and spallation sources have been studied in terms of spectra and efficiency. In this first study, the nuclear data files used with MCNPX (ENDF/B-VI.4) did *not* include the high-energy cross-section data up to 150 MeV. In future calculations, the ENDF/B-VI.4 data file will be replaced with the LA150 data file, which contains newly evaluated nuclear data for neutron transport in the energy range up to 150 MeV.

The neutron leakage spectra at the outer surface of the 8.5 cm radius lead buffer alone, with the *(d,d)-*, the *(d,t)-* and the spallation sources coupled to it, have been determined. In the case of the *(d,t)-* and the spallation source, most of the source neutrons have been slowed down when they exit the lead buffer, and the peaks of the spectra are found at a little less than 2 MeV. However, a large fraction of the neutrons still have much higher energies, 32 % of the *(d,t)-*neutrons are unperturbed and are still in the 14 MeV peak, and 7.5 % of the spallation neutrons have an energy higher than 20 MeV. For the *(d,d)-* source, only a small fraction of the neutrons have been slowed down and most of them have about the same energy as when they were emitted (2 to 3 MeV).

The calculations determining the neutron spectra for the three sources, coupled to the simplified model of the MUSE-4 configuration show that, the spectra at the three investigated positions in the fuel (*r=10, 20 and 30 cm*) are almost completely dominated by the multiplication in the fuel and look about the same for the different sources. The origins of the sources are almost "forgotten" in most positions in the fuel, even though the peak from the 14 MeV neutrons is still visible far away from the centre of the core.

In the case of the spallation source, created by 1000 MeV protons impinging on a cylindrical target of lead, the neutron yield has been investigated as a function of the lead target dimensions. When increasing the radius from 5 to 20 cm the spectrum moves towards lower energies, as expected, since the neutrons are surrounded by more scattering material. When varying the height of the lead target, the spallation neutron moderation reaches saturation at a depth of about 50 cm and the spectrum does not change when further increasing the height.

The source efficiencies for the three sources coupled to the simplified model of the MUSE-4 configuration have been calculated with the following results: $j\,^*_{(d,d)} = 1.25$, $j\,^*_{(d,t)} = 2.15$ and $j\,^*_{spallation} = 1.28$. Hence, considering the source efficiency, a *(d,d)-* source coupled to the investigated configuration would be a good substitute for a spallation source. The reason for the high value for the *(d,t)-*source, is the increased fission rate induced in a large part by fissions from the *(n,2n)-*multiplied neutrons in the lead.

The spallation source has been artificially split into a low-energy part (<20 MeV) and a high-energy part (>20 MeV) and the contributions from each of them have been determined. It has been shown that about 63 % of *j* * come from the source neutrons having an energy below 20 MeV and 37 % from the neutrons above 20 MeV ($j_T^* = j_{<20}^* + j_{>20}^* = 1.12 + 0.66 \approx 1.8$).

In future investigations, calculations will be repeated for a more realistic model of the MUSE-4 experiment. In addition to this, the simulation of the *(d,d)*- and the *(d,t)*-sources will be replaced by the pre-defined MCNP-functions with angular and energy dependence included. The data file ENDF/B-VI.4 used in the calculations with MCNPX will also be replaced by the newly evaluated high-energy data file LA150 and the decomposition of the spallation source will be performed with the source neutrons emitted with a correct angular distribution. However, these changes will not invalidate any of the conclusions drawn in this report.

8.7   EXPLANATORY NOTE: DEFINING THE SOURCE NEUTRONS FOR THE SPALLATION SOURCE

When the 1000 MeV protons hit the core a large number of neutrons are created via spallation and other secondary interactions. Most of them are created in the lead target, but some also in the fuel. In this case all neutrons created in the lead buffer have been considered as source neutrons, while all neutrons created outside the lead buffer have been considered as multiplied neutrons (by fission, *(n,xn)*-reactions and spallation etc.).

Two different simulations have been performed to obtain this, one with the entire core present (Figure 8-1) and one with only the lead buffer present (Figure 8-2). The results are shown in Table 8-7. The values in the rightmost column are the ones used in section 8.5.3 and Table 8-4 to calculate *j* * for the spallation source.

Table 8-7. Neutron weight due to different reactions, in the entire core and in the lead buffer, per source proton

	Entire core	**Lead Buffer Only**	**Rest of core** (Col. 2 – col. 3)
Fission *(F)*	610	0	610
(n,xn)-reactions *(X)* [10]	4.58	1.82	2.76
Nuclear Interactions *(NI)* [11]	30.41	22.0	8.4

As is seen in the table almost 24 neutrons for each source proton are created in the lead buffer. However, some neutrons are "consumed", and to calculate the net number of

---

[10] Neutrons produced by *(n,xn)-reactions*, by neutrons having an energy lower than 20 MeV, weighted per source neutron.

[11] Neutrons produced by *"nuclear interactions"*, weighted per source neutron. The neutrons produced by neutrons with an energy higher than 20 MeV are labelled "Nuclear Interactions" in MCNPX.

source neutrons produced in the lead, absorbed neutrons have to be subtracted off, according to Table 8-8. The value of 21 neutrons at the bottom of the rightmost column is the one used in Table 8-4 to normalise the number of neutrons produced to be per source *neutron,* instead of per source *proton*.

Table 8-8. Neutron balance in the lead buffer

	X (n,xn)	*NI*	Other	Total
Produced	1.82	22.0		23.82
Absorbed	0.89	1.52	0.37	2.78
Neutron gain	**0.93**	**20.48**	**-0.37**	**21.04**

9   SPALLATION TARGET DEVELOPMENT

The International Science and Technology Centre Project # 559 "Pilot flow lead-bismuth target of 1 MWth for accelerator-based systems" is a collaborative project between Institute of Physics and Power Engineering (IPPE) in Obninsk, Los Alamos National Laboratory (LANL), Royal Institute of Technology and CEA-Cadarache. Funding parties of this project are USA, EU and Sweden.

The purpose of the project is to develop a heavy metal-Pb/Bi eutectic- flow target, which possesses the best features for producing neutrons at a high power proton accelerator. Thus, the technical key problems of a flowing Lead-Bismuth 20 MW-power target should be investigated. Such a technical base will be established by the design of a pilot lead-bismuth 1 MW power target. It is decided that the pilot target will be tested at the LANSCE accelerator at LANL (LANSCE: 800 MeV, 1.5 mA linear proton accelerator) after extensive off-beam tests, first in Obninsk year 2000 and then in Los Alamos.

The spallation target (Figure 9-1) has been manufactured and then tested 2 times during the reported period.
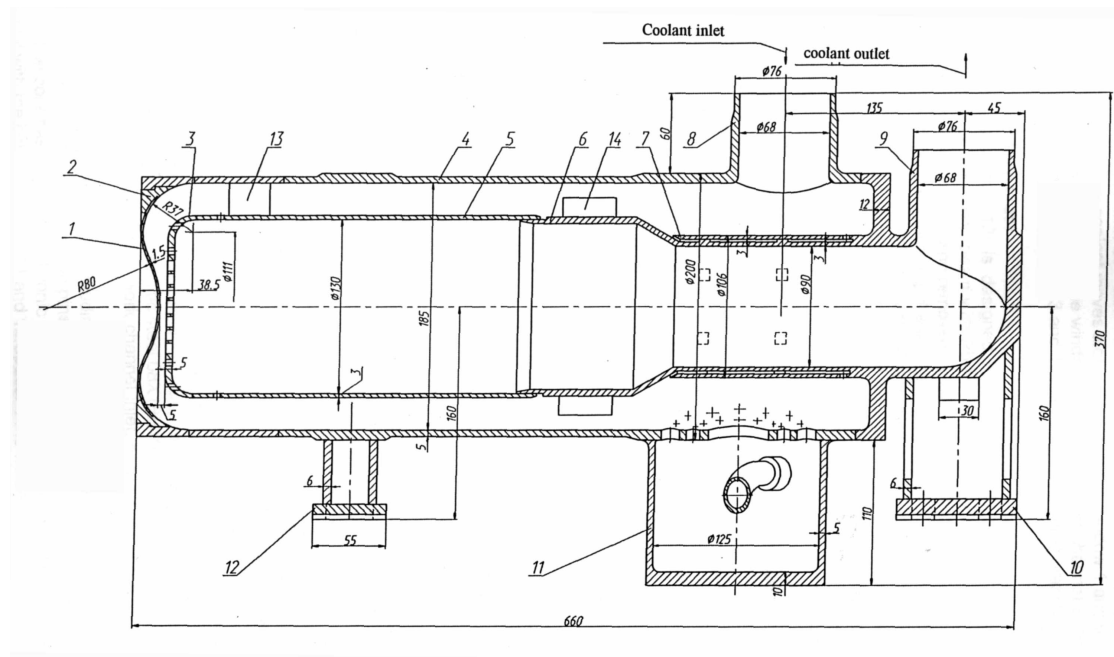

Figure 9-1. The spallation target. Main components of the target: 1 - window, 2 - window support, 3 - diffuser plate (see Fig. 9-3), 4 - target hull (see Fig. 9-2), 5 - inner channel.

The first tests revealed some problems with electromagnetic pumps (EMP). The electromagnetic pump, which was to be mounted into the spallation target circuit (see Figure 9-2) failed during the test runs in May 2000. EMP failed apparently by faulty
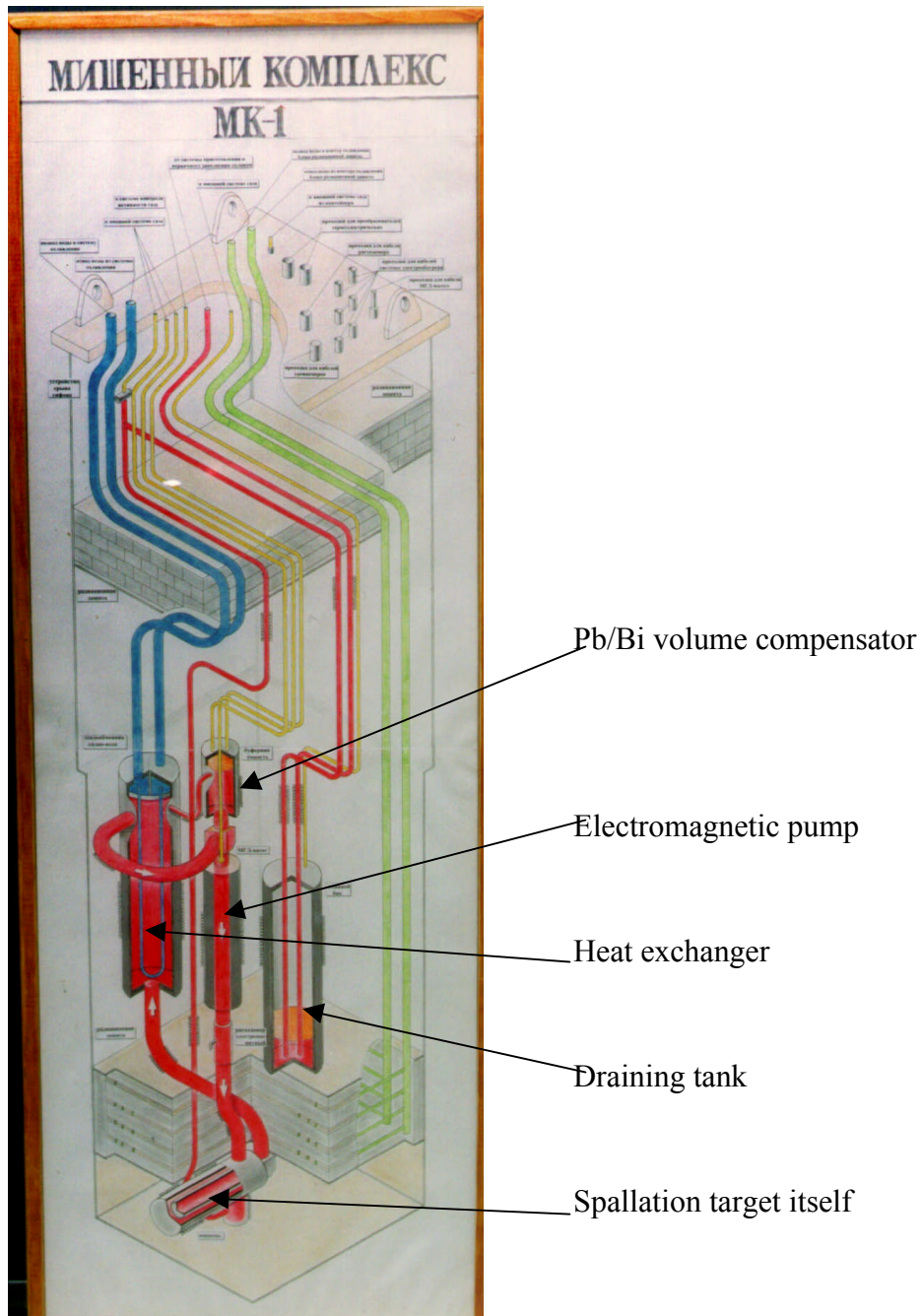
Figure 9-2. Schematic diagram of the spallation target circuit including heat-exchanging and out-gassing piping. Blue color marks low temeprature circuit, red color – high tempertaure.

welds and/or by gas pressure buildup caused by outgassing processes in a ferromagnetic metallic powder core of the EMP. Metallic powder is normally conditioned before installation into pumps but then undergoes anyway spontaneous outgassing processes during an initial phase of operation due to unavoidable exposure to humid air during

installation. A reserve EM pump of the same construction was not able to reach designed operational parameters. Therefore a decision was made to manufacture another EMP with more stringent technological control. This new pump was then mounted into the target circuit.

During the second series of tests in November 2000, the EMP reached required operational parameters with a flow rate of 20 m³/hr and efficiency of 7%. However, other problems emerged during those tests.

The target circuit was successfully filled with liquid Pb-Bi eutectic, which then circulated many times for 2-3 hour runs until the temperature increased above 300 C. For these tests target had no cooling in a heat-exchanger – the heat exchanger was designed for pressurized hot water cooling at LANL; a pressurized hot water cooling system is not available at IPPE. Therefore the EM-pump heats efficiently up the liquid metal.

Most of the control equipment and electronics designed and manufactured at LANL worked properly except for 2 level-meters (see Figure 9-3) - out of 8 - were malfunctioning. It did not effect thermal hydraulic tests but could not be approved as a successful test run.
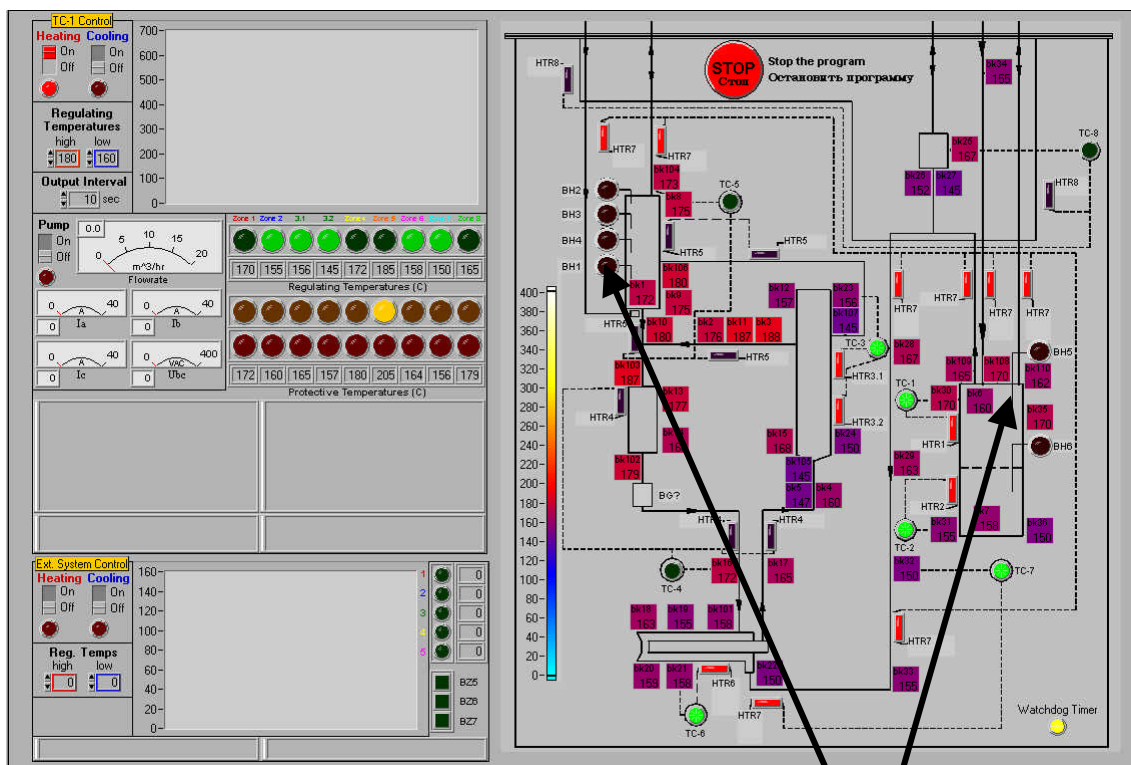

Figure 9-3. A control console of the spallation target circuit. Failing level-meters.

Failing level-meters had an important function to signal filling of the drainage tank (a right arrow on Figure 9-3) and to signal ground level in a compensation tank (a left arrow on Figure 9-3). Figure 9-4 shows more details about failing sensor in the drainage tank.

The decision was made to prolong the spallation target project by 6 months to determine the reasons for the faulty performance of the level-meters and to exchange all the level-meters to more reliable ones.

Final thermal hydraulic tests of the spallation target were scheduled for April 2001.

Level sensors BH5 and BH6 indicating LBE level in drainage tank. **Sensor BH5 failed**.

Temperature indicators in and around drainage tank.

Figure 9-4. Detailed view on failing sensor BH5 in th edrainage tank.

10 SEMINARS, CONFERENCES AND INTERNATIONAL INTERACTIONS

The Fourth Accelerator and Transmutation Technology Workshop", Korea Atomic Energy Research Institute, Taejon, Korea, January 2000. Invited speaker – Waclaw Gudowski.

Visit to KAERI, Korea and JAERI, Japan , Januray 2000. Presentation of EU-Confirm project – Janne Wallenius

Visit to Argonne National Laboratory, preparation of a collaboration project, January 2000 – Marcus Ericsson.

ADS Technical Working Group (ADS-TWG) meetings in Rome, February and October, Cadarache – June, Paris - September 200. Preparation of ADS Roadmapping report – Waclaw Gudowski.

EU-ADS cluster meeting, Paris, March 2000 – Waclaw Gudowski, Janne Wallenius

VTT, Helsingfors, March. Lecture on transmutation – Janne Wallenius

MCNP4C-course in Los Alamos, USA, March 2000 – Janne Wallenius, Per Seltborg

Visit to Argonne National Laboratory, preparation of a collaboration project, March 2000 – Waclaw Gudowski.

OECD/NEA – ADS expert group meeting, Paris, April 2000 – Waclaw Gudowski

EU-harmonisation meetings for a new XADS-project, Paris, Maj and September 200 – Waclaw Gudowski

Technical Working Group on Fuel Development Projects, Karlsruhe, Maj 2000 – Janne Wallenius

Confirm - project meeting, Cadarche, Juni 2000 – Janne Wallenius

IAEA Coordinated Research Project Meeting "Use of Th-based Fuel Cycle in Accelerator Driven Systems (ADS) to Incinerate Pu and to Reduce Long-term Waste Toxicities", Minsk, August 2000 – Waclaw Gudowski

Linac2000, XX International Linac Conference, Monterey, August, 21-25, 2000. Invited paper - Waclaw Gudowski (see Appendix VIII)

Internatoinal Conference on Emerging Nuclear Energy Systems – ICENES, Peetn, September 2000 – Janne Wallenius, Kamil Tucek (see Appendix IX)

Kick-off meeting of EU-project SPIRE, Saclay September 2000 – Janne Wallenius

EU ADS-network project meeting, Paris September 2000 – Waclaw Gudowski

EU MUSE-project - kick-off meeting, Cadarache, Septmeber 2000 – Waclaw Gudowski, Per Seltborg

IAEA Advisory Group Meeting "Design and Performance of Reactor and Subcritical Blanket Systems with Lead and Lead-Bismuth as Coolant and/or Target Material", Moscow, 23 - 27 October 2000 – Janne Wallenius

International Conference on Advanced Monte Carlo for Radiation Physics, Particle Transport Simulation and Applications, 23-26 October, 2000, Lisbon, Portugal. Invited speaker – Waclaw Gudowski (see Appendix X)

IAEA Technical Committee Meeting on "Core Physics and Engineering Aspects of Emerging Nuclear Energy Systems for Energy Generation and Transmutation", 28 November to 1 December 2000, Argonne National Laboratory – Marcus Ericsson (see Appendix XI)

Tests of 1 MW Spallation Target in Obninsk, November 2000 – Waclaw Gudowski (see Chapter 9)

NEA/OECD – "6th Information Exchange Meeting on Actinide and Fission Product Partitioning and Transmutation" Madrid (Spain), 11-13 December 2000 – Waclaw Gudowski, Janne Wallenius (see Appendix II)

International Workshop on "Role of Accelerators in Nuclear Power Applications" Trombay, Mumbai, India, December 2000 – Waclaw Gudowski

11   REFERENCES

[1]   A. Languille et al, CAPRA core studies, the oxide reference option, in Proc.Int. Conf. Future Nuclear Systems, GLOBAL 95, page 874, ANS 1995.

[2]   C. Rubbia et al., Fast neutron incineration in the Energy Amplifier as alternative to geologic storage: The case of Spain- Technical Report CERN/LHC/97-01(EET),1997.

[3]   T. Umeoka et al, Study of CDA driven by ULOF for the nitride fuel core, in Proc. Int. Conf. Future Nuclear Systems, GLOBAL 99, ANS 1999.

[4]   W. Maschek, D. Thiem and P. Lo Pinto, Core disruptive accident analysis for advanced CAPRA cores, in Proc. 4th Int Conf. Nuclear Engineering, ICONE-4, page 237, ASME 1996.

[5]   H. M. Beamont et al, CAPRA core studies, high burnup core Ð conceptual study, in Proc.Int. Conf. Future Nuclear Systems, GLOBAL 97, page 137, ANS 1997.

[6]   T. Takizuka et al, Studies on accelerator driven transmutation systems, In Proc. 5th int. information exchange meeting on actinide and fission product partitioning and transmutation, EUR 18898 EN, OECD/NEA 1998.

[7]   J. Wallenius, K. Tucek, J. Carlsson, and Waclaw Gudowski, "Application of Burnable Absorbers in an Accelerator-Driven System," Nucl. Sci. Eng. 137, p. 96-106, (2001).

[8]   Karl O. Ott and Robert J. Neuhold, "Introductory Reactor Dynamics," American Nuclear Society, 1985.

[9]   H. H. Hummel and D. Okrent, "Reactivity Coefficients in Large Fast Power Reactors," p. 190, publ. by American Nuclear Society, 1978.

[10] W. M. Rohsenow, H. Choi, "Heat, Mass, and Momentum Transfer," p. 193, Prentice-Hall, 1961.

[11] M. Eriksson, J. Wallenius, K. Tucek, W. Gudowski, J. E. Cahalan, "Preliminary Safety Analysis of the Swedish ADS Employing Nitride Fuel and Burnable Absorbers", IAEA Technical Committee Meeting on Core Physics and Engineering Aspects of Emerging Nuclear Energy Systems for Energy Generation and Transmutation, Argonne, 28 Nov-1 Dec, 2000.

[12] M. Eriksson, "Reliability Assessment of the LANSCE Accelerator System," M.Sc. thesis, Royal Institute of Technology, Stockholm (1998).

[13] J. E. Cahalan, A. M. Tentner, and E. E. Morris, "Advanced LMR Safety Anlaysis Capabilities in the SASSYS-1 and SAS4A Computer Codes," Proc. Of the International Topical Meeting on Advanced Reactors Safety, Pittsburgh, April 17-21, 1994.

[14] H. S. Khalil, T. A. Taiwo, F. E. Dunn, R. B. Turski, E. E. Morris, and J. E. Cahalan, "Coupled Reactor Physics and Thermal-Hydraulics Computations with the SAS-DIF3DK Code," Proc. Joint International Conference on Mathematical

Methods and Supercomputing for Nuclear Applications, Saratoga Springs, New York, October 5-9, Vol. 2, pp. 1063-1071, American Nuclear Society (1997).

[15] T. A. Taiwo, "DIF3D-K: A Nodal Kinetics Code for Solving the Time-dependent Diffusion Equation in Hexagonal-Z Geometry," Argonne National Laboraory, ANL/NPR-92/17, October (1992).

[16] C. B. Carrico, E. E. Lewis, and G. Palmiotti, "Three-Dimensional Variational Nodal Transport Methods for Cartesian, Triangular, and Hexagonal Criticality Calculations," Nuclear Science and Engineering, 111, pp. 168-179, June (1992).

[17] G. Palmiotti, C. B. Carrico, and E. E. Lewis, "Variational Nodal Methods with Anisotropic Scattering," Nuclear Science and Engineering, 115, pp. 223-243, November (1993).

[18] E. E. Lewis, C. B. Carrico, and G. Palmiotti, "Variational Nodal Formulation for the Spherical Harmonics Equations," Nuclear Science and Engineering, 122, pp. 194-203, (1996).

[19] E. E. Lewis and G. Palmiotti, "Simplified Spherical Harmonics in the Variational Nodal Method," Nuclear Science and Engineering, 126, pp. 48-58, (1997).

[20] F. E. Dunn and J. E. Cahalan, "Computationally Efficient Thermal Hydraulics Calculations in the SAS-DIF3DK Coupled Reactor Physics and Thermal Hydraulics Code," Proc. Joint International Conference on Mathematical Methods and Supercomputing for Nuclear Applications, Saratoga Springs, New York, October 5-9, Vol. 2, pp. 1097-1106, American Nuclear Society (1997).

[21] Hundsbedt, A., Magee, P.M., 1988, Design and performance of the PRISM natural convection decay heat removal system, Proc. Int. Topical Meeting on Safety of Next Generation Power Reactors, pp. 844-851

[22] Cinotti, L., and Corsini, G., 1999, A proposal for enhancing the primary coolant circulation in an ADS, unpublished

[23] Reeks, M., 2001, The ICRP Model of the Human Repository Tract: a brief summary relating to lung deposition, not published yet

[24] Rousanov, A.E. et al., 1998, Design and study of cladding steels for fuel elements of NPP using heavy coolant, Proc. Heavy Liquid Metal Coolants in Nuclear Technology, HLMC 98. IPPE

[25] Talbot, L. Cheng, R.K., Schefer, R.W., Willis, D.R., 1980, Thermophoresis of particles in a heated boundary layer, J. Fluid Mechanics, vol. 101, part 4, pp.737-758

[26] J. F. Briesmeister, Editor: „MCNP –A General Monte Carlo Code N-Particle Transport Code", LANL report LA-12625-M, Version 4B (March 1997)

[27] J. Cetnar: "A Method of Transmutation Trajectories Analysis in Accelerator Driven System" Proc. IAEA Technical Committee Meeting on Feasibility and Motivation for Hybrid Concepts for Nuclear Energy Generation and Transmutation, Madrid, 17-19 Sept. 1997.

[28] Judith F. Briesmeister, Editor, ``MCNP -- A General Monte Carlo N-Particle Transport Code," Los Alamos National Laboratory report LA-13709-M (April, 2000).

[29] http://www.epm.ornl.gov/pvm/pvm_home.html

[30] Richard B. Firestone, Virginia S. Shirley*, Coral M. Baglin, S.Y. Frank Chu, and Jean Zipkin, The 8th edition of the Table of Isotopes, book and CD-ROM, John Wiley & Sons, Inc., 1996.

[31] A. G. Croff: "A User's Manual for the ORIGEN2 Computer Code", ORNL /TM-7157 (Oct. 1980)

[32] R.E. Prael, H. Lichtenstein. "User Guide to LCS: The LAHET Code System". Report LA-UR- 89-3014, Los-Alamos National Laboratory, New-Mexico, USA

[33] Laurie S. Waters, Editor, MCNPX Users's Manual, TPO-E83-G-UG-X-00001, LANL, 1999.

[34] EURATOM 1996. Laying Down Basic Safety Standards for the Protection of the Health of Workers and the General Public from the Dangers Arising from Ionizing Radiation. Council Directive 96/29 Euratom of May 13, 1996. Official Journal of the European Communities, Vol. 39, No. L 159, June 29, 1996.

[35] Byung-Chan Na, editor, Comparison Calculations for fn Accelerator-Driven Minor Actinide Burner, NEA/OECD Nuclear Science Committee, NEA 2001 (prepared fo publication)

[36] W. Gudowski and I. Slessarev, editors, "IAEA Benchmark on Accelerator-Driven Systems - Use of Th-based Fuel Cycle in Accelerator Driven Systems (ADS) to Incinerate Pu and to Reduce Long-term Waste Toxicities", International Atomic Energy Agency, IAEA 2001, (prepared for publication)

[37] R.E. MacFarlane, The NJOY Nuclear Data Processing System, Version 91, Report LA-12740-M, Los Alamos National Laboratory, 1994

[38] http://t2.lanl.gov/codes/njoy99/

[39] M. B. Chadwick, P. G. Young, S. Chiba, S. C. Frankle, G. M. Hale, H. G. Hughes, A. J. Koning, R. C. Little, R. E. MacFarlane, R. E. Prael, and L. S. Waters, "Cross Section Evaluations to 150 MeV for Accelerator-Driven Systems and Implementation in MCNPX," Nuclear Science and Engineering 131, No. 3 (March 1999) 293.

[40] A. V. Ignatyuk, W. Gudowski et al., Neutron and Proton Cross Section Evaluations for ^{232}Th up t6o 150 MeV, submitted to Nuclear Science and Engineering.

[41] V.S. Barashenkov, Cross Sections of Particle and Nucleus Interactions with Nuclei (Russian), JINR, Dubna, 1993.

[42] M. Salvatores, M. Martini, I. Slessarev, "MUSE-1: A first experiment at MASURCA to validate the physics of sub-critical multiplying systems relevant to ADS", Kalmar, Sweden, June 3-7, 1996

[43] R. Soule, M. Salvatores, R. Jacqmin, "Validation of neutronic methods applied to the analysis of fast sub-critical systems: The MUSE-2 experiments", Global'97, page 639, 1997

[44] J.F. Lebrat et al, "Experimental investigation of multiplying sub-critical media in presence of an external source operating in pulsed or continuous mode: The MUSE-3 experiment", CEA/Cadarache.

[45] W. Assal, C.A. Bompas and R. Soule, "Geometrical and physical data for the MUSE 4 experiment", CEA/Cadarache (1999).

[46] J.M. De Conto, "GENEPI: A high intensity deuteron accelerator for pulsed neutron production", Institut des Sciences Nucléaires de Grenoble.

[47] J.Y. Doriath et al, "ERANOS 1: The Advanced European System of Codes for Reactor Physics Calculation", International Conference on Mathematical Methods and Super Computing in Nuclear Application, 19-23 April 1993, Kongresszentrum, Karlsruhe Germany.

[48] G. Palmiotti et al, "BISTRO Optimized Two Dimensional Sn Transport Code", Topical Meeting on Advances in Reactor Physics, Mathematics and Computation, April 1987, PARIS, FRANCE